

Set-up of the motion control and
characterization of the ablation laser for the
condensed ^{83m}Kr conversion electron source
of the KATRIN experiment

Diplomarbeit

Richard Bottesch

Institut für Kernphysik

Mathematisch-Naturwissenschaftliche Fakultät
der
Westfälischen Wilhelms-Universität
Münster

Juli 2012

Ich versichere, dass ich die Arbeit selbständig verfasst und keine anderen als die angegebenen Quellen und Hilfsmittel benutzt, sowie Zitate kenntlich gemacht habe.

Ort, Datum

Unterschrift

Referent: Prof. Dr. Ch. Weinheimer

Koreferent: Prof. Dr. A. Khoukaz

Contents

1. Introduction	1
1.1. The beginning of neutrino physics	1
1.2. The experimental search for the neutrino	2
1.3. Neutrinos in the standard model of particle physics	3
1.4. Neutrino sources	4
1.4.1. Natural neutrino sources	4
1.4.2. Artificial neutrino sources	5
1.5. Massive neutrinos	5
1.5.1. The solar neutrino problem	5
1.5.2. Neutrino oscillations	6
1.5.3. Experiments on neutrino oscillations	7
1.6. Determination of the absolute neutrino mass	9
2. The KATRIN experiment	13
2.1. The tritium beta-decay	13
2.2. The MAC-E filter	16
2.3. The setup of the KATRIN experiment	19
2.3.1. The tritium source	20
2.3.2. The transport and pumping sections	21
2.3.3. The pre- and main spectrometers	21
2.3.4. The detector	24
3. The condensed krypton source	25
3.1. Conversion electrons from ^{83m}Kr	27
3.2. Setup and function of the condensed krypton source	27
3.2.1. The gas system	28
3.2.2. The cryogenic section	30
3.2.3. The highly ordered pyrolytic graphite substrate	31
4. Ellipsometry	33
4.1. Polarization of light	34
4.1.1. P-polarized light	36
4.1.2. S-polarized light	37
4.2. Measuring film thickness with reflection ellipsometry	38
4.2.1. Null ellipsometry	40
4.3. The PC ellipsometry	42
4.3.1. The preliminary PC ellipsometry setup	43
4.3.2. Analysis of PC ellipsometry data	44

5. Integrating the CKrS into the CPS	47
5.1. The substrate region	47
5.2. Concept of the CKrS at the CPS	49
5.3. Moving the CKrS inside the CPS	50
5.4. Motion control	51
5.4.1. The test setup	52
5.4.2. The LabVIEW VI	58
6. Characterization of the laser ablation	61
6.1. The setup for ablation	61
6.1.1. The ablation laser	62
6.1.2. The second harmonic generator	65
6.1.3. The Glan-Laser polarizer	66
6.1.4. The dichroic guiding mirrors	67
6.2. Measurements and analyses	69
6.2.1. Adjustment of the laser output power	69
6.2.2. The beam profile	71
6.2.3. Adjusting the laser power using the GLP	74
6.3. Scanning the substrate	77
6.3.1. Changes to the HOPG surface after high-intensity ablation	78
6.4. Quadrupole mass spectrometry	82
6.4.1. The principle of quadrupole mass spectrometry	82
6.4.2. Mass spectra taken during the ablation process	86
6.4.3. The adsorption of gasses at the HOPG surface	91
7. Summary and outlook	93
A. Technical details on the motion control	95
A.1. Details on the IMD 20 drive module	95
A.2. CANopen	97
B. Tables	101
B.1. Measurement data on laser parameters	101
B.2. Measurement data on the beam profile	103
B.3. Power adjustment via the GLP	105
B.4. Measurement data on HOPG damage	106

1. Introduction

Although the neutrino seems to be by far the lightest particle in the universe it is believed to be vital to the past and future development of our universe. Until today the neutrino mass could only be determined to an upper limit of $2 \text{ eV}/c^2$. The goal of the **K**Arlsruhe **T**Ritium **N**eutrino (KATRIN) experiment is the determination of the neutrino mass from the tritium beta-decay with a sensitivity of $0.2 \text{ eV}/c^2$ (90% C.L.). To achieve this level of sensitivity it is necessary to monitor the stability of the retarding potential at the main spectrometer of the KATRIN experiment closely. The **C**ondensed **K**rypton **S**ource (CKrS) is one of the means for this type of monitoring. In order to work properly, absolute cleanliness of the **H**ighly **O**rdered **P**yrolytic **G**raphite (HOPG) substrate, a key component of the CKrS, is imperative.

This diploma thesis addresses the issues of the CKrS being prepared for installation at the KATRIN experiment, which includes development of the motorization and motion control and employing laser ablation as a method for cleaning the HOPG substrate.

1.1. The beginning of neutrino physics

The discovery of radioactivity by A.-H. Becquerel in 1896 gave rise to a number of experiments that aimed at determining the structure of atoms and atomic nuclei. Three types of radiation were discovered and labeled as α , β and γ radiation. α radiation — consisting of helium nuclei [Rut08] — and β radiation — being electrons [Kau02] — are emitted from unstable nuclei. These emissions usually leave the nucleus in an excited state. The transition to a less excited state or the ground state is accomplished through the emission of γ radiation, which is high-energy electromagnetic radiation of a few MeV [Rut14]. The spectra of α and γ radiation proved to be discrete. In a two-body decay, where the nucleus would retain only a small amount of recoil energy the electron should carry the same amount of energy in every β -decay of a given isotope. However, in 1914 J. Chadwick and H. Geiger discovered the β -spectrum to be continuous [Cha14]. It seemed that the laws of conservation of energy, angular momentum and quantum mechanical spin statistics were violated.

In an attempt to correct the apparent mistake, W. Pauli [Pau30] postulated a third particle in the β -decay he called neutron. It was supposed to have a spin of $1/2$, no electrical charge and its mass was assumed to be of the order of the electron mass. Consequently the β -decay could be described as a three-body decay and the continuous spectrum could be explained. In 1932 J. Chadwick discovered an electrically neutral nucleon, which nowadays is known as the neutron [Cha32]. The neutron, which had nearly the same mass as a proton, was evidently too heavy to be the third particle in the β -decay. The theoretical characterization

of the β -decay, which included the “neutrino”¹, was accomplished by E. Fermi [Fer34] in 1934. In this theory the neutrino had no mass and the progeny, neutrino and electron, were generated only during emission. Fermi’s theory successfully described the life time of β -unstable nuclei and the shape of the spectrum. It is still valid today, with only small corrections in the low-energy limit of the weak interaction.

1.2. The experimental search for the neutrino

It was not until 1956, 26 years after W. Pauli postulated the neutrino, that F. Reines and C. L. Cowan succeeded in detecting the neutrino by investigating the inverse β -decay



using a nuclear reactor at the Savannah River power plant as a source for antineutrinos which are produced in the β -decay of the fission products and of free neutrons.

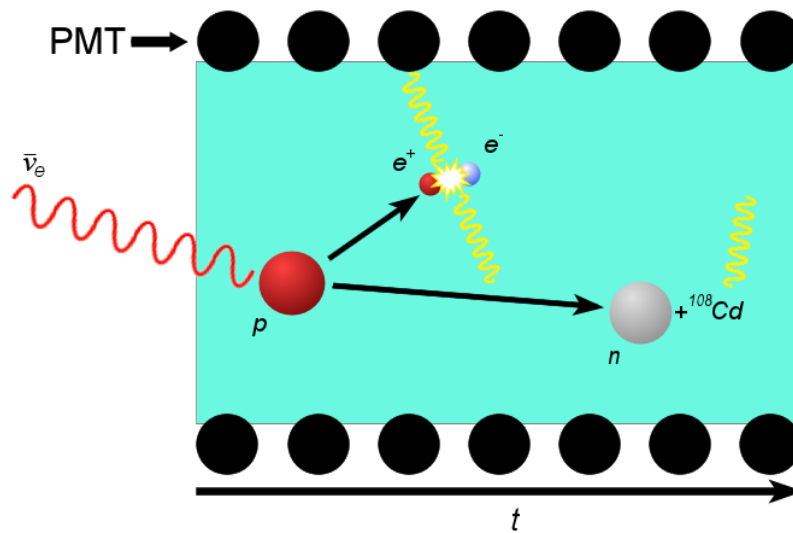
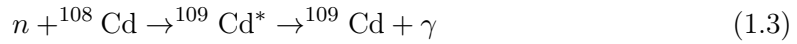


Figure 1.1.: **Schematic of the experiment of Reines and Cowan in 1956.** The light blue area depicts the scintillation detector. The description is found in the text below.

The detector consisted mainly of water with a scintillator material and cadmium chloride [Ron58]. The water provides the target protons for the $\bar{\nu}_e - p$ reaction. The positron from the inverse β -decay quickly finds an electron for an annihilation reaction. Two γ -rays are emitted in opposite directions and have the characteristic 511 keV each. The γ -rays are detected with the scintillation detector and the scintillation light is picked up by photo multiplier tubes (PMT). These signals constitute the first signal in the detection of the antineutrino. The second signal comes from the neutron and its interaction with the

¹Pauli’s neutron was ultimately named neutrino which means small neutron (ital.)

cadmium chloride. When the cadmium absorbs a neutron, it reaches an excited state, followed by the emission of a γ -ray.



The cross section for the $\bar{\nu}_e - p$ reaction was found out to be a mere

$$\bar{\sigma} = (11 \pm 2.6) \cdot 10^{-44} \text{ cm}^2 \tag{1.4}$$

[Rei59]

and is in accordance with Fermi's theory. Today we know that the reason for this small cross section is that the neutrino only interacts weakly with matter. The force carriers of the weak interaction are the Z^0 , W^+ and W^- bosons, which have a mass of $m_{Z^0} = 91.2 \text{ GeV}$ and $m_W = 80.4 \text{ GeV}$ [Nak10]. The uncertainty principle states that the range for interaction is reduced when the mass of exchange particles grows.

1.3. Neutrinos in the standard model of particle physics

In 1962 it became clear that there were more than one kind of neutrinos when the muon neutrino was discovered at the ASG accelerator in Brookhaven. Nowadays the standard model distinguishes twelve fundamental fermions (quarks and leptons) and their respective anti particles. The fundamental particles are categorized into three families (generations) of leptons according to their masses. There are six kinds (flavours) of quarks, which are

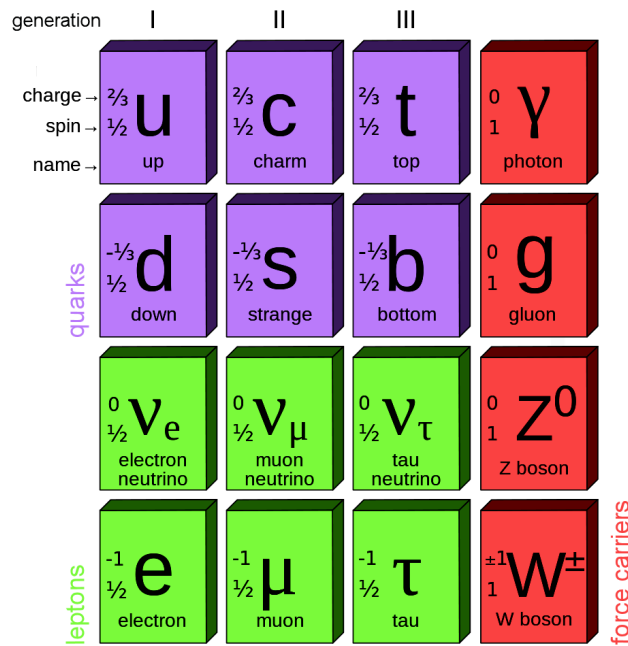


Figure 1.2.: The standard model of particle physics. Figure adapted from [Mis06].

grouped into three colours red, green and blue. The leptons are arranged into doublets (ν_e, e) , (ν_μ, μ) and $(\nu_\tau, \tau)^2$. All neutrinos carry zero electrical charge and all charged

²The τ lepton was discovered in 1975 at the Stanford Linear Accelerator Center (SLAC) by M. L. Perl et al. [Per75]. The existence of the ν_τ was verified by the DONUT experiment in 2000 [Kod01].

leptons carry a charge of $-e$. Quarks carry a charge of $+2/3 \cdot e$ or $-1/3 \cdot e$. (figure 1.2). The antiparticles have the same mass, but opposite electrical charge, colour and I_3 (third component of the weak isospin).

1.4. Neutrino sources

1.4.1. Natural neutrino sources

There are a number of natural neutrino sources. **The sun** for example emits neutrinos during fusion of hydrogen to helium.



This is only one of the possible types of fusion in the sun. Solar neutrinos have energies of $E_\nu \approx 0.3$ MeV.

Supernovae type II³ are another strong neutrinos source. They produce about 10^{57} electron neutrinos with energies of ≈ 10 MeV during the gravitational collaps when huge amounts of electrons are captured

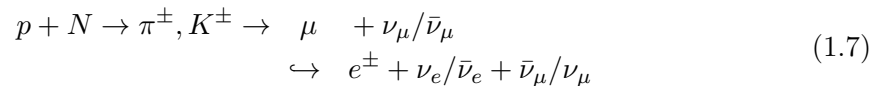


However, 90% of the neutrinos produced in a supernova type II are emitted during the cooling of the resulting neutron star.

Cosmological neutrinos are comparable to the cosmic background radiation. They stem from the thermodynamic equilibrium shortly after the big bang and have cooled down due to the Hubble-Expansion of the universe. There are about $336 \nu/\text{cm}^3$ in the universe⁴ at a temperature of $T_\nu \approx 1.95$ K ($E_\nu \approx 5 \cdot 10^{-4}$ eV)[Rin05].

Highly energetic **cosmic neutrinos** with energies of $E_\nu > 10^6$ GeV occur, when high energy protons from the cosmic radiation interact with target protons or photons in interstellar space. Kaons and pions are generated and decay into neutrinos among other things. Since neutrinos do not interact electromagnetically, their trajectory is a straight line and their point of origin can be determined. High energy protons occur in areas with recent supernovae where they can gain energy from shock fronts. Active galaxy centers are also possible ν sources.

Neutrinos originate not only in space, but also in Earth's atmosphere. **Atmospheric neutrinos** are produced when cosmic radiation interacts with atomic nuclei (O, N) in the upper atmosphere. Cascades of secondary particles with high energies, mainly kaons (K^\pm) and pions (π^\pm), develop. These decay into muons (μ^\pm) which decay further into positrons or electrons (e^\pm).



³Type II supernovae occur with stars with a mass of $M > M_c \approx 8 \cdot M_{sol}$. The solar mass is $M_{sol} = 1.99 \cdot 10^{30}$ kg. Supernovae type I come from stars with $M < M_c$ and do not produce significant numbers of neutrinos.

⁴The background radiation amounts to $411 \gamma/\text{cm}^3$

Most atmospheric neutrinos have energies of $E_\nu \approx 100$ MeV, but can go as high as $E_\nu \approx 10^6$ GeV.

1.4.2. Artificial neutrino sources

Neutrinos can be artificially produced in particle accelerators and of course in nuclear reactors.

Reactor neutrinos ($\bar{\nu}_e$) come from the neutron decay of the fission products (see equation 1.2) and have energies of $E_\nu < 10$ MeV. With every fission about 6 neutrinos are emitted.

Accelerator neutrinos can have energies of up to 300 GeV depending on the method of production. With accelerators it is possible to generate focussed neutrino beams.

1.5. Massive neutrinos

1.5.1. The solar neutrino problem

In the standard model the neutrinos are assumed to be massless. The Homestake experiment which monitored the flow of solar neutrinos however showed, that far less neutrinos from a certain fusion cycle in the sun could be detected than predicted by the standard model.

The Homestake experiment (1970 — 1994) was conducted in an abandoned gold mine in South Dakota by R. Davis et al. A tank with 615 tons of liquid tetrachloroethene (C_2Cl_4) was set up 1400 m deep in the ground. The ν_e interact with the chlorine



The radioactive argon atoms are then extracted from the tank⁵ and with a half-life of 35 days decay back into chlorine. With this method $1/2$ ${}^{37}\text{Ar}$ atoms per day could be produced. The rate with which the neutrinos were detected was

$$\text{Homestake} : 2.56 \pm 0.22 \text{ SNU}^6 \quad [\text{Dav96}], \quad (1.9)$$

whereas the expected neutrino detection rate was

$$\text{SSM} : 9.3 \pm 1.3 \text{ SNU} \quad [\text{Bah95}]. \quad (1.10)$$

This was only about a third of the neutrinos predicted by the standard sun model (SSM). Newer experiments like GALLEX, SAGE, Kamiokande and Super-Kamiokande also observed the same reduced neutrino flow from the sun. This discrepancy was called the solar neutrino problem which could only be explained if neutrino (flavour) oscillations were assumed to be possible.

⁵The extraction efficiency lies at about 95%.

⁶Solar Neutrino Unit, 1 SNU = 1 ν_e -capture per second per 10^{36} target atoms

1.5.2. Neutrino oscillations

In the past few decades several experiments on atmospheric, solar and reactor neutrinos showed that neutrino flavours actually do oscillate. The mechanism for neutrino oscillation is subsequently explained in short:

The flavour eigenstates $|\nu_\alpha\rangle$ ($\alpha = e, \nu, \tau$) are not identical to the eigenstates $|\nu_i\rangle$ ($i = 1, 2, 3$) of the mass operator M . With a unitary mixing matrix U the flavour eigenstates can be described as a superposition of mass eigenstates [Sch97]:

$$|\nu_\alpha\rangle = \sum_i U_{\alpha i} |\nu_i\rangle. \quad (1.11)$$

The reversal is

$$|\nu_i\rangle = \sum_\alpha U_{i\alpha}^+ |\nu_\alpha\rangle = \sum_\alpha U_{i\alpha}^* |\nu_\alpha\rangle. \quad (1.12)$$

The mixing matrix is a 3x3 matrix with three mixing angles and one phase angle which can be CP violating.

The evolution of a mass eigenstate is described by applying Schrödinger's equation ($\hbar = 1, c = 1$).

$$|\nu_i(t)\rangle = e^{-iE_i t} |\nu_i\rangle \quad (1.13)$$

$$\text{with } E_i = \sqrt{p_i^2 + m_i^2} \approx p + \frac{m_i^2}{2p} \approx E + \frac{m_i^2}{2E} \text{ if } p \gg m_i \quad (1.14)$$

This means that different mass eigenstates are propagating with different phase factors, if $m_i \neq m_j$ for $i \neq j$. After the time t an originally (at $t = 0$) pure flavour state will become:

$$|\nu(t)\rangle = \sum_i U_{\alpha i} e^{-iE_i t} |\nu_i\rangle \stackrel{(1.12)}{=} \sum_{i,\beta} U_{\alpha i} U_{\beta i}^* e^{-iE_i t} |\nu_\beta\rangle \quad (1.15)$$

If the neutrino travels a distance d or rather for a time t before being detected through a process of weak interaction, it is possible to produce different leptons l_α and l_β . The transition probability $\mathcal{P}(\alpha \rightarrow \beta; t) \equiv |\langle \nu_\beta | \nu(t) \rangle|^2$ is calculated as follows:

$$\mathcal{P}(\alpha \rightarrow \beta; t) = \left| \sum_i U_{\alpha i} U_{\beta i}^* e^{-iE_i t} \right|^2 \quad (1.16)$$

$$= \sum_i |U_{\alpha i} U_{\beta i}^*|^2 + 2\Re \sum_{j>i} U_{\alpha i} U_{\alpha j}^* U_{\beta i}^* U_{\beta j} e^{-i(E_i - E_j)t} \quad (1.17)$$

Considering an ultra relativistic neutrino, the time t is equivalent to the distance the neutrino travels $d \approx ct = t$, for $c = 1$. In conjunction with equation 1.14 the phase difference in the second part of equation 1.17 becomes:

$$(E_i - E_j)t \approx \frac{m_i^2 - m_j^2}{2} \cdot \frac{d}{E} \equiv \frac{\Delta m_{ij}^2}{2} \cdot \frac{d}{E} \quad (1.18)$$

The average in time t , distance d or energy E of the first part of equation 1.17 represents the average transition probability:

$$\langle \mathcal{P}(\alpha \rightarrow \beta) \rangle = \sum_i |U_{\alpha i} U_{\beta i}^*|^2 = \sum_i |U_{\alpha i}^* U_{\beta i}|^2 = \langle \mathcal{P}(\beta \rightarrow \alpha) \rangle \quad (1.19)$$

Analysis of the average transition probability reveals information about the parameters of the mixing matrix. Equation 1.18 shows that the transition probability changes periodically with d/E . This means that the second part of equation 1.17 describes the process of neutrino oscillation. This however is only possible, if at least one of the neutrino masses $m_i \neq 0$, otherwise all Δm_{ij}^2 disappear.

For a demonstration of this issue, consider two flavour mixing with only two kinds of neutrinos, one mixing angle θ and no complex phase:

$$\begin{pmatrix} \nu_\alpha \\ \nu_\beta \end{pmatrix} = \begin{pmatrix} \cos(\theta) & \sin(\theta) \\ -\sin(\theta) & \cos(\theta) \end{pmatrix} \cdot \begin{pmatrix} \nu_1 \\ \nu_2 \end{pmatrix} \quad (1.20)$$

This results in the following transition probability from one flavour state to another:

$$\mathcal{P}(\alpha \rightarrow \beta; d) = \sin^2 2\theta \left(\frac{\Delta m^2 d}{4E} \right) \quad (1.21)$$

Obviously, the mixing angle θ and the mass difference Δm^2 cannot be zero for neutrino oscillation to happen. The mixing angle defines the amplitude and the mass difference, energy and distance define the phase of the oscillation.

Neutrino oscillation is strong evidence for nonzero neutrino rest masses, but experiments in this field are only sensitive to mass differences Δm_{ij}^2 as indicated by equation 1.18. It is merely possible to derive the lowest possible mass for one of the involved neutrinos from the mass difference, the answer to the question on absolute masses m_i however remains hidden to such experiments. All the illustrations in this section are only valid in vacuum. Neutrino oscillation in matter may be different, because of the MSW-effect⁷ [Sch97].

The Homestake experiment could only detect the electron anti neutrino and therefore was not able to prove that neutrino oscillation really existed. Several newer experiments were conducted, which were able to verify this hypothesis.

1.5.3. Experiments on neutrino oscillations

In 1998 the Super-Kamiokande (SK) cooperation showed that neutrinos which originate in the Earth's atmosphere showed flavour oscillation. The SK detector was a cylindrical tank filled with 50 kilotons of ultra clean water which was surrounded by 11 200 PMTs and was seated in the Kamioka mine (Japan) approximately 1000 m below the surface. Through an interaction in the tank the neutrinos could produce charged leptons l_α^\pm ($\nu_\alpha + N \rightarrow l_\alpha^- + X$ and $\bar{\nu}_\alpha + N \rightarrow l_\alpha^+ + X$) which themselves produced Cherenkov radiation due to their

⁷The resonant influence of matter on the probability for flavour transition was named MSW-effect after its discoverers S. Mikheyev, A. J. Smirnov and L. Wolfenstein.

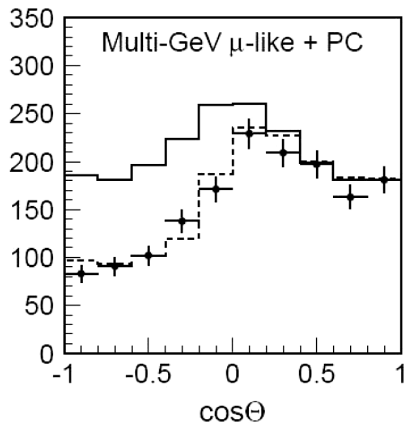


Figure 1.3: **A deficiency in ν_μ depending on the zenith angle** could be observed by the Super-Kamiokande experiment. The continuous line shows the expected neutrino flow without flavour oscillation, the dotted line is a fit to the data which is consistent with two flavour mixing ($\nu_\mu \rightarrow \nu_\tau$) [SK04].

high velocity. This light was then detected with the PMTs. The different ring shaped images of the Cherenkov cone could be used to distinguish between signals from ν_e and ν_μ ⁸. It was observed that there was a correlation between the number of events from ν_μ and the zenith angle. The data shows consistently the case of two flavour oscillation $\nu_\mu \leftrightarrow \nu_\tau$ ⁹. The correlation originates in the different distances d the neutrinos travel depending on the zenith angle ($d_{min} \approx 20$ km and $d_{max} \approx 13\,000$ km).

The data from three phases of data taking (SK I, SK II and SK III) result in best fit value of $\Delta m_{23}^2 = 2.1 \cdot 10^{-3} \text{ eV}^2/c^4$ and $\sin^2(2\theta_{23}) > 0.93$ at 90 % C. L. [Abe11] which is compatible with “maximum mixing” at $\sin^2(2\theta_{23}) = 1$.

In 2001 the SNO collaboration (“Sudbury Neutrino Observation”) showed that the cause for the solar neutrino problem was indeed the neutrino flavour oscillation [Ahm01]. In their experiment they set up a spherical detector of 1000 t D_2O surrounded by 9456 PMTs in a mine near Sudbury, Canada. To shield from cosmic radiation the experiment took place over 2000 meters under ground. The neutrinos can be observed through three types of interaction:

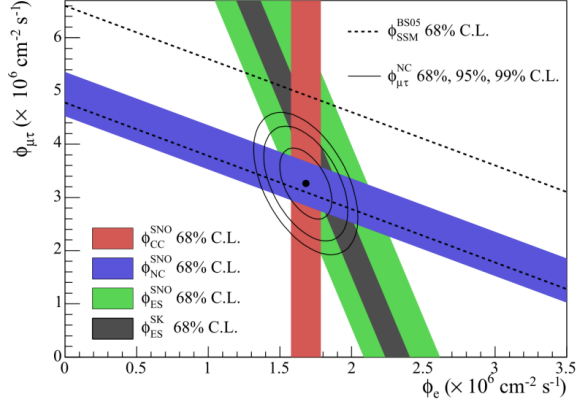
$$\begin{aligned}
 \nu_e + d &\rightarrow p + p + e^- & (\text{CC, charged current}), & \Phi_{CC} &= \Phi_e, \\
 \nu_\alpha + d &\rightarrow p + n + \nu_\alpha & (\text{NC, neutral current}), & \Phi_{NC} &= \Phi_e + \Phi_{\mu\tau}, \\
 \nu_\alpha + e^- &\rightarrow \nu_\alpha + e^- & (\text{ES, elastic scattering}), & \Phi_{ES} &= \Phi_e + 0.16 \Phi_{\mu\tau}.
 \end{aligned}$$

The CC and ES interactions can be identified by their characteristic Cherenkov light. When deuterium captures the neutron from a NC interaction, 6.25 MeV γ radiation is emitted [SNO02]. This way all three kinds of neutrinos ν_α ($\alpha = e, \mu, \tau$) can be detected. With SNO, in addition to the reduced electron neutrino flow Φ_e , a flow of ν_μ and ν_τ from the sun was observed. Since only ν_e are produced in the sun, the other neutrino flavours should develop due to oscillation. The flows Φ_e and $\Phi_{\mu\tau}$ which were measured in the experiment consistently add up to the expected neutrino flow from the SSM, as shown in figure 1.4.

⁸The signals of interacting ν_e would produce blurred rings, whereas ν_μ -rings were sharp.

⁹Oscillation to ν_e is minimal, if not zero.

Figure 1.4: Φ_e versus $\Phi_{\nu\tau}$. The area between the dashed lines represents the total ${}^8\text{B}$ flux predicted by the SSM. The narrow grey band parallel to the SNO ES band represents the Super-Kamiokande result for the ES channel [Fuk02]. The point represents Φ_e from the CC channel and $\Phi_{\nu\mu}$ from the NC-CC difference with the 68%, 95% and 99% C.L. contours included [Aha05].



1.6. Determination of the absolute neutrino mass

Since neutrinos have nonzero rest mass and due to their great number, they make up a significant percentage of the matter in the universe. The magnitude of this percentage depends on the absolute mass of the neutrino, and there are several experiments attempting to determine it.

A number of experiments try to find the mass of cosmic neutrinos. A combination of the data of SDSS-III, WMAP7 [Lar10] and HST¹⁰ [Rie11] measurements result in $\sum_{\nu} m_{\nu} < 0.26 \text{ eV}/c^2$ as the sum of all three neutrino masses [Put12].

Experiments with the neutrinoless double beta decay present another angle to the matter of the neutrino mass. In the $0\nu\beta\beta$ -decay two β -decays take place simultaneously in the same nucleus. The neutrino from the first decay has to be absorbed at the vertex of the second decay (exchange of a virtual neutrino). The Heidelberg-Moscow experiment determined an upper limit of the effective Majorana neutrino mass $m_{ee} < 0.35 \text{ eV}/c^2$ by measuring the half-life for the $0\nu\beta\beta$ -decay of ${}^{76}\text{Ge}$ ¹¹ [Kla01]. The term Majorana implies one of the conditions for $0\nu\beta\beta$ -decay; the neutrino has to be its own antiparticle (Majorana particle). The second condition is the necessity for a change in helicity of the neutrino from the first decay, before being absorbed at the vertex of the second decay. m_{ee} is the coherent sum of the neutrino mass eigenstates $|\nu_i\rangle$ with eigenvalues m_{ν_i} ($i = 1, 2, 3$):

$$m_{ee} = \left| \sum_i U_{ei}^2 \cdot m_{\nu_i} \right| \quad (1.22)$$

The matrix elements U_{ei} specify the electron flavor content of the mass states.

¹⁰SSDS-III: Sloan Digital Sky Survey III, WMAP7: Wilkinson Microwave Anisotropy Probe with seven years of data, HST: Hubble Space Telescope

¹¹Since no actual $0\nu\beta\beta$ -events could be determined, only a lower limit on the half life of ${}^{76}\text{Ge}$ could be calculated. However in a later publication part of the group claimed to have found evidence for the $0\nu\beta\beta$ -decay [Kla04]. This claim is treated very controversially.

A direct way to determine the neutrino mass is the study of the endpoint of the tritium β -decay spectrum. A detailed description of such an experiment will be given in chapter 2. Two experiments of this type have already been conducted and their results are:

$$\begin{array}{lll} \text{Mainz:} & m_{\nu_e} \leq 2.3 \text{ eV}/c^2 & [\text{Kra05}] \\ \text{Troitsk:} & m_{\nu_e} \leq 2.2 \text{ eV}/c^2 & [\text{Lob11}] \end{array}$$

The KATRIN experiment will increase the sensitivity for the measurement of the neutrino rest mass by about an order of magnitude. A neutrino mass of $0.3 \text{ eV}/c^2$ ($0.35 \text{ eV}/c^2$) could be determined with a significance of 3σ (5σ). At least a new upper limit of $0.2 \text{ eV}/c^2$ at 90% C.L. could be gained [Ott08].

Thesis outline

- **Chapter 1** contains a short historical summary of the theoretical and experimental efforts to find the neutrino and measure its mass. Current results from some of the approaches to the neutrino mass problem are given.
- In **chapter 2** the KATRIN experiment is introduced. The experiment aims to determine the mass of the $\bar{\nu}_e$ by analyzing the electrons from the tritium- β -decay with energies close to the endpoint of T_2 - β -spectrum. The key components of the experiment and their functions along with some important parameters for operation are covered here.
- The subject of **chapter 3** is the condensed ^{83m}Kr source (CKrS), the motivation for its use and its setup.
- **Chapter 4** illustrates the role and realization of ellipsometry as a method for determining the cleanliness of the highly ordered pyrolytic graphite (HOPG) substrate. The thickness of very thin films and refractive indices of these films and the substrate are also determined through ellipsometry measurements. An alternative type of ellipsometry is introduced where some of the ellipsometry components have been moved into the cryogenic section inside the ultrahigh vacuum chamber of the CKrS.
- **Chapter 5** contains details on intended setup of the CKrS with regard to its installation at the cryogenic pumping section (CPS) of the KATRIN experiment. The mobility of the CKrS will be ensured by a motion control for which a test assembly and necessary software have been developed.
- **Chapter 6** addresses the issue of laser ablation as a method for cleaning the HOPG substrate. Several tests have been conducted to determine the functionality of the ablation laser setup. An analysis of the gas composition during several phases of the CKrS operation has been performed.
- **Chapter 7** summarizes the results of this thesis and gives an outlook on future tasks at the CKrS regarding the issues presented in this thesis.

2. The KATRIN experiment

The **K**ARlsruhe **T**RItium **N**eutrino (KATRIN) experiment will determine the mass of the electron antineutrino with a sensitivity of 0.2 eV (90% C.L.) by measuring the tritium beta-spectrum near its endpoint of 18.6 keV. A **M**agnetic **A**diabatic **C**ollimation with **E**lectrostatic (MAC-E) filter serves as a spectrometer for isolating the electrons with energies close to the spectral endpoint from the lower energetic background. The setup of the KATRIN experiment and the technical challenges will be explained in this chapter.

2.1. The tritium beta-decay

In the KATRIN experiment the electrons will be produced in β -decay of gaseous tritium (${}^3\text{H}$)¹. Tritium decays into its mirror nucleus helium-3 (${}^3\text{He}^+$).

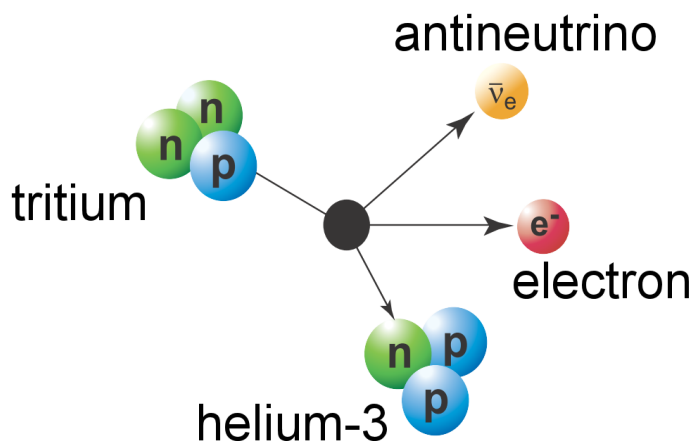


Figure 2.1.: **The β -decay of a neutron in a tritium nucleus.** A neutron converts to a proton by emitting an electron and an electron antineutrino.

In the T_2 - β -decay a neutron in the tritium nucleus converts to a proton by emission of an electron and an electron antineutrino. The atomic number of the nucleus is therefore

¹Tritium, which is often abbreviated by T, is an isotope of hydrogen which possesses two neutrons. Tritium is found in its molecular form, its molecular formula is T_2 .

raised by one whereas the mass number remains the same:

$$(Z,A) \longrightarrow (Z+1,A) + e^- + \bar{\nu}_e \quad (2.2)$$

The decay energy is shared by the electron, the antineutrino and the daughter nucleus. Due to the great mass difference between the daughter nucleus and the other two particles, the recoil momentum is negligible² [Mas07]. Therefore it can be assumed that the total decay energy is shared by the electron and the antineutrino. The β -decay spectrum of the electron is continuous and from its shape the mass of the electron antineutrino can be derived.

Using Fermi's Golden Rule the energy spectrum is calculated as the rate of emitted electrons dN/dt in the energy interval $[E, E + dE]$:

$$\frac{d\dot{N}}{dE} = \frac{d^2 N}{dt dE} = \frac{2\pi}{\hbar} |\mathcal{M}|^2 \rho(E), \quad (2.3)$$

with $\rho(E)$ being the phase space density for the possible final states of the electron and the antineutrino and \mathcal{M} the nuclear matrix element. For the β -spectrum this yields [Alt03]:

$$\frac{d\dot{N}}{dE} = R(E) \sqrt{(E_0 - E)^2 - m_{\bar{\nu}_e}^2 c^4} \Theta(E_0 - E - m_{\bar{\nu}_e} c^2) \quad (2.4)$$

with

$$R(E) = \frac{G_F^2}{2\pi^3 \hbar^7 c^5} \cos^2(\theta_C) |\mathcal{M}|^2 F(Z+1, E) \cdot p \cdot (E + m_e c^2) \cdot (E_0 - E), \quad (2.5)$$

where:

G_F	Fermi coupling constant
θ_C	Cabibbo angle
$\mathcal{M}(E)$	nuclear matrix element for the transition
$F(Z, E)$	Fermi function, which considers the Coulomb interaction between the emitted electron and the daughter nucleus
p, E	momentum and energy of the electron
E_0	endpoint energy of the β spectrum
$m_e c^2$	rest energy of the electron
$m_{\bar{\nu}_e} c^2$	rest energy of the electron anti neutrino

The step function $\Theta(E_0 - E - m_{\bar{\nu}_e} c^2)$ ensures that neutrinos can only be emitted if the available energy exceeds the neutrino rest energy.

For the T_2 - β -decay both the nuclear matrix element \mathcal{M} and the Fermi function $F(Z+1, E)$ do not depend on the neutrino mass $m_{\bar{\nu}_e}$. The nuclear matrix element is also energy independent and has been calculated to $|\mathcal{M}|^2 = 5.55$ [Rob88].

The Fermi function with $Z = 1$ for tritium computes to

$$F(Z+1, E = E_0) = 1.1875 \quad [\text{Ang04}]. \quad (2.6)$$

²The recoil momentum lowers the endpoint of the spectrum slightly, but does not modify its shape significantly.

The neutrino mass affects the decay spectrum through the neutrino momentum contained in the phase

$$p_\nu = \sqrt{(E_0 - E)^2 - m_{\bar{\nu}_e}^2 c^4} \quad (2.7)$$

Figure 2.2 shows the theoretical β -decay spectrum of tritium. Tritium has a very low spectral endpoint E_0 compared to most other β -emitters. The lower the spectral endpoint the more pronounced is the relative influence of the neutrino rest mass. This makes tritium suitable for neutrino mass experiments.

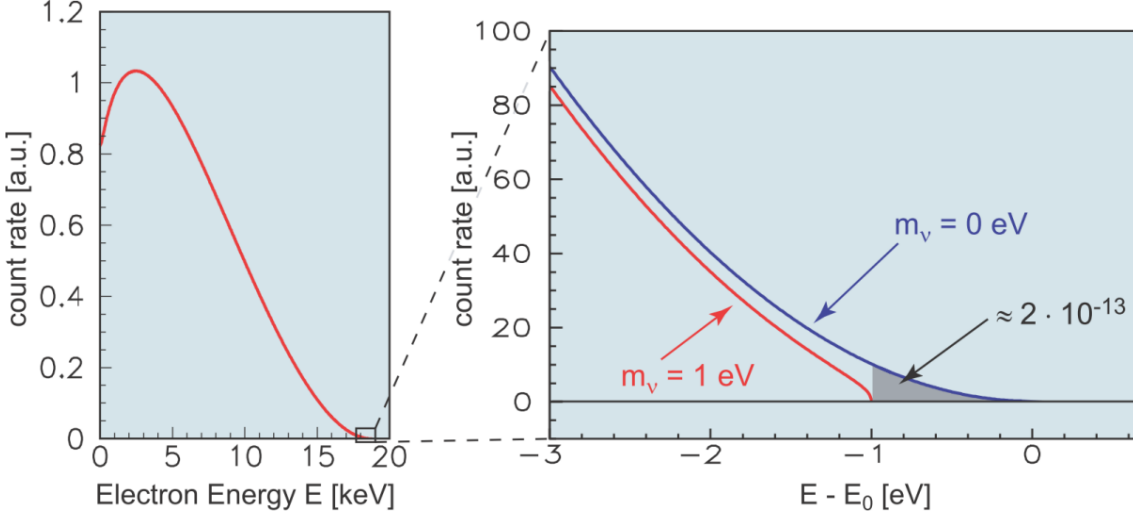


Figure 2.2.: **Signature of a nonzero neutrino mass in the end region of the energy spectrum from the T_2 - β -decay.** The figure shows the complete spectrum for electrons on the left and a magnified end region on the right. The two graphs in the right figure illustrate how the form of the spectrum changes if the neutrino rest mass goes from $m_{\bar{\nu}_e}=0$ eV/ c^2 to $m_{\bar{\nu}_e}=1$ eV/ c^2 . This change concerns the complete spectrum, but is most significant at the end point. In case of an 1 eV/ c^2 neutrino rest mass about $2 \cdot 10^{-13}$ of all decays would fall into the grey-shaded area. Figure [Ang04].

Figure 2.2 indicates that the neutrino mass is detectable as a shift of the endpoint towards a slightly lower energy. However, since measurements of a spectrum contain a significant amount of background, the exact position of the endpoint cannot be identified. The decay energy E_0 of the tritium β decay from gaseous tritium was determined to be

$$E_0(T_2) = 18571.8 \pm 1.2 \text{ eV} \quad [\text{Ott08}]^3. \quad (2.8)$$

The uncertainty in this measurement is still too high to make it a good reference value for the KATRIN experiment in order to gain a neutrino mass with the desired sensitivity. The position of E_0 and the neutrino mass squared $m_{\bar{\nu}_e}^2$ will be free parameters in the fit function of the measured endpoint.

As illustrated in figure 2.2 only a very small fraction of decays produce electrons with the necessary energy to be useful for the experiment. Therefore the accepted angle of

³This result takes the mass difference between T and ^3He from the Penning trap experiment [Nag06] into account.

emission has to be as large as possible. In the same context it is important to achieve a low background rate and with it a good signal-to-noise ratio. Also the energy resolution has to be in the range of the statistical sensitivity for the expected neutrino mass. A sensitivity of $m_{\bar{\nu}_e} = 0.2 \text{ eV}/c^2$ requires a relative resolution of $\Delta E/E = 1:20\,000$. In order to be able to fulfill these strict requirements, MAC-E filters are used in the KATRIN experiment.

2.2. The MAC-E filter

The principle of the MAC-E filter (**M**agnetic **A**diabatic **C**ollimation and **E**lectrostatic filter) was first proposed in [Bea80]. It was used in the neutrino mass experiments in Mainz [Pic92a] and Troitsk [Lob85] and has been developed further for the KATRIN experiment. A significant improvement is the better energy resolution and the newly implemented wire electrode (see section 2.3.3) for background reduction.

$$\begin{aligned} \text{Mainz:} \quad \Delta E/E &= 4.8 \text{ eV} \\ \text{KATRIN:} \quad \Delta E/E &= 0.93 \text{ eV}^4 \end{aligned}$$

KATRIN incorporates two MAC-E filters of different resolution. One is called pre-spectrometer and the other main spectrometer. Solenoids at the entrance and exit of each spectrometer guide the decay electrons magnetically. The magnetic field strength decreases towards the center of the spectrometer where the analyzing plane is located. There the magnetic field strength $B = B_{ana} = 0.3 \text{ mT}$ is minimal.

Figure 2.3 shows the schematic of the main spectrometer. Electrons from the tritium source which enter the spectrometer from one side are guided by the magnetic field towards the detector on the other side. Due to the Lorentz force $\vec{F}_L = q \cdot (\vec{E} + \vec{v} \times \vec{B})$ the electrons follow the magnetic field lines in a cyclotron motion. The kinetic energy of the electrons can be put in terms of parallel and perpendicular to the magnetic field lines E_{\parallel} and E_{\perp} :

$$\begin{aligned} E_{kin} &= E_{\parallel} + E_{\perp} \\ &= E_{kin} \cos^2 \theta + E_{kin} \sin^2 \theta. \end{aligned} \tag{2.9}$$

θ is the angle between the momentum and the magnetic field line and $\cos^2 \theta = \left| \frac{\vec{B} \cdot \vec{v}}{|\vec{B}| \cdot |\vec{v}|} \right|$. Because of the cyclotron motion the electrons retain a magnetic angular momentum

$$\mu = |\vec{\mu}| = \frac{e}{2m_e} |\vec{l}| = \frac{E_{\perp}}{B} = \text{const.} \tag{2.10}$$

which is conserved in motion as long as the changes in the magnetic field are slow during a cyclotron step or in other words adiabatic. Due to the changes in the magnetic field strength the electrons move inside a gradient force field

$$\vec{F}_{\nabla} = \nabla(\vec{\mu} \cdot \vec{B}). \tag{2.11}$$

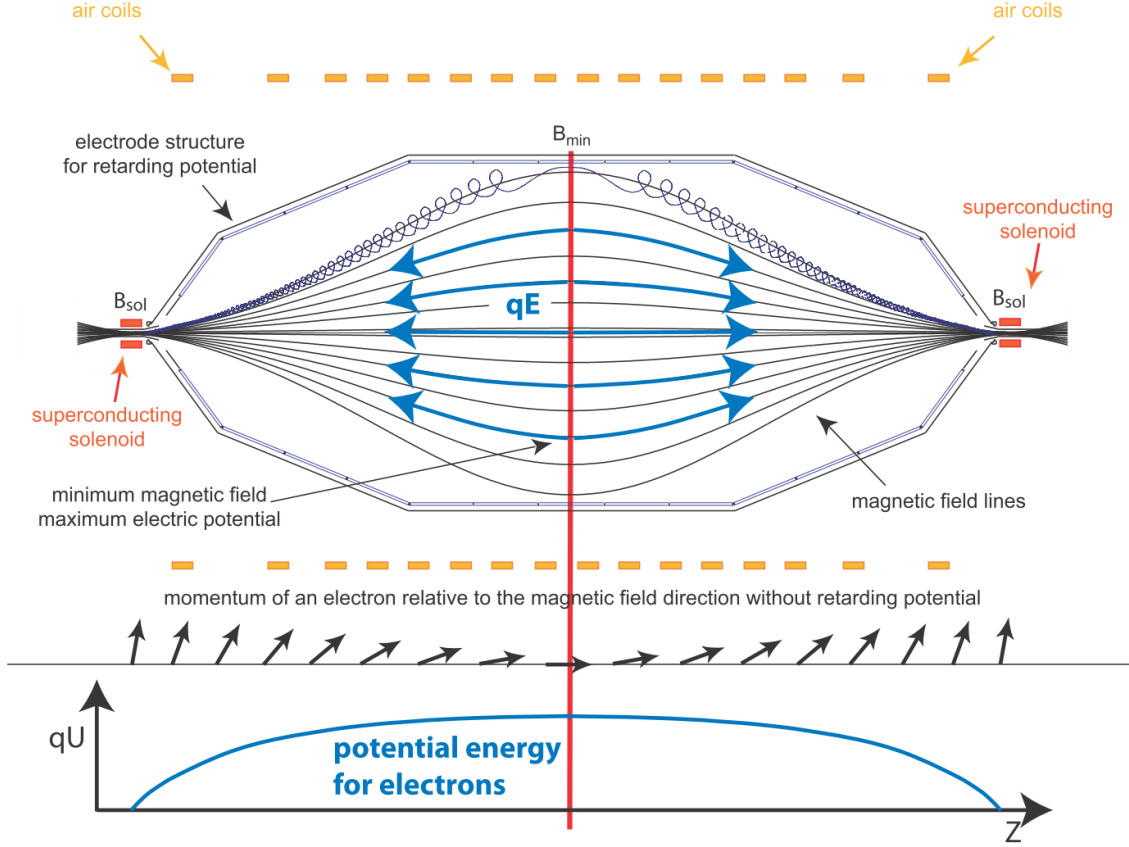


Figure 2.3.: **Cross-section of the main spectrometer.** The spectrometer vessel includes a wire electrode (see section 2.3.3) to repel electrons from muons interacting with the vessel hull. Air coils around the spectrometer compensate for the earth magnetic field. The spiral line represents the trajectory of an electron along an outer magnetic field line and the red line represents the analyzing plane. Figure [Pra11].

As the magnetic field strength drops along the field lines towards the analyzing plane so does E_{\perp} for equation 2.10 to remain true. At the same time the total kinetic energy remains conserved (equation 2.9). This implies an increase in E_{\parallel} along the magnetic field line towards the analyzing plane. On the way to the analyzing plane where the magnetic field strength is lowest, nearly the total kinetic energy is transformed to the E_{\parallel} component. This is where the filtering is done. A negative voltage U_0 is applied inside the MAC-E filter and creates a retarding potential barrier which is highest in the analyzing plane. The barrier repels electrons with insufficient energy and lets electrons pass when

$$E_{\parallel,A} > -e \cdot U_0 \quad (2.12)$$

with $E_{\parallel,A}$ being the energy of the electron motion parallel to the magnetic field line in the analyzing plane. The number of electrons passing the potential barrier can be varied by adjusting U_0 or by applying acceleration or deceleration voltage at the source. This way the β -electron spectrum can be scanned.

⁴This resolution can be achieved if the whole of the flux tube is to remain inside the spectrometer vessel. The resolution can be boosted at the cost of luminosity by reducing the magnetic field strength B_{ana} in the center of the spectrometer.

The so-called pinch magnet, placed in front of the detector, fulfills another filtering function. Since the tritium source is located far outside the entrance solenoid of the main spectrometer, there is a limit to the accepted decay angle⁵ $\theta_{S,max}$ of the β -electrons. This is caused by the different guiding magnets' strength at the tritium source with $B_S = 3.6$ T and the pinch magnet before the detector with $B_p = 6.0$ T. Using equations 2.9 and 2.10 the maximal accepted decay angle is

$$const. = \mu = \frac{\sin^2\theta_S}{B_S} = \frac{\sin^2\theta_p}{B_p} \quad \theta_p=90^\circ \Rightarrow \quad \theta_{S,max} = \arcsin\sqrt{\frac{B_S}{B_p}} = 50.77^\circ. \quad (2.13)$$

Electrons with a decay angle greater than $\theta_{S,max}$ are magnetically reflected, because θ_p becomes greater than 90° [Ang04]. A greater decay angle means a longer traveling distance and therefore a greater chance for the electrons to scatter inelastically at the tritium molecules inside the source. Scattered electrons would have altered energies and must not reach the detector.

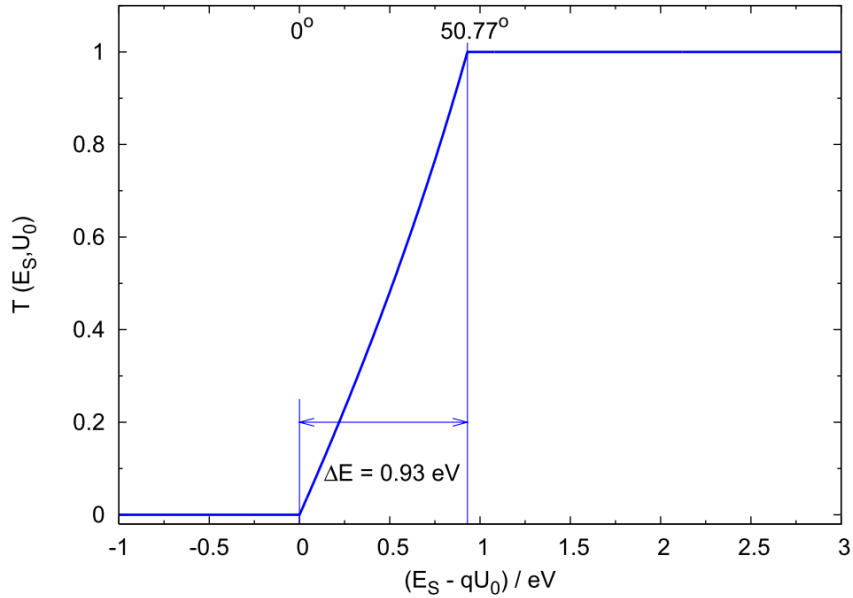


Figure 2.4.: **The analytical transmission function of the KATRIN main spectrometer.** The figure shows the theoretical transmission function of the main spectrometer for electrons with a given energy at the source E_S as a function of the filter energy qU_0 . The three parts of the transmission are distinguishable. In the left part the electron energies are too low to pass the potential barrier. The flank in the middle part is caused by the different angles of emission which requires the electrons to carry different excess energies when passing the barrier. Electrons with small decay angles only need small excess energies while greater decay angles ($\theta_{S,max} = 50,77^\circ$) require higher excess energies to be transmitted. In the right region all electrons are emitted.

If an electron has an E_\perp component close to $E_{kin,max} = 18.57$ keV at the entrance of the main spectrometer, the maximum energy of the electron motion perpendicular to the

⁵The decay angle is the angle between the positive z-axis (see figure 2.3) and the momentum at which the β -electron is emitted.

magnetic field line in the analyzing plane will be

$$\begin{aligned}\Delta E = E_{\perp,max,A} &= E_{kin,max} \cdot \frac{B_{ana}}{B_p} \\ &= 0.93\text{eV}\end{aligned}\quad (2.14)$$

considering the conservation of μ . This value represents the resolution of the main spectrometer. These considerations result in a transmission function which is divided into three parts [Pic02b]:

$$T(E_S, U_0) = \begin{cases} 0 & \text{if } E_S < q U_0 \\ \frac{1 - \sqrt{1 - \frac{(E_S - q U_0) B_S}{E_S B_{ana}}}}{1 - \sqrt{1 - \frac{B_S}{B_{sol}}}} & \text{if } q U_0 \leq E_S \leq q U_0 \frac{B_p}{B_{sol} - B_{ana}} \\ 1 & \text{if } E_S > q U_0 \frac{B_p}{B_p - B_{ana}} \end{cases} \quad (2.15)$$

The transmission function only allows the transmission of electrons with $\theta_S \leq \theta_{S,max}$ and depends on the energy of the β -electrons in the tritium source E_S , the ratio of the magnetic fields in the source and the analyzing plane $\frac{B_S}{B_{ana}}$, the retarding potential U_0 and the spectrometer resolution. The resolution ΔE is the energy interval in which the transmission increases from 0% to 100% (figure 2.4).

2.3. The setup of the KATRIN experiment

The KATRIN experiment is set up at the Karlsruhe Institute of Technology (KIT). Only there at the tritium laboratory (TLK) the necessary amount of tritium with an isotope purity of over 95% can be allocated.

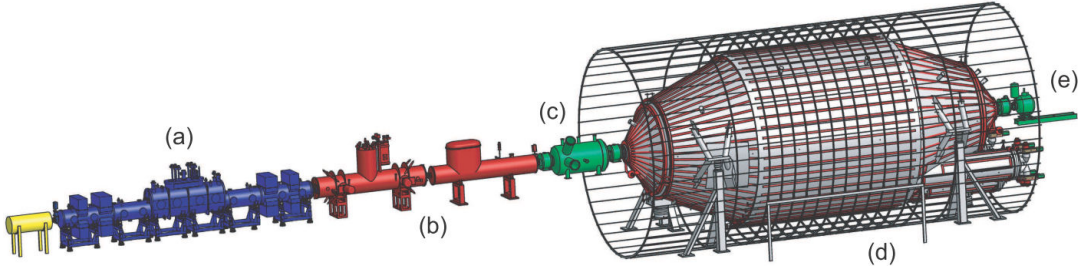


Figure 2.5.: **The KATRIN experiment** consists of five major sections: (a) the windowless gaseous tritium source (WGTS), (b) the transport section with differential and cryogenic pumping section (DPS and CPS), (c) the pre-spectrometer, (d) the main spectrometer with the surrounding air coils and (e) the detector. The total length of KATRIN is about 70 m.

The electrons from the tritium decay in the source (WGTS) are guided magnetically through the transport section consisting of the differential and cryogenic pumping sections towards the spectrometers. The following sections give a more detailed view on the main components of the KATRIN experiment.

2.3.1. The tritium source

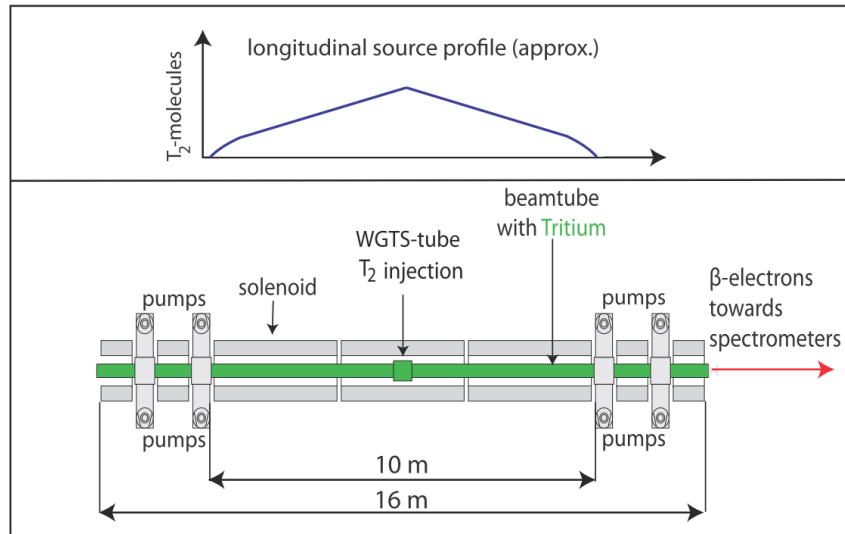


Figure 2.6.: **The windowless gaseous tritium source.** The upper figure shows the density profile of the tritium gas and the lower figure a schematic of the WGTS. Figure [Pra11].

The **Windowless Gaseous Tritium Source** (WGTS) is a tube of 10 m length and a diameter of ≈ 90 mm and contains the tritium which emits the β electrons. The source being gaseous provides very high luminosity, and simulations indicate that the buildup of charge inside the source is only about 10 mV [Ang04]. Gaseous tritium is inserted at 2 mbar \cdot l/s with an inlet pressure of $3.35 \cdot 10^3$ mbar into the center of the WGTS. The gas diffuses towards the ends of the tube where the pressure drops to $4 \cdot 10^{-5}$ mbar.

The tritium inside the source is kept at 30 K with a temperature stability of 30 mK. At a given pressure the column density increases as the temperature decreases. A stable temperature means a stable column density and with it a stable activity of the source. At 30 K the column density is $\rho d = 5 \cdot 10^{17}$ molecules/cm² which translates to an activity of 10^{11} Bq. Another measure to maintain a stable column density is the permanent exchange of the tritium gas. The tritium inlet is 40 g/day. Turbo molecular pumps at both ends of the tube continually remove gas. The density profile inside the WGTS is shown in figure 2.6.

The WGTS is surrounded by super conducting magnets which guide the β -electrons adiabatically at a magnetic field strength of $B_S = 3.6$ T. This results in a magnetic flux tube ($\phi = 82$ mm) of 191 T \cdot cm². An electron gun on the back side of the WGTS (left side in figure 2.6) is used to measure the response function of the complete KATRIN setup and to monitor the source column density.

2.3.2. The transport and pumping sections

Next to the source is the transport section which contains the **Differential Pumping Section**, DPS2-F⁶, and the **Cryogenic Pumping Section**, CPS. Here the electrons are guided adiabatically by solenoids at a field strength of 5.6 T towards the spectrometers. The main task of the transport section is to reduce the amount of tritium, which would otherwise reach the spectrometers. The accepted background from tritium decays inside the spectrometers is 10^{-3} Hz [Ang04] which means in tritium reduction by a factor of 10^{14} compared to the activity inside the WGTS.

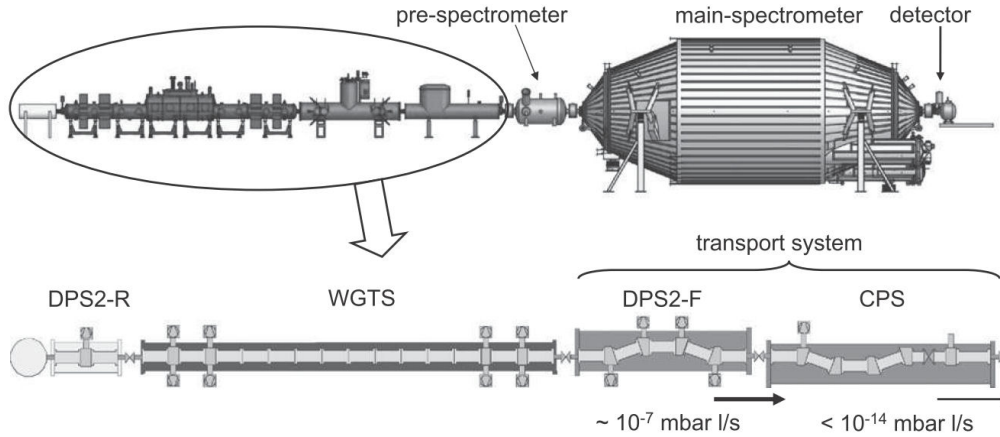


Figure 2.7.: **The differential- and cryo pumping section of KATRIN.** Figure [Pra11].

The DPS2-F has four bends, each housing a turbo molecular pump. The electrons follow the magnetic field lines, whereas the electrically neutral tritium molecules fly on straight trajectories and are removed by the pumps with a very high probability. Yet some T_2 molecules may hit the walls in a fashion that allows them to pass the DPS2-F. The total tritium reduction after the DPS2-F is 10^7 with 10^2 from the DPS1-F and 10^5 from the DPS2-F. The tritium which is removed by the DPS is then fed back into the T_2 -cycle.

The CPS also consists of a four times bent tube, but its walls are kept at 4.2 K. Argon snow inside the CPS increases the effective surface for a greater probability of tritium sorption [Kaz08]. The tritium flow rate is reduced by another factor of 10^7 . The principle of the CPS has been tested successfully in the **TR**itium **A**rgon **F**rost **P**ump (TRAP) test setup [Stu07].

2.3.3. The pre- and main spectrometers

The spectrometer section consists of the pre- and the main spectrometer both of which are of the MAC-E filter type (see section 2.2). The pre-spectrometer filters electrons with $E < E_0 - 300$ eV and reflects them back towards the source section. The electron flow rate

⁶The DPS2-F is the second differential pumping section in the forward direction. The DPS1-F is located inside the WGTS.

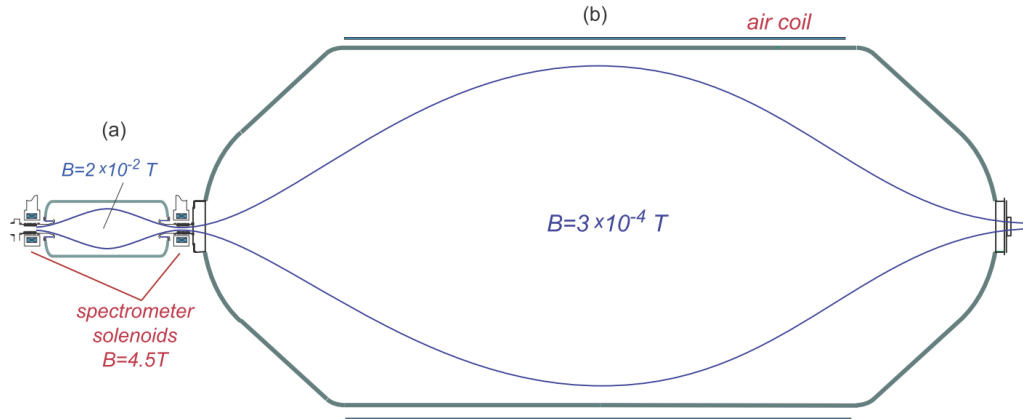


Figure 2.8.: **Pre- and main spectrometer in the KATRIN setup.** Electrons are pre-selected by the pre-spectrometer (a) before they enter the main spectrometer (b). Figure [Thu07].

is thus reduced from 10^{10} down to $1000 \text{ e}^-/\text{s}$. Hereby the chance of electrons scattering at residual gas molecules inside the main spectrometer which might cause background is reduced.

Both spectrometers consist of a cylindrical vessel with conical ends. They mainly differ in size due to their intended resolution. The pre spectrometer has a resolution of 100 eV at 18.6 keV , a length of 3.4 m and a diameter of 1.7 m . The magnetic field in the analyzing plane is $2 \cdot 10^{-2} \text{ T}$. The main spectrometer has a length of 23 m and a diameter of 10 m and achieves a resolution of 0.93 eV as mentioned above. A diameter of this magnitude is necessary in order to maintain the flux tube of $191 \text{ T} \cdot \text{cm}^2$. Otherwise electrons which enter the spectrometer on the outer magnetic field lines would be guided into the walls at the intended magnetic field strength of $3 \cdot 10^{-4} \text{ T}$ in the analyzing plane. The length of the spectrometer is required for the $E_{\perp} \rightarrow E_{\parallel}$ transition to be adiabatic. The main spectrometer is also surrounded with air coils to compensate the Earth's magnetic field. Without the air coils the electrons would receive a drift and parts of the flux tube would be lost at the walls.

Ionisation processes at residual gas molecules inside the spectrometers would lead to an elevated background. For this reason the pressure will be kept at 10^{-11} mbar by use of six turbo molecular pumps and SAES NEG getter pumps⁷.

Since the expected count rate in the KATRIN experiment is $\mathcal{O}(10 \text{ mHz})$, it is important to keep the rate of background signals at a minimum. One of the two major sources of background is the decay of Radon which is primarily found in the material of the getter pumps in the spectrometers. The main spectrometer uses 3 km of getter material strips. The Radon emanating from it would exceed the maximal accepted background by a factor of 30. This background is reduced by installing liquid nitrogen cooled baffles [Fra11]. Secondary electrons induced by cosmic muons or from decays inside the spectrometer vessel hull are the other major background source.

⁷NEG: **Non-Evaporable Getter**. Getter pumps bind gas molecules chemically to the surface. Diffusion transports the molecules into the getter material.

The wire electrode

The main spectrometer has been equipped on the interior with a mainly double layered wire electrode. The wire electrode is kept at a potential of -200 V with respect to the vessel hull to reflect low energy electrons which are produced inside the hull and propagate towards the interior of the spectrometer back towards the vessel hull. The voltage applied to the wires also influences the retarding potential U_0 in the analyzing plane of the main spectrometer. Therefore careful consideration was given to the configuration of the wire electrode.

To make the installation possible in the first place, a system of modules and mountings has been developed. The spectrometer vessel was equipped with rings of rails on which the modules could be moved into and anchored to their final positions. The precision of the mounting of the modules as well as the placement, thickness and tension of the wires in every module is paramount to the correct generation of the retarding potential.

With the exception of the steep conical regions⁸ the main spectrometer was equipped with double layered electrode modules. Figure 2.9 shows a schematic of wire configuration in a double layer module. The voltages applied to the wire electrode can be varied to help produce the intended retarding potential. A double layered electrode was chosen to compensate for the limitations of precision engineering the spectrometer vessel. At a diameter of about 10 m the difference in the distance l_1 can be as much as 5mm to which the U_{eff} of a single layered electrode would be too sensitive. Applying voltages to the spectrometer vessel and the wire electrode results in an effective potential qU_{eff} rather than the sum of the applied voltages. With the electric screening factor S , defined as

$$S_a = 1 + \frac{2\pi l_a}{s \ln \frac{s_a}{\pi d_a}}, \quad (2.16)$$

this computes to

$$qU_{eff,1} = qU_{wire,1} + \frac{qU_{vessel} - qU_{wire,1}}{S_1} \quad (2.17)$$

and

$$qU_{eff,2} = qU_{wire,2} + \frac{qU_{vessel} - qU_{wire,2}}{S_2} + \frac{qU_{vessel} - qU_{wire,1}}{S_1 \cdot S_2}. \quad (2.18)$$

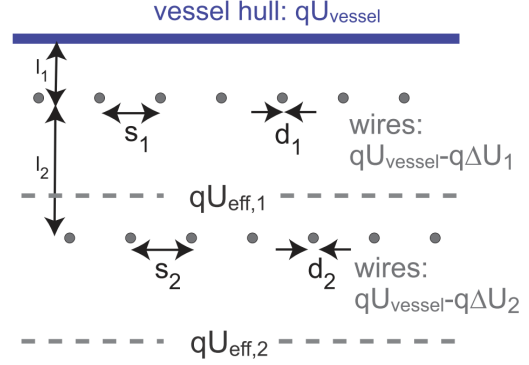


Figure 2.9.: **Double layered wire electrode** with the following parameters: $l_1 = 150$ mm, $l_2 = 70$ mm, $d_1 = 0.3$ mm, $d_2 = 0.2$ mm, $s_1 = s_2 = 25$ mm. Secondary electrons with low energies are reflected electrostatically towards the vessel hull and cannot enter the flux tube. Combining the voltages on the electrode layers and the vessel hull results in an effective potential $qU_{eff,2}$ inside the spectrometer. Figure and values: [Pra11].

⁸The conical regions of the main spectrometer are next to its entrance and exit (see figure 2.3) and have been equipped with single layered electrode modules. The modules were manufactured in different shapes for the steep and flat conical regions and the central part of the main spectrometer.

The retarding potential can be varied to scan the endpoint of the spectrum. Alternatively an acceleration or deceleration voltage can be applied and varied to the source section to the same end.

The third important task of the wire electrode is the removal of electrons from penning traps. For this purpose the electrode is divided into two halves and a different voltage is applied to each half. In this mode of operation, the so-called dipole mode, electrons receive a $\vec{E} \times \vec{B}$ drift when inside the flux tube [Hug08], [Val09].

2.3.4. The detector

Electrons which overcome the potential barrier in the main spectrometer are accelerated and guided towards the detector. The detector is a segmented Si-PIN diode with 148 pixels of equal surface area. Each of the 12 ring segments on the detector contains 12 pixels except for the center which holds only four pixels (figure 2.10). The segmentation allows for the calibration of the transmission function for each pixel and thus identifying inhomogeneities in the retarding potential or the magnetic fields [Ang04]. The transmission function ideally should be the same for every detector pixel.

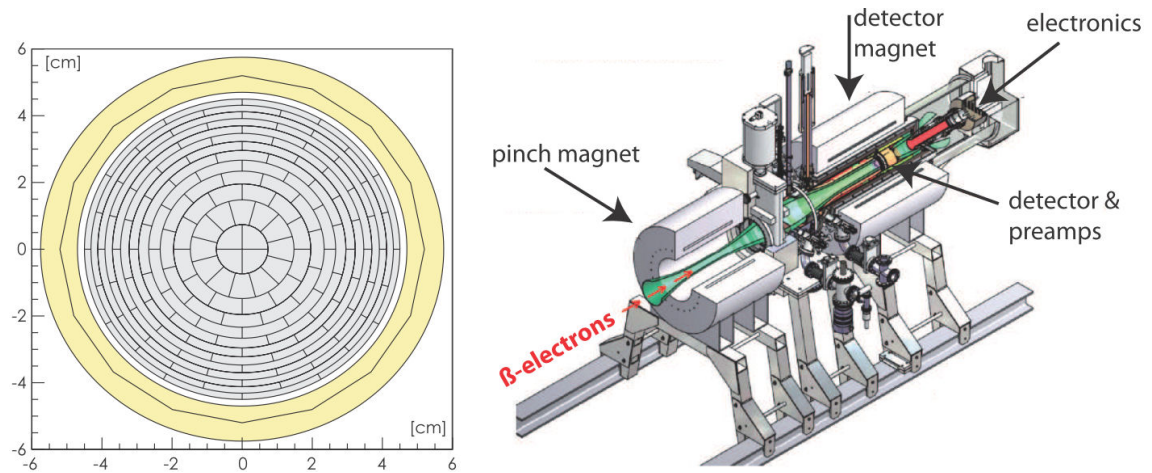


Figure 2.10.: **The detector** segmentation is shown in the left figure. The complete detector setup (right figure [Leb10]) includes the pinch magnet which accounts for the reflection of electrons with decay angles above 50.77° .

To move the T_2 - β -signals into a lower background region, the electrons are post-accelerated by up to 30 keV. The background in the signal region is expected to be less than 1 mHz. A high energy resolution also helps with identifying background and ensures a narrow energy band for signal electrons. Monte Carlo simulations show that a resolution of 1 keV is sufficient [Ang04].

3. The condensed krypton source

In order to achieve the intended sensitivity of $0.2 \text{ eV}/c^2$ on the neutrino rest mass the sum of the uncertainties σ_{tot} in the KATRIN experiment has to be

$$\sigma_{tot} \leq 0.025 \text{ eV}^2. \quad (3.1)$$

This includes the expected statistical uncertainties from measuring the transmission function on the intervall $[E_0 - 30 \text{ eV}, E_0 + 5 \text{ eV}]$,

$$\sigma_{stat} \leq 0.018 \text{ eV}^2$$

and the systematical uncertainties from all components and processes in KATRIN,

$$\sigma_{syst,tot} \leq 0.017 \text{ eV}^2.$$

The monitoring of the retarding potential presents the greatest source for uncertainties with $\sigma_{syst,ret} = 0.0075 \text{ eV}^2$ which is also the upper limit for any single uncertainty in the KATRIN experiment [Ang04]. This results in a tolerable fluctuation of 60 mV at most in the retarding voltage according to

$$\Delta m_\nu^2 = -2\sigma^2 \quad (3.2)$$

for undetected or disregarded gaussian fluctuations [Rob88]. With the retarding potential in the analyzing plane being $U_0 = 18.6 \text{ keV}$ this results in a relative stability of $\frac{0.06\text{V}}{18600\text{V}} = 3 \text{ ppm}^1$ which has to be maintained over the measuring period of 2 month. Therefor KATRIN employs two mechanisms to monitor the stability of the retarding voltage:

1. **Precise high voltage divider** [Thu07].
2. **Calibration sources based on a natural standard** aim for a very accurate, strictly reproducible measurement of the energies of conversion electrons, Auger electrons or photons. A calibration source has to fulfill various criteria to be applicable in KATRIN, such as
 - a narrow line width and good reproducibility of the line position,
 - a high count rate,
 - a short half-life if used in the main beam line and
 - the energies of the emitted electrons (photons) have to be in the area of the T_2 - β -spectrum endpoint.

¹ppm: parts per million

The **C**ondensed **K**rypton **S**ource (CKrS) is one of the calibration sources used in the KATRIN experiment. To fulfill the requirements the CKrS uses the metastable ^{83m}Kr isotope, which produces monoenergetic electrons from disexcitation of the nucleus (section 3.1) with a half-life of $T_{1/2} = 1.83$ h. The ^{83m}Kr which is produced from ^{83}Rb through electron capture is gaseous. A capillary tube allows the gas to pass through to the substrate region inside an ultrahigh vacuum (UHV) chamber where it condenses to the substrate. The substrate is made of **H**ighly **O**rdered **P**yrolytic **G**raphite (HOPG) and sits on top of a 4 K copper cold finger². Due to the long half-life of $T_{1/2} = 86.2$ d the ^{83}Rb cannot be kept inside the main beam line. Long lasting contamination of the spectrometers could otherwise be the result. Section 3.2 will give an overview of the CKrS setup and amongst other things details to how the CKrS manages to separate the ^{83}Rb and ^{83m}Kr .

The K-32 line position for the ^{83m}Kr decay has also proven to be very stable and reproducible as shown in [Ost08]. For meaningful measurements of the transmission function the source has to possess a high count rate (about 2.5 kHz). This can be achieved with a modified substrate region and by heating the inner radiation shield to about 150 K to prevent the Kr gas from condensing onto the radiation shield [Smo08]. However the spectral line stability was not tested with this configuration. Greater outgassing would be the result of heating the inner radiation shield which would possibly lead to more residual gas condensing onto the substrate. This could lead to a shift of the spectral line due to a changed work function.

²During this work the substrate was heated to about 25 - 30 K by a resistive heater to prevent hydrogen from condensing onto the substrate. Molecular hydrogen has a boiling point of 20 K.

3.1. Conversion electrons from ^{83m}Kr

With a probability of 100% ^{83}Rb decays to ^{83}Kr through electron capture. However only a small fraction of the transitions directly end up in a stable Kr isotope.

About 76% of the decays produce the meta-stable ^{83m}Kr isotope. Figure 3.1 shows the relevant decay channel for ^{83}Rb . The energy of the excited state $I = 1/2^-$ is 41.55 keV and has a half-life of $T_{1/2} = 1.83 \text{ h}^3$. By emitting a conversion electron the nucleus reaches the excited state $I = 7/2^+$ which has a half-life of only $T_{1/2} = 0.15 \mu\text{s}$. Emission of another conversion electron eventually results in the stable state $I = 9/2^+$ of ^{83}Kr . The probability with which an electron is emitted compared to emission of a γ -quantum is given by the conversion coefficient α . In the $I = 1/2^- \rightarrow I = 7/2^+$ transition for instance emission of an electron is 2000 times more probable.

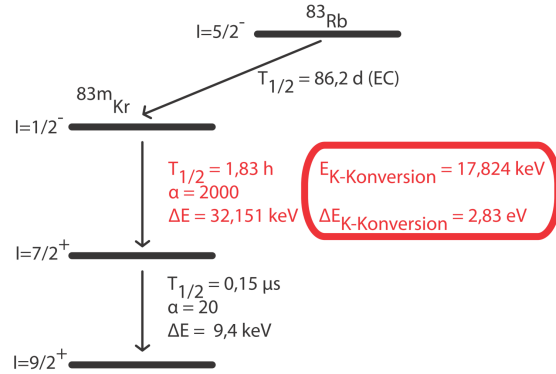


Figure 3.1.: Decay scheme of ^{83}Rb via ^{83m}Kr

During the process of internal conversion, in which the conversion electron is produced, the excited nucleus interacts electromagnetically with and transfers its energy to the electron shell. Every time a single electron is emitted it carries the same kinetic energy⁴

$$E_{kin} = E_{\gamma} - E_b^{vac}. \quad (3.3)$$

E_{kin}	kinetic energy of the conversion electron
E_{γ}	excitation energy of the nucleus
E_b^{vac}	binding energy with respect to vacuum

Conversion electrons from the K-shell have an energy of 17.82 keV and a line width of 2.7 eV [Ost08]. The line width depends on the life-time of the involved excited states.

3.2. Setup and function of the condensed krypton source

The CKrS for the KATRIN experiment has been developed and set up at Institut für Kernphysik of the Westfälische Wilhelms-Universität in Münster. The current setup has been or is being tested on various aspects:

- Automation of the gas system for reproducible gas inlet [Sch11].
- Measuring the thickness of krypton films using laser ellipsometry (details in chapter 4) [Ost08], [Weg10].

³Values taken from [Nudat2].

⁴Please note that equation 3.3 is only valid for free atoms. Condensed atoms are subject to additional effects i.e. the work function of the substrate [Ost08].

- Setting up and testing laser ablation as a means for cleaning the HOPG substrate [Ost08].
- Moving ellipsometry components into the cryogenic region inside the UHV chamber and testing the 'PC ellipsometry' (section 4.3) [Spi11].
- Redesigning the CKrS to be compatible with CPS specifications (a short overview of the concept is given in chapter 5).
- Developing and testing the motion control for the CKrS (section 5.4).
- Automation of the ablation system as a first step for achieving laser class 1 (chapter 6).

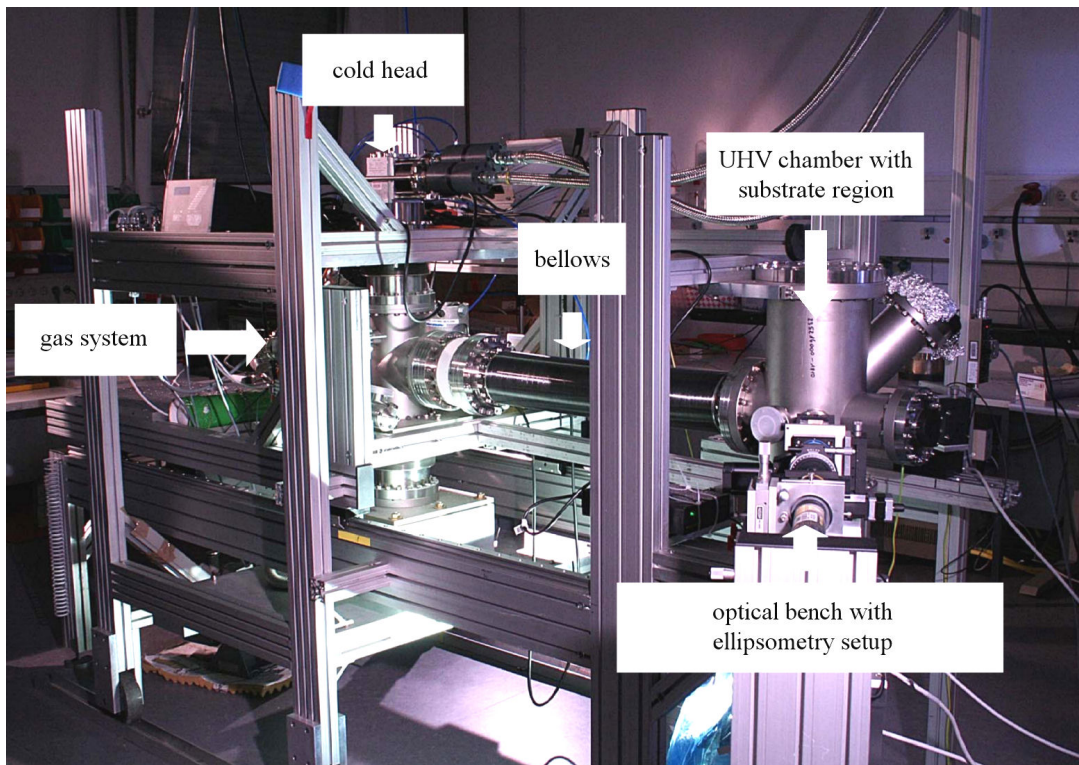


Figure 3.2.: **The CKrS** as it is set up in Münster. The main components are the gas system at the rear end, the cold head which cools down the substrate region, the bellows which allow for the necessary mobility for adjustments, maintainance and upgrades of the substrate region, the UHV chamber containing the substrate and radiation shields as well as the detector setup for the ellipsometry and the optical bench with the ellipsometry setup. Picture [Sch11].

3.2.1. The gas system

The automated gas system is able to release reproducible amounts of gas into the substrate region inside the UHV chamber. It is possible to choose stable Kr gas for reference measurements or the ^{83m}Kr gas for count rate measurements and switch between these on demand. Stable Kr is used to test the functionality of the gas system [Sch11] and to

determine the connection between the changes in the polarization of light in ellipsometry measurements and the film thickness (chapter 4).

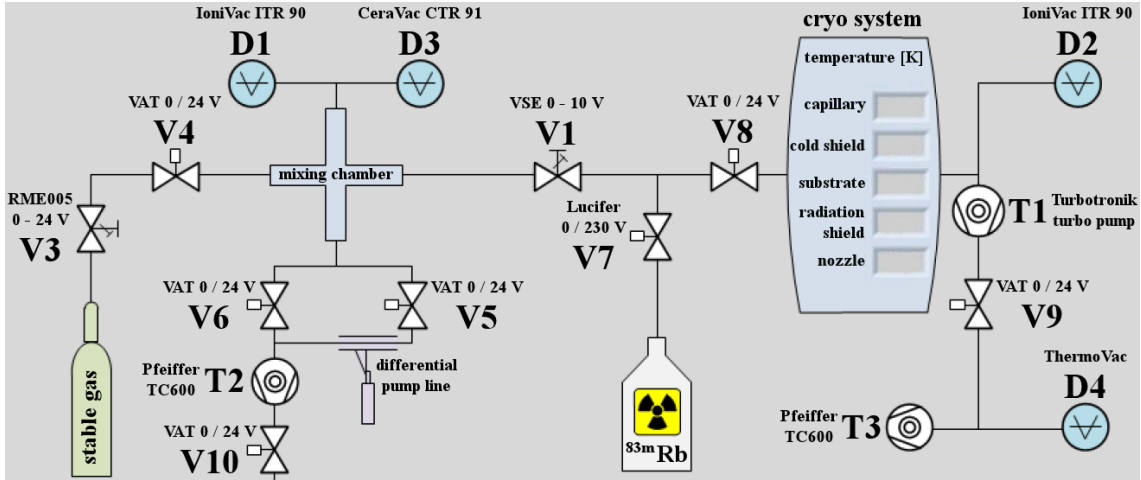


Figure 3.3.: **The gas system.** This is the operating interface of the LabVIEW program for the CKrS. Valves can be remotely operated and the pressures and temperatures of the different components can be monitored.

In measurements with stable Kr, the gas is first guided into the mixing chamber. Here the pressure for the inlet into the vacuum chamber is set. It usually is around 2 mbar. The gas flow Q is proportional to the pressure difference Δp

$$Q = L \cdot \Delta p, \quad (3.4)$$

where L is the conductance value. Since partial pressure at the substrate is of the order 10^{-12} , the gas flow is almost solely caused by the pressure in the mixing chamber. Via valve **V1**⁵ the amount of gas that travels through the capillary to the substrate region can be regulated by varying the valve opening and the opening time. In case of power failure **V8** closes off the substrate region⁶. After a time inside the mixing chamber the krypton will be contaminated with other sorts of gasses because of outgassing from the chamber walls. Because of the low pressure inside the mixing chamber the percentage of residual gas can get rather high, that's why during measurement times the mixing chamber should be purged by the valve- and pump system below the chamber (figure 3.3) and filled with fresh gas every couple of days (ideally 3 to 4). A baratron (**C3**) which is independent of the type of gas and a full range manometer (**D2**) monitor the pressure inside the mixing chamber.

The radioactive ^{83m}Kr is produced by a solid ^{83}Rb source inside a container which can be tapped by opening **V7**. In a volume with only ^{83}Rb present an equilibrium between generation and decay of ^{83m}Kr is achieved after about 45 minutes [Smo08]. The gas flow is governed by the amount of ^{83m}Kr atoms inside the source and the molecular conductance of the capillary.

⁵**V1** is a thermomechanical full metal regulating valve.

⁶Note: In case of power failure **V1** will open fully (Closed at 12 V and fully open at 0 V). When power is returned **V8** will open again, yet because of a longer response time **V1** will fully close a few seconds later. This results in an uncontrolled gas inlet.

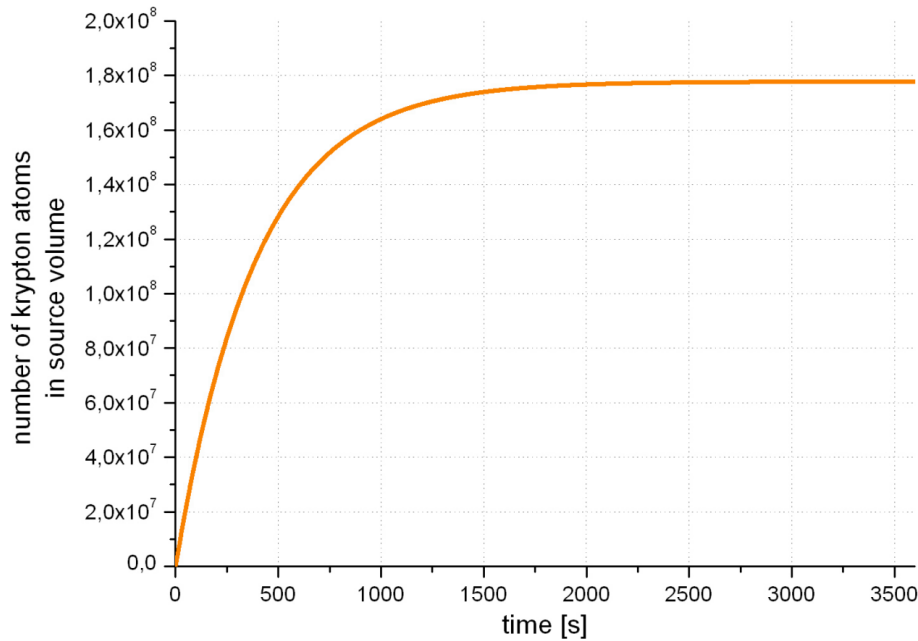


Figure 3.4.: **The production of ^{83m}Kr** in the source volume with initially no ^{83m}Kr atoms reaches saturation level after about 45 minutes. In this example the ^{83}Rb has an activity of $A_{\text{Rb}} = 455$ kBq. Figure [Smo08].

3.2.2. The cryogenic section

The cryosystem is based on a two-stage cooling unit (Sumitomo Heavy Industries Ltd., model: RDK 408D) with a cold finger attached. The HOPG substrate is mounted to the end face of the cold finger at a distance of about 1300 mm from the central axis of the cold head.

The first stage provides cooling power of 34 W at 40 K and is thermally connected to the outer radiation shield which protects the substrate from heat radiation from the UHV chamber walls. The cold finger with the substrate and the inner cold shield are connected to the second stage which can reach 4 K with a cooling power of 1 W. The inner radiation shield serves as a cold trap for residual gas and improves the vacuum in the substrate region. This and slightly heating the substrate to 25 — 30 K helps to reduce the amount of residual gas condensing onto the substrate. The temperatures of several key parts of the cryo system are monitored and displayed continually as seen in figure 3.3

Figure 3.5 shows a cross section of the cryo system in the region around the substrate. The radiation and cold shield have apertures on the sides which provide optical access for the ellipsometry. The aperture in front of the substrate is the outlet for the conversion electrons and inlet for the ablation laser beam. These measures for monitoring and cleaning are necessary to ensure the cleanliness of the substrate and with it the stability of the calibration line position. The cleanliness can be determined with the polarizer values in ellipsometry measurements after cleaning the substrate, called start values. A stability of ≈ 1 ppm⁷ over more than one month was achieved after ablation cleaning and continually

⁷Variation of the start values is less than 0.3°.

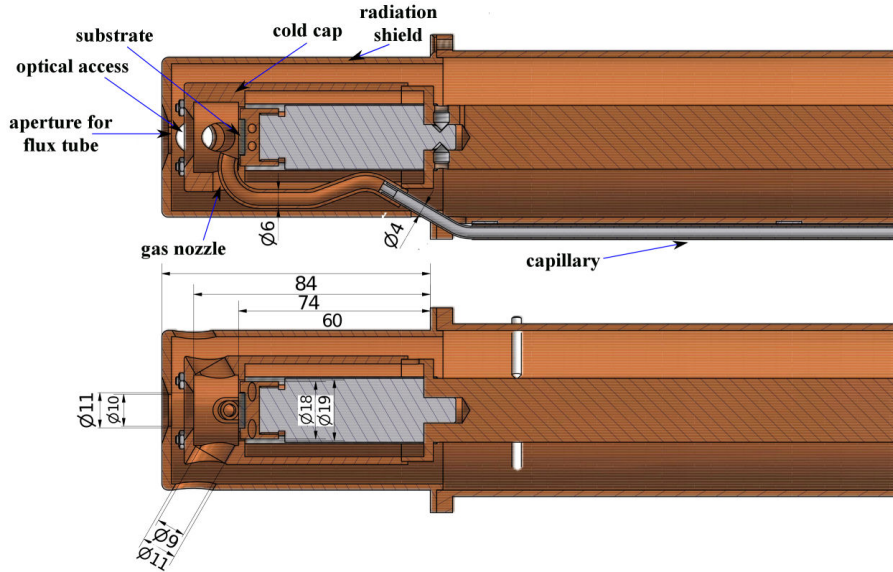


Figure 3.5.: **The substrate region of the CKrS** contains the HOPG substrate which is the heart of the CKrS. The capillary guides the Kr gas directly to the substrate. Figure adapted from [Ost08].

condensing ^{83m}Kr onto the substrate for about a week [Ost08].

The horizontal setup (figure 3.5) in which the CKrS is currently operated is not applicable for the KATRIN experiment. A new design has been created and will be put into practice after current tests and measurements are concluded. The completely redesigned substrate region amongst other things will be introduced in chapter 5.

3.2.3. The highly ordered pyrolytic graphite substrate

The heart of the CKrS is the **H**ighly **O**rded **P**yrolytic **G**raphite (HOPG) substrate, which is mounted to the cold finger. Graphite has a hexagonal structure is made up of layers which are held together by weak van de Waals forces. It has a lattice constant of 2.46 \AA and the distance between two layers is 3.35 \AA . Neighbouring layers are shifted by half a face diagonal which results in a ABAB... layer system as pictured in figure 3.6. The axis perpendicular to the graphene plains is called the c-axis.

HOPG is polycrystalline with a grain size of about $3 - 10 \text{ mm}$ and mosaic angles (angles between the c-axis of the crystal grains) of $0.4 \pm 0.1^\circ$ at highest quality (SPI-1). It also has a very smooth surface with steps of a few atomic layers which makes it suitable as a substrate for homogeneously condensed films.

Graphite is optically anisotropic due to being an uniaxial crystal. Anisotropic media are described can be characterized by an optical indicatrix:

$$\frac{x^2}{n_1^2} + \frac{y^2}{n_2^2} + \frac{z^2}{n_3^2} = 1 \quad (3.5)$$

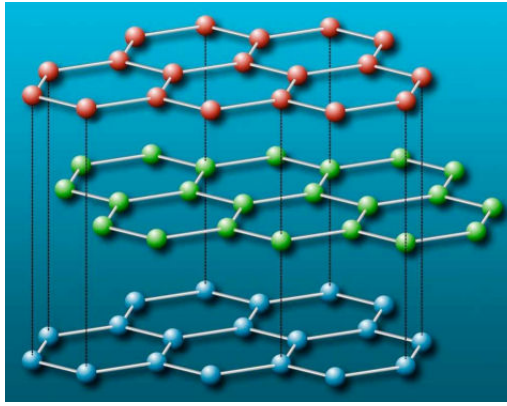


Figure 3.6.: **Structure of the HOPG substrate** [Ost08].

In uniaxial crystals $n_1 = n_2 = n_o$ is the ordinary and $n_3 = n_e$ is the extraordinary index of refraction⁸. Alternatively the HOPG substrate can be described by the “isotropic equivalent” where n_o from the anisotropic expression is the index of refraction [Vol89]. This simplification was successfully used in [Weg10].

⁸For biaxial crystals $n_1 \neq n_2 \neq n_3$.

4. Ellipsometry

Ellipsometry is a method for gaining information such as structure, film covering or film thickness of a sample. The polarization of light before and after the interaction with the sample are measured and a transformation matrix can be derived in form of a Jones matrix for non-depolarizing or a Müller matrix for depolarizing systems. More information on the polarization changes inside the system can be extracted by studying the inner processes of a system with focus on electromagnetic wave optics.



Figure 4.1.: **The common ellipsometry setup** includes a light source (**L**) which typically is a laser, a system of optical components to prepare a certain polarization state (**P**), a sample (**S**) which changes the polarization followed by an analyzer (**A**) which can be a linear polarizer and a detector (**D**) which measures the intensity of the transmitted light.

There are several different types of polarization changing processes which can yield different information about the sample:

- **Scattering** occurs when light passes through a medium with a spatially inhomogeneous refraction index.
- During **transmission** the polarization state of light changes continually along its way inside the sample which is caused by the optical anisotropy of the material. The transmission ellipsometry (or polarimetry) is mainly used for analyzing the molecular structure of materials in the field of physical chemistry.
- **Reflection or refraction** of light at the boundary surface between different media abruptly changes the polarization state due to different transmission- and reflection coefficients for s- and p-polarized light (see section 4.1). This “reflection ellipsometry” is the standard method for gaining information about the optical characteristics of a sample such as the index of refraction. It is also used for observing the increase (through adsorption or oxidation) or decrease (through desorption or sputtering) of the thickness of very thin films.

The CKrS, described in chapter 3, employs the method of reflection ellipsometry to monitor the changes on the substrate or its cleanliness. The underlying method of the **null ellipsometry** as well as the commonly used PCSA setup will be described in section 4.2.

4.1. Polarization of light

Light can be described as an electromagnetic plain wave. When light propagates through an optically isotropic medium the electric field \vec{E} , the magnetic field \vec{B} and the wave vector are perpendicular to one another with \vec{E} being defined as the polarization of the light. A polarized wave which propagates in z -direction can be described as [Nol02]:¹

$$\vec{E}(z,t) = E_x(z,t) \vec{e}_x + E_y(z,t) \vec{e}_y \quad (4.1)$$

with

$$\begin{aligned} E_x(z,t) &= E_{0x} \cos(kz - \omega t) \\ E_y(z,t) &= E_{0y} \cos(kz - \omega t + \phi). \end{aligned} \quad (4.2)$$

Three special cases of polarization can be distinguished depending on the phase shift ϕ :

- **linear polarization**

An electromagnetic wave is linearly polarized when

$$\phi = \pm k \cdot \pi, \quad k = 0,1,2,\dots \quad (4.3)$$

The electric field vector \vec{E} oscillates along a straight line in the xy -plane.

If light is reflected at a surface two polarization states are distinguished. If \vec{E} oscillates perpendicularly to the plane of incidence the term s-polarization applies. In a cartesian coordinate system where \vec{e}_x lies in the plane of incidence this means $E_x = 0$ and

$$\vec{E}(z,t) = E_y \vec{e}_y \cos(kz - \omega t). \quad (4.4)$$

On the other hand if \vec{E} oscillates in parallel to the plane of incidence ($E_y = 0$) it is called p-polarization².

$$\vec{E}(z,t) = E_x \vec{e}_x \cos(kz - \omega t) \quad (4.5)$$

- **circular polarization**

Circular polarization is achieved when the amplitudes of the partial waves are equal ($E_x = E_y = E_0$) and the phase difference is

$$\phi = \pm(k + \frac{1}{2}) \cdot \pi, \quad k = 0,1,2,\dots \quad (4.6)$$

There are two types of circular polarization:

$$\vec{E}(z,t) = E_0(\vec{e}_x \cos(kz - \omega t) \pm \vec{e}_y \sin(kz - \omega t)) \quad (4.7)$$

“+” means the light is right hand polarized and $\phi = +\pi/2$

“−” means the light is left hand polarized and $\phi = -\pi/2$

¹The amplitudes $E_x(z,t)$ and $E_y(z,t)$ are usually complex numbers. In the context of these considerations however it is sufficient to use the real parts.

²The expressions p- and s-polarization stem from the german words “parallel” and “senkrecht” (perpendicular).

- **elliptical polarization**

In every other case, the light is elliptically polarized.

When a monochromatic plane wave k_1 encounters a boundary surface between two non magnetic, non dissipative and isotropic media with different refractive indices n_1 and n_2 , it is partially transmitted k_2 and partially reflected k_3 (figure 4.2).

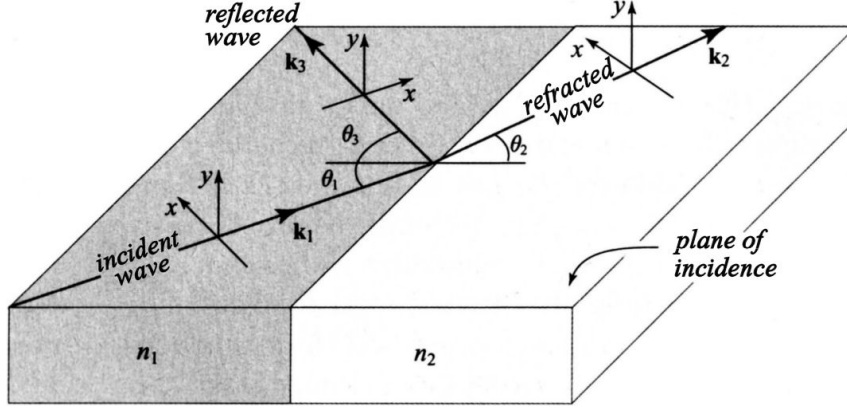


Figure 4.2.: **Reflection and transmission of light at a boundary surface.** The plane wave (k_1) encounters the boundary surface at an angle of incidence θ_1 which is equal to the angle of reflection θ_3 . The angle of refraction θ_2 can be calculated from the incidence angle with Snell's law (equation 4.8). The plane in which the incident and the reflected wave propagate is called the plane of incidence. (Figure adapted from [Sal08].)

The angle of refraction is calculated by applying Snell's law for refraction:

$$n_1 \sin\theta_1 = n_2 \sin\theta_2 \quad (4.8)$$

The amplitudes of the incident, the refracted and the reflected wave are described by Jones vectors³.

$$\vec{E}_1 = \begin{pmatrix} E_{1x} \\ E_{1y} \end{pmatrix} \quad \vec{E}_2 = \begin{pmatrix} E_{2x} \\ E_{2y} \end{pmatrix} \quad \vec{E}_3 = \begin{pmatrix} E_{3x} \\ E_{3y} \end{pmatrix} \quad (4.9)$$

The reflected and the refracted wave can be brought into relation to the incident wave by Jones matrices \mathbf{t} for transmission properties and \mathbf{r} for reflection properties:

$$\vec{E}_2 = \mathbf{t}\vec{E}_1 \quad (4.10)$$

$$\vec{E}_3 = \mathbf{r}\vec{E}_1 \quad (4.11)$$

The polarizations in x - and y -direction are independent from each other and both independently fulfill the conditions of continuity at the boundary surface in its tangential components \vec{E} and \vec{H} as well as the normal components \vec{D} and \vec{B} . Figure 4.2 shows the definition of the x - and y -direction. The x -component is parallel to the plane of incidence and a wave with a polarization in x -direction is called p-polarized. A wave polarized in y -direction on

³The scalar components E_{ix} and E_{iy} ($i=1,2,3$) specify the part of each wave in equation 4.9 which is polarized parallel (E_{ix}) and perpendicular (E_{iy}) to the plane of incidence.

the other hand is called s-polarized. Due to the independence of those two polarization states the Jones matrices \mathbf{t} and \mathbf{r} take on a diagonal form.

$$\mathbf{t} = \begin{bmatrix} t_x & 0 \\ 0 & t_y \end{bmatrix} \quad \mathbf{r} = \begin{bmatrix} r_x & 0 \\ 0 & r_y \end{bmatrix} \quad (4.12)$$

From equation 4.10 and 4.11 then results:

$$E_{2x} = t_x \cdot E_{1x} \quad E_{2y} = t_y \cdot E_{1y} \quad (4.13)$$

$$E_{3x} = r_x \cdot E_{1x} \quad E_{3y} = r_y \cdot E_{1y}. \quad (4.14)$$

Considering the continuity condition the transmission coefficients t_x and t_y and reflection coefficients r_x and r_y result in:

$$r_p = r_x = \frac{n_2 \cos\theta_1 - n_1 \cos\theta_2}{n_2 \cos\theta_1 + n_1 \cos\theta_2} \quad (4.15)$$

$$r_s = r_y = \frac{n_1 \cos\theta_1 - n_2 \cos\theta_2}{n_1 \cos\theta_1 + n_2 \cos\theta_2} \quad (4.16)$$

$$t_p = t_x = (1 + r_p) \frac{\cos\theta_1}{\cos\theta_2} \quad (4.17)$$

$$t_s = t_y = (1 + r_s) \quad (4.18)$$

These equations are known as the **Fresnel equations** thus the matrix coefficient are called Fresnel coefficients. As mentioned above, the angle θ_2 can be calculated from θ_1 , n_1 and n_2 with equation 4.8:

$$\cos\theta_2 = \sqrt{1 - \left(\frac{n_1}{n_2}\right)^2 \sin^2\theta_1} \quad (4.19)$$

Since the term under the square root can be negative the Fresnel coefficients are complex:

$$r_p = |r_p| \cdot e^{i\delta_p} \quad (4.20)$$

$$r_s = |r_s| \cdot e^{i\delta_s} \quad (4.21)$$

The $|r_p|$ and $|r_s|$ as well as the phase shifts δ_p and δ_s show different behavior depending on the wave's angle of incidence and the consideration of inner ($n_1 > n_2$) or outer reflection ($n_1 < n_2$).

4.1.1. P-polarized light

Figure 4.3 shows the behaviour of an incident wave at the boundary surface as a function of the angle of incidence θ_1 , for the case $n_1 < n_2$.

- Below or at the Brewster angle⁴ $\theta_B = \arctan\left(\frac{n_2}{n_1}\right)$ r_p is real and negative with $|r_p|$ dropping from $\frac{n_1 - n_2}{n_1 + n_2}$ at $\theta_1 = 0^\circ$ to 0 at $\theta_1 = \theta_B$ and $\delta_p = \pi$.
- If $\theta_1 > \theta_B$ r_p is real and positive and $|r_p|$ goes from 0 at θ_B to 1 at 90° with $\delta_p = 0$.

⁴The Brewster angle only plays a role in the reflection of p-polarized light.

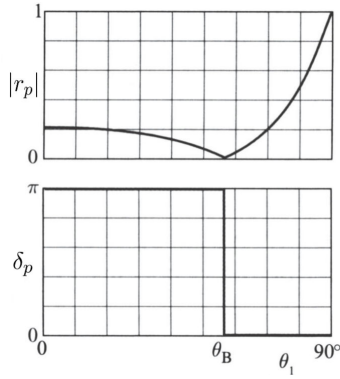


Figure 4.3.: **Outer reflection of p-polarized light** ($n_1 < n_2$) [Sal08].

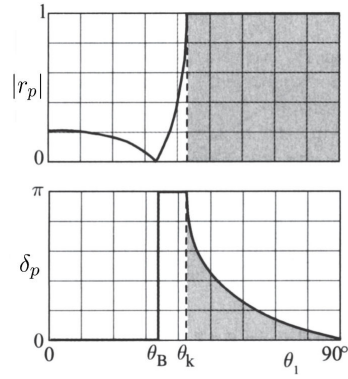


Figure 4.4.: **Inner reflection of p-polarized light** ($n_1 > n_2$) [Sal08].

For the inner reflection (figure 4.4) there are two critical angles at which $|r_p|$ and δ_p change their behavior. The first is the Brewster angle, the second is θ_k above which there is total reflection and no refracted partial wave can develop. The angle of total reflection applies to s- as well as p-polarized waves in inner reflection.

- For $\theta_1 \leq \theta_B$ r_p is real and positive with $|r_p|$ dropping from $\frac{n_1 - n_2}{n_1 + n_2}$ at $\theta_1 = 0^\circ$ to 0 at $\theta_1 = \theta_B$ and δ_p jumping from 0 to π at θ_B .
- If the incident angle lies between both critical angles ($\theta_B < \theta_1 \leq \theta_k$) r_p is real and negative with $|r_p|$ rising from 0 at θ_B to 1 at θ_k and $\delta_p = \pi$.
- In case of inner total reflection ($\theta_1 > \theta_k$) r_p is complex and $|r_p| = 1$. δ_p however continually drops according to $\delta_p = 2 \cdot \arctan \left[\frac{-1}{\sin^2 \theta_k} \sqrt{\frac{\cos^2 \theta_k}{\cos^2 \theta_1} - 1} \right]$ [Sal08].

4.1.2. S-polarized light

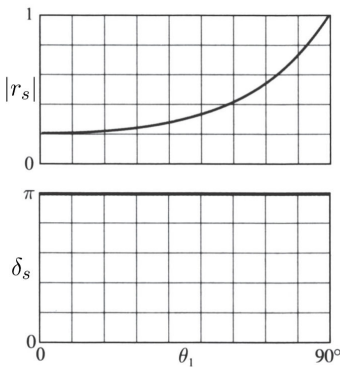


Figure 4.5.: **Outer reflection of s-polarized light** ($n_1 < n_2$) [Sal08].

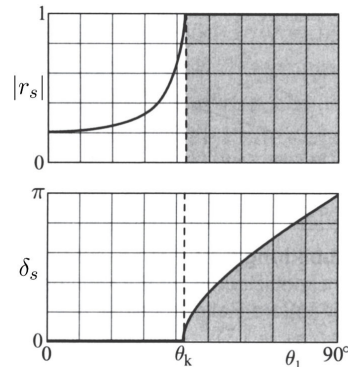


Figure 4.6.: **Inner reflection of s-polarized light** ($n_1 > n_2$) [Sal08].

With the outer reflection (figure 4.5) r_s remains real and negative for all angles of incidence. $|r_s|$ continually rises from $\frac{n_2 - n_1}{n_1 + n_2}$ at $\theta_1 = 0^\circ$ to 1 at 90° and $\delta_s = \pi$.

- In inner reflection, r_s is real and positive for $\theta_1 \leq \theta_k$ with $|r_s|$ rising from $\frac{n_1-n_2}{n_1+n_2}$ at $\theta_1 = 0^\circ$ to 1 at θ_k and $\delta_s = 0$.
- Above θ_k there is again total reflection and r_s is complex. Here $|r_s| = 1$ and $\delta_s = 2 \cdot \arctan \left[\sqrt{\frac{\cos^2 \theta_k}{\cos^2 \theta_1} - 1} \right]$ (Information and figures: [Sal08]).

4.2. Measuring film thickness with reflection ellipsometry

The ellipsometry setup at the CKrS in the institute of nuclear physics, WWU Münster is capable of measuring the coating thickness of krypton and residual gas on the HOPG substrate as well as its cleanliness after heating and/or ablation. The measured variable is the polarization of laser light which changes during the reflection at the substrate.

The following considerations concern a 3-layer system as depicted in figure 4.7. The vacuum, film and substrate are assumed to be homogeneous and optically isotropic⁵ and their complex refraction indices are N_0 , N_1 and N_2 . The film thickness d influences the phase difference δ of the reflected partial waves to one another. The change in the polarization of a light wave which is subject to multiple beam interference is measured as a function of the film thickness.

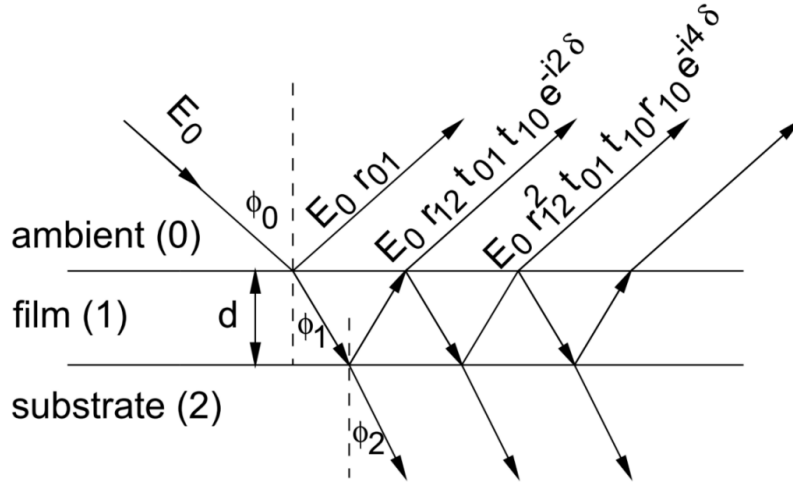


Figure 4.7.: **Reflection and transmission of a plane wave at a multiple layer system** [Ost08]. The 3-layer system (vacuum - film - substrate) is assumed to have plane and parallel surface boundaries. The parameters are the film thickness d , the angle of incidence ϕ_0 , the refraction angles ϕ_1 inside the film and ϕ_2 inside the substrate, the phase angle δ and the complex Fresnel coefficients for reflection and transmission r_{01} , r_{10} , r_{12} , t_{01} and t_{10} .

An incident plane wave with an amplitude E_0 encounters the film (surface boundary **01**) at an angle of incidence ϕ_0 . Part of the wave is reflected with a reflection coefficient

⁵HOPG is an optically anisotropic material. This fact is considered in section 3.2.3.

r_{01} and the other part is transmitted with a transmission coefficient⁶ t_{01} at an angle of

$$\phi_1 = \arcsin\left(\frac{N_0}{N_1} \cdot \sin\phi_0\right). \quad (4.22)$$

The transmitted partial wave then hits the boundary surface **12** between the film and the substrate and again part of the wave is reflected, the amplitude now being $E_0 t_{01} r_{12}$, and the other part enters the substrate at the angle $\phi_2 = \arcsin(N_1/N_2 \cdot \sin\phi_1) = \arcsin(N_0/N_2 \cdot \sin\phi_0)$ and is absorbed by the substrate.

The partial wave $E_0 t_{01} r_{12}$ is again partially reflected at the boundary surface **10**. The transmitted partial wave $E_0 t_{01} r_{12} t_{10}$ interferes with the first reflected partial wave $E_0 r_{01}$.

The optical retardation (Δs) between the partial wave having traveled through the film and the partial wave inside the vacuum is considered in the phase factor $e^{-i2\delta}$. Figure 4.8 shows how the optical retardation arises.

$$\Delta s = 2N_1 l_1 - N_0 l_0 \quad (4.23)$$

The distance travelled in vacuum is

$$\begin{aligned} l_0 &= 2d \tan\phi_1 \sin\phi_0 \\ &= 2d \frac{N_1}{N_0} \sin\phi_1 \end{aligned} \quad (4.24)$$

and the distance travelled inside the film

$$2l_1 = \frac{2d}{\cos\phi_1}. \quad (4.25)$$

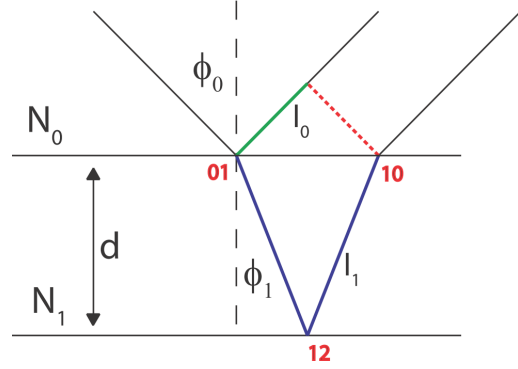


Figure 4.8.: The optical retardation during reflection at a thin film [Weg10].

Inserting these expressions into equation 4.23 produces:

$$\Delta s = 2dN_1 \cos\phi_1 = 2d\sqrt{N_1^2 - N_0^2 \sin^2\phi_0}. \quad (4.26)$$

This results in a change of the phase angle δ as a consequence of d

$$\delta = \frac{2\pi}{\lambda} d \sqrt{N_1^2 - N_0^2 \sin^2\phi_0} \quad (4.27)$$

which by convention considers only half of the optical retardation in medium N_1 . This is corrected by the factor 2 in the phase factor $e^{-i2\delta}$.

The sum of all the partial waves which are reflected back into the vacuum is an infinite geometric series and constitutes the complex total reflected amplitude R of the incident light wave amplitude:

$$R = r_{01} + t_{01}t_{10}r_{12}e^{-i2\delta} + t_{01}t_{10}r_{10}r_{12}^2e^{-i4\delta} + t_{01}t_{10}r_{10}^2r_{12}^3e^{-i6\delta} + \dots \quad (4.28)$$

The limit of a geometric series with $|q| < 1$ is

$$\sum_{k=0}^{\infty} a_0 q^k = \lim_{n \rightarrow \infty} \sum_{k=0}^n a_0 q^k = \frac{a_0}{1 - q} \quad (4.29)$$

⁶The derivations in this section apply to p- and s-polarized alike. Therefore, the Fresnel coefficients are not labeled p or s.

Using this, R becomes:

$$R = r_{01} + \frac{t_{01}t_{10}r_{12}e^{-i2\delta}}{1 - r_{10}r_{12}e^{-i2\delta}} \quad (4.30)$$

With the relations [Azz87]

$$r_{10} = -r_{01} \quad (4.31)$$

$$t_{01}t_{10} = 1 - r_{01}^2 \quad (4.32)$$

equation 4.30 can be converted to

$$R = \frac{r_{01} + r_{12}e^{-i2\delta}}{1 + r_{10}r_{12}e^{-i2\delta}} \quad (4.33)$$

This equation is valid for p- as well as for s-polarized light ($j = p, s$):

$$R_j = \frac{r_{01j} + r_{12j}e^{-i2\delta}}{1 + r_{10j}r_{12j}e^{-i2\delta}}. \quad (4.34)$$

The change in amplitude and phase in relation to the incident wave becomes clear when the complex total reflected amplitudes R_p and R_s are considered as a function of their absolute value and phase ($j = s, p$):

$$R_j = |R_j|e^{i\delta_{R_j}}. \quad (4.35)$$

Due to different reflection and transmission properties of p- and s-polarized light at a boundary surface the total reflection coefficients R_p and R_s are different. In an experiment, the ratio between the two coefficients is determined by observing the polarization state before and after the reflection:

$$\rho = \frac{R_p}{R_s} = \frac{r_{01p} + r_{12p}e^{-i2\delta}}{1 + r_{10p}r_{12p}e^{-i2\delta}} \cdot \frac{1 + r_{10s}r_{12s}e^{-i2\delta}}{r_{01s} + r_{12s}e^{-i2\delta}}. \quad (4.36)$$

Using equation 4.35 this ratio can be described as

$$\rho = \tan\Psi e^{i\Delta} \quad (4.37)$$

where

$$\Psi = \arctan\left(\frac{|R_p|}{|R_s|}\right) \quad (4.38)$$

includes the change in the amplitudes of p- and s-polarized light during reflection and

$$\Delta = \delta_{R_p} - \delta_{R_s} \quad (4.39)$$

reflects the difference in the respective phase shifts.

4.2.1. Null ellipsometry

Determination of the ratio ρ can be achieved by using a PCSA setup for the null ellipsometry (figure 4.9). The light is prepared by the rotating polarizer P and the fixed compensator C to be linearly polarized after reflection at the substrate-film complex. The analyzer A is rotated in order to cancel the light intensity which is monitored by the detector D. If the light still reaches the detector the polarizers P and A are adjusted accordingly.

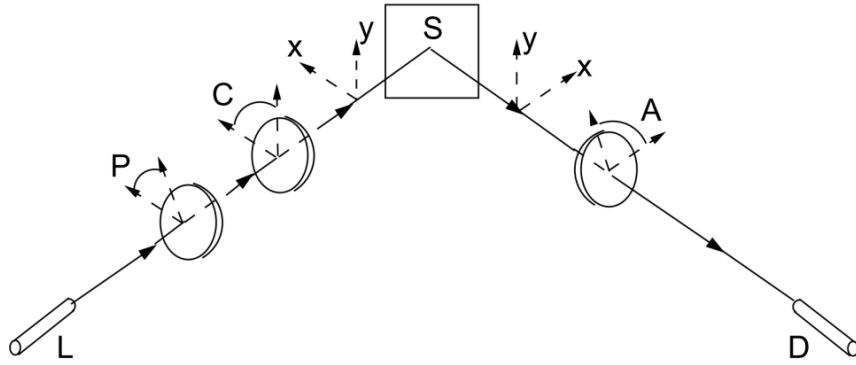


Figure 4.9.: **The null ellipsometry setup** consists of a light source L, two linear polarizers P and A, a compensator C, a sample S and the detector D. Figure [Ost08].

The setup utilized in the institute of nuclear physics at WWU Münster consists of the following items:

- The light source is a 543.5 nm He-Ne laser and
- the compensator C is a quarter-wave retarder.
- The adjustment of P and A (in PC ellipsometry P and C (see section 4.3)) is done by an automated LabVIEW program which was initially developed by A. Wegmann [Weg10].
- The reference (zero) position for the polarizers P, A and the compensator C is the positive x-direction in figure 4.9. The position values increase counterclockwise when looking towards the light source.

The changes in the polarization of light when propagating through the optical setup can be determined by analyzing the system using Jones vectors for the light and Jones matrices for the optical components. Assuming the components are optically ideal the Jones matrices in the respective coordinate systems are:

$$\text{linear polarizer} \quad T_{LP}^{te} = K_{LP} \begin{bmatrix} 1 & 0 \\ 0 & 0 \end{bmatrix} \quad (4.40)$$

$$\text{compensator} \quad T_C^{fs} = K_C \begin{bmatrix} 1 & 0 \\ 0 & \rho_C \end{bmatrix} \quad (4.41)$$

$$\text{sample} \quad T_S^{xy} = \begin{bmatrix} V_{ex} & 0 \\ 0 & V_{ey} \end{bmatrix} \quad (4.42)$$

The exponents in equations 4.40, 4.41 and 4.42 denote the polarization eigenstates of the respective component. The linear polarizer has a transmitting and an extinguishing axis while the compensator has a fast and a slow axis and the sample has an x-axis parallel to the plane of incidence and a y-axis perpendicular to it. The PCSA system is described by multiplying the Jones matrices in the order of the optical components in the setup while after each element a transformation into the coordinate system of the next element is necessary which is achieved by using the appropriate rotation matrix⁷. Calculations with

⁷A detailed example of the calculations of such a system can be found in [Spi11].

this method yield a detected signal of [Azz87]

$$\mathcal{J}_D = \text{const.} \cdot |L|^2 \quad (4.43)$$

with

$$\begin{aligned} L = & V_{ex} \cos A [\cos C \cos(P - C) - \rho_C \sin C \sin(P - C)] \\ & + V_{ey} \sin A [\sin C \cos(P - C) + \rho_C \cos C \sin(P - C)]. \end{aligned} \quad (4.44)$$

Thus, the signal depends on the azimuthal angles of P, C and A, ρ_C of the compensator and the complex eigenvalues V_{ex} and V_{ey} of the optical system. The aim of null ellipsometry is the correct alignment of P, C and A so that no light at all reaches the detector:

$$\mathcal{J}_D = 0 \quad (4.45)$$

This is achieved when

$$L = 0. \quad (4.46)$$

Using this condition as a solution for equation 4.44 the ratio ρ_S between the eigenvalues of the system can be determined:

$$\rho_S = \frac{V_{ex}}{V_{ey}} = -\tan A \frac{\tan C + \rho_C \tan(P - C)}{1 - \tan C \tan(P - C)} \quad (4.47)$$

The compensator, in this case being a quarter-wave retarder, produces a phase shift of $\delta_C = -\pi/2$ between the fast and the slow axis. This makes ρ_C :

$$\rho_C = T_C \cdot e^{i\delta_C} = -i \quad (4.48)$$

If the compensator is fixed to the angle of $\pm\pi/4$ between its fast axis and the plane of incidence equation 4.47 becomes

$$\rho_S = \mp \tan A e^{\mp 2i(P \mp \pi/4)} \quad \text{for } C = \pm \frac{\pi}{4} \quad (4.49)$$

There are two combinations of polarizer and analyzer positions at which no light passes through to the detector⁸:

$$(P, A) \quad \text{and} \quad (P', A') = (P - \pi/2, \pi - A) \quad (4.50)$$

Henceforth this type of null ellipsometry will be called PA ellipsometry in reference to P and A being observables in this kind of measurements. Here the compensator remains fixed at $\pm \pi/4$ between its fast axis and the plane of incidence.

4.3. The PC ellipsometry

Installation at the KATRIN experiment requires changing the CKrS setup to make it applicable. This section deals with the conditions at the CPS (see chapter 5) which have to be considered and the necessary modifications to the ellipsometry setup. The concept for

⁸Adjusting P and A by $n \cdot \pi$ ($n \in \mathbb{Z}$) yields of course the same results.

the new design will be introduced in chapter 5. A preliminary setup has been developed to simulate the conditions at the CPS. The modifications resulted in a new type of ellipsometry which was tested to determine its usability and to compare with the results from the PA ellipsometry published in [Weg10]. Also the underlying theory to the PA ellipsometry was extended to make the new data comparable to PA data.

An important feature of the PA ellipsometry setup and also cause for the setup changes are the vacuum windows at the UHV chamber which houses the substrate. The rotating polarizer and analyzer are mounted outside the vacuum chamber and operated at room temperature. The analyzer and detector are positioned as close as possible to the substrate to avoid loss of information from the diverging reflected beam. This divergence is caused by the slightly uneven substrate. However, the conditions at the CPS do not allow for this kind of setup because:

- There are no vacuum windows near the substrate for the reflected beam to leave the vacuum chamber. The only window available would be the one through which the ellipsometry laser beam is coupled into the CPS and that is at a distance of ≈ 2 m to the substrate. This would lead to a great loss of information since much of the reflected beam would not leave through such a distant window.
- There is little space inside the CPS for a rotary table for the analyzer. Technically, installing a rotator which could work inside the relatively strong magnetic field would be possible, however any viable solution would produce disproportional expenses.

4.3.1. The preliminary PC ellipsometry setup

The preliminary setup with the modified ellipsometry circumvents these restrictions (figure 4.10). The light source (a) consists of the He-Ne laser, a neutral density filter (F) which allows regulating the intensity and a linear polarizer (P) and quarter wave retarder ($\lambda/4$) to achieve a highly circularly polarized light. The circular polarization of the light ensures an unchanging intensity behind the following polarizer (b) independent of its orientation. This polarizer is mounted to a rotary table (company: PI, model: M-060.DG) with a minimal accuracy of $200 \mu\text{rad}$ ($\hat{=} 0.0115^\circ$) when moving to a certain position [PI]. If all movement is unidirectional the repeatability of a position lies at $50 \mu\text{rad}$ ($\hat{=} 0.0029^\circ$). The compensator (c) is a quarter wave retarder which is also mounted to a rotary table. Behind the compensator the light is polarized elliptically (or in special cases linearly or circularly) depending on the angle between the orientation of its optical axes and polarization state after the linear polarizer.

Through a vacuum window with an antireflective coating (d), the light enters the UHV chamber where it is reflected at the substrate-film-system (e). At a certain combination of polarizer angle (P), compensator angle (C) and a film of given physical (film thickness and composition) and optical (index of refraction) properties the light after reflection at the substrate is polarized linearly and can be compensated by the fixed analyzer (f). The detector (g) is a Si-PIN diode (Hamamatsu type S-3590-19) and monitors the intensity behind the analyzer. A remotely controlled current amplifier (Femto DLPCA-200) amplifies the signals of a few pA which are then digitalized by a 12 bit ADC (h).

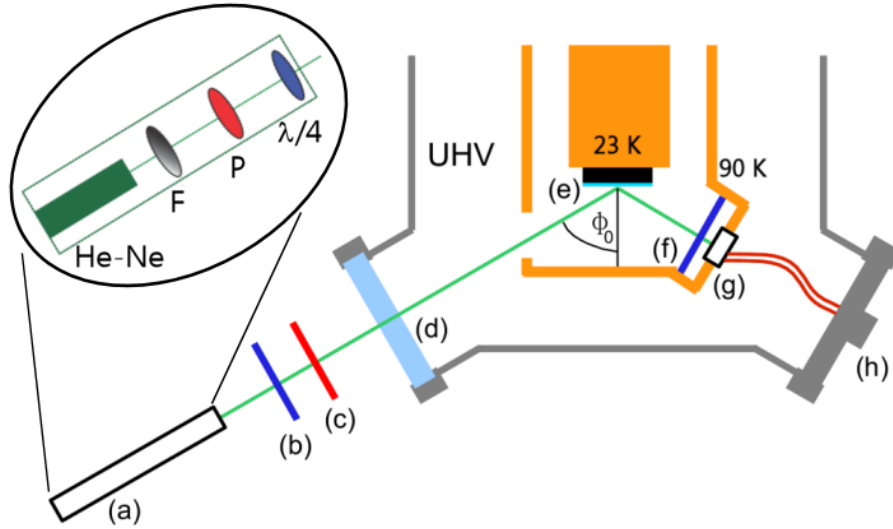


Figure 4.10.: **Ellipsometry setup with analyzer and detector inside the UHV chamber** containing the usual ellipsometry components such as the light source (a) which provides circularly polarized light with adjustable intensity, the polarizer (b), the compensator (c), the sample (e), the analyzer (f) and the detector (g). Additionally, there is one vacuum window (d) to couple the laser beam into the vacuum chamber and an electric feedthrough (h) for the detector cable. For clarity, the inner cold shield which surrounds the substrate and is kept at ≈ 12 K is not displayed. Figure combined from originals in [Bau12] and [Weg10].

The rotary tables are computer controlled and in the course of a measurement the P and C positions for cancelling the light are searched for and assumed. From the resulting data set which includes the positions P and C and the light's intensity, the position of the minimum can be calculated.

The novelty of this setup is that the analyzer is fixed at $+30^\circ$ with respect to the plane of incidence while the compensator is mounted on a rotary table. This makes P and C the observables of such a measurement and the name **PC ellipsometry** was chosen to distinguish this method from the PA ellipsometry.

4.3.2. Analysis of PC ellipsometry data

Since the raw data from the PC ellipsometry measurements are not directly comparable to the PA data, the PC data have to be converted. Starting point for the following considerations is equation 4.47 which has to be valid for any kind of null ellipsometry in a PCSA setup. Using the Euler formula ρ_S can also be characterized by

$$\alpha \cdot e^{i\beta} = \rho_S = -\tan A \frac{\tan C + \rho_C \tan(P - C)}{1 - \tan C \tan(P - C)}. \quad (4.51)$$

Now coordinates \tilde{P} and \tilde{A} are defined in such a way that the left part of equation 4.51 becomes

$$\rho_S = \tan \tilde{A} \cdot e^{2i(\tilde{P} + \pi/4)} \quad (4.52)$$

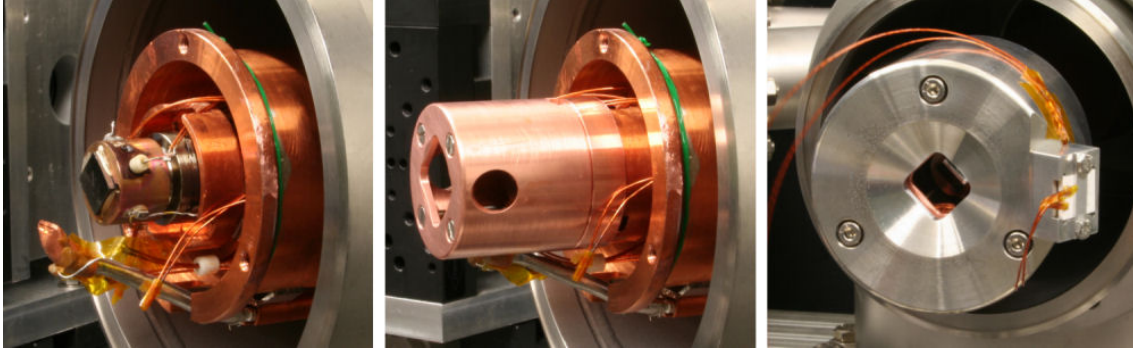


Figure 4.11.: **The substrate and detector.** The left picture shows the substrate on which the films are prepared and the nozzle at the end of the capillary through which the krypton gas is guided. There are cables for the temperature probe and the resistive heater. The inner radiation shield (12 K) which is connected to the second stage of the cryocooler is displayed in the middle. In the right picture, the outer cold shield (90 K) which holds the detector (white housing) and a temperature probe is shown. The analyzer is located beneath the detector.

which resembles equation 4.49 for $C = -\pi/4$. This makes

$$\tilde{P} = \frac{\beta}{2} - \frac{\pi}{4} = \frac{\arg(\rho_S)}{2} - \frac{\pi}{4} \quad (4.53)$$

and

$$\tilde{A} = \arctan \alpha = \arctan |\rho_S|. \quad (4.54)$$

If at a certain film thickness the values P and C are measured, these can be converted to \tilde{P} and \tilde{A} values which would be obtained in PA ellipsometry at the same film thickness. This allows for easy comparison between the PA and PC data. In practice this means that the same analysis tools can be used and the PC data sets only have to be fed into a conversion program⁹ and the corresponding $\tilde{P}\tilde{A}$ data sets are produced.

First test results of the new setup can be found in [Spi11]. Figures 4.12 and 4.13 are an example for the conversion of PC-data into $\tilde{P}\tilde{A}$ data from current measurements [Bau12].

A fit program for the PA data, called *elli.cpp*, was developed by A. Wegmann and T. Schäfer in 2010. The program varies up to five fit parameters for the isotropic equivalent. These are the angle of incidence and the refractive indices and absorption coefficients of the film and the substrate. The effects of varying each parameter are described in [Weg10]. Optionally the parameters for an anisotropic material can be added to the calculations. However, the time for the fit increases by at least one order of magnitude and the results do not differ significantly from those obtained without the anisotropic parameters.

⁹The conversion tool *umrechnung.cpp* was developed by D. Spitzer, and its function is described in [Spi11].

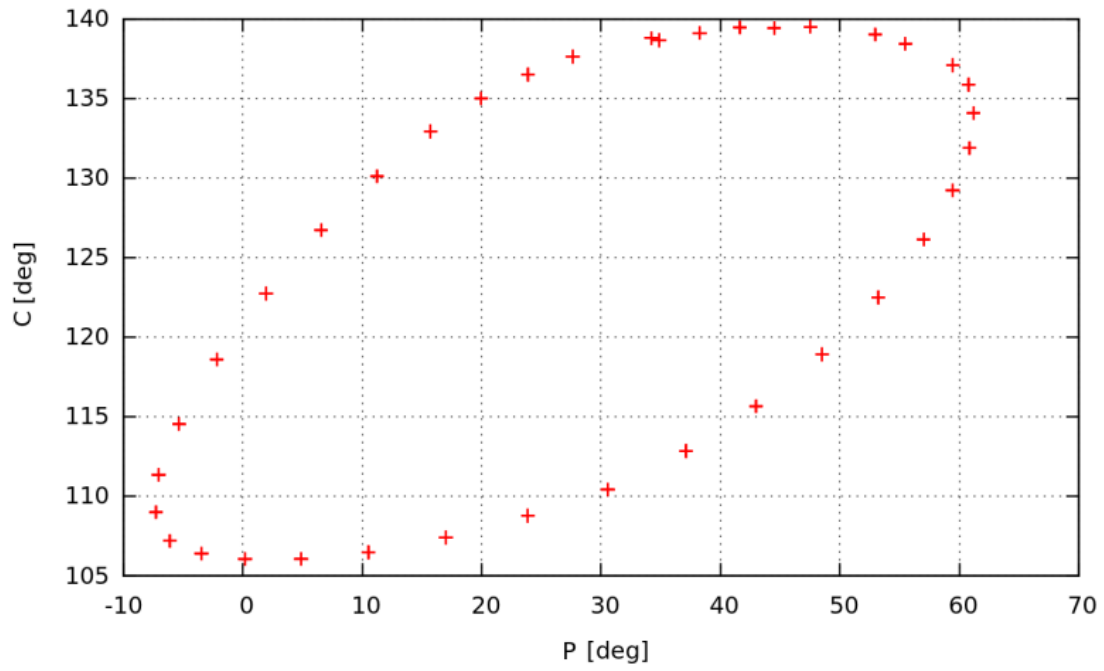


Figure 4.12.: **Raw PC data** from the measurement of an incremental krypton film preparation [Bau12].

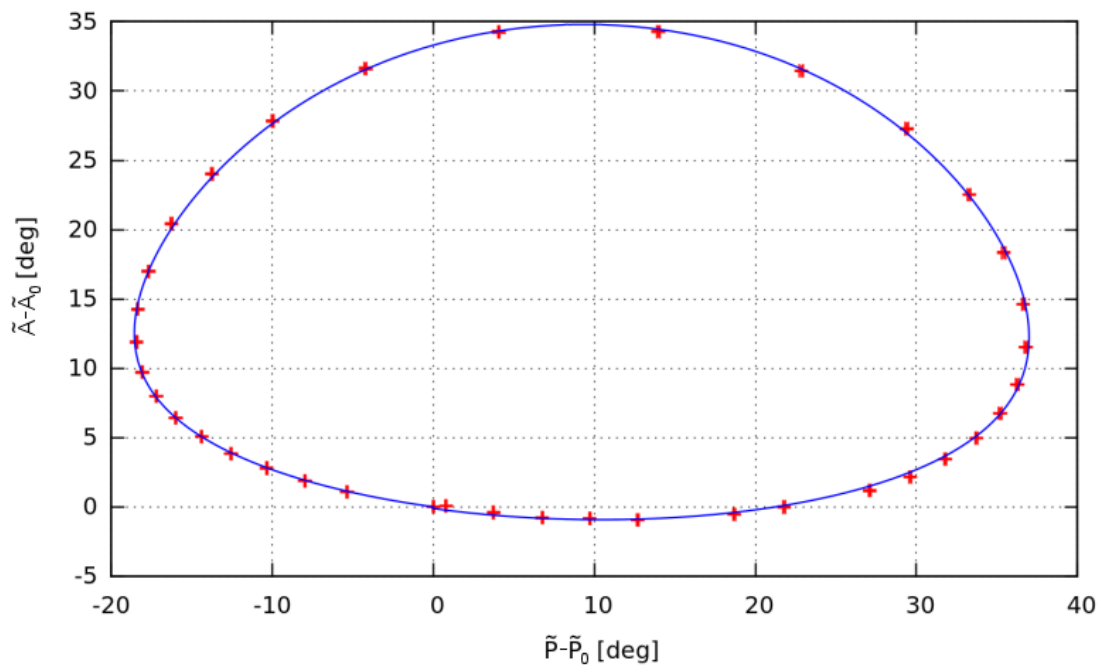


Figure 4.13.: **The converted $\tilde{P}\tilde{A}$ data** in values relative to \tilde{P}_0 and \tilde{A}_0 of a clean substrate. The blue line is a fit to the data points [Bau12].

5. Intergrating the CKrS into the CPS

The goal of the development of the CKrS is its application at the KATRIN experiment inside the **Cryogenic Pumping Section (CPS)** which was introduced in section 2.3.2. Figure 5.1 shows the place of installation for the CKrS which is in the forward section of the CPS directly behind the cold gate valve (V3).

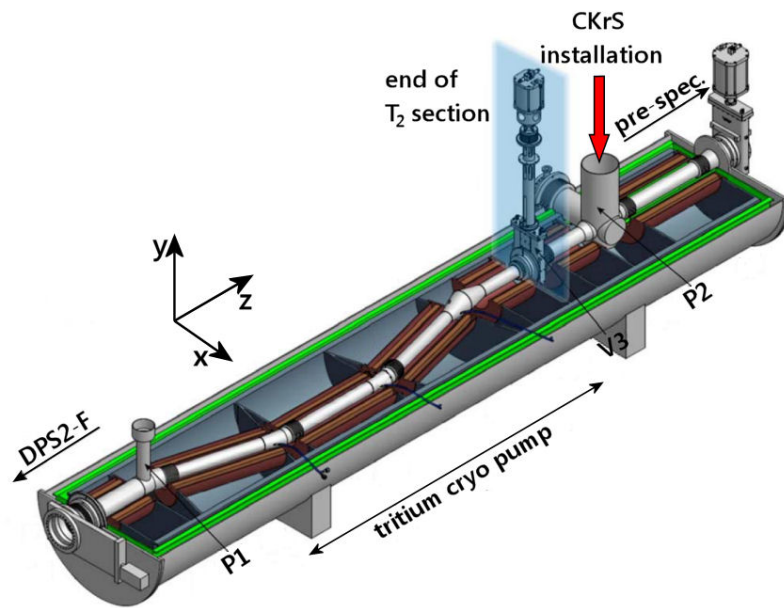


Figure 5.1.: **A longitudinal section through the CPS.** The CKrS is intended to be installed at the pump port no. 2 (P2) and will enter the CPS from above. The cold gate valve (V3) separates the tritium pumping section from the forward parts of the experiment. It is opened only during data taking. The origin of the coordinate system lies at the left end of the CPS in the center of the beam line. Figure adapted from [Gil10].

This chapter discusses of the specifics of the new design of the CKrS and its installation at the KATRIN experiment.

5.1. The substrate region

The CKrS, in its current form (see chapter 3) is unsuitable for direct installation at the KATRIN experiment. One reason for a new setup is the direction from which the CKrS enters the CPS and the direction in which the electrons are to be emitted. The substrate has to be relocated to the side of the cold finger which faces the detector and the radiation

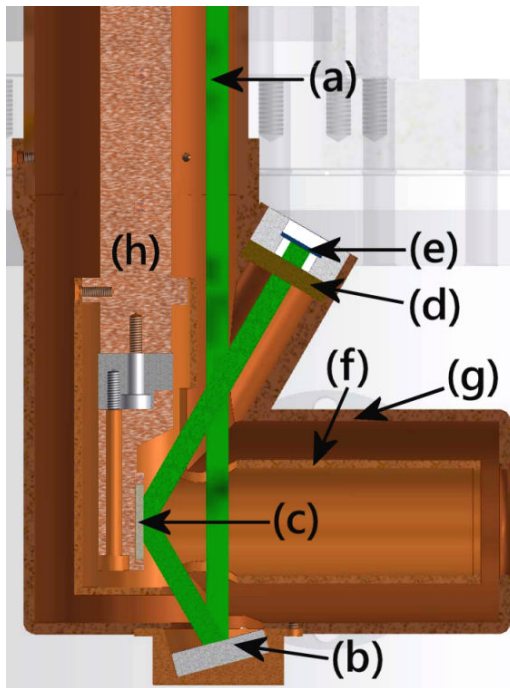


Figure 5.2: **The redesigned substrate region** basically consists of the same components as the preliminary setup with only one difference. The ellipsometry laser beam (a) has to be redirected by a mirror (b) before it is reflected at the substrate (c). After reflection it passes the analyzer (d) and its intensity is measured by the detector (e). The cold shield (f) and the radiation shield (g) protect the substrate from residual gas and heat radiation. Like in the preliminary setup, the analyzer and detector are mounted to the radiation shield. The cold finger (h) which is connected to the second stage of the cryocooler is cut longitudinally at its end to provide a plane for the substrate to be mounted on. Since the substrate has to be heated to prevent hydrogen from condensing onto it, the end part is thermally insulated from the rest of the cold finger by a piece of stainless steel (grey area). Design [Bau13].

shield and cold shield have to be adapted to fit this new orientation. Figure 5.2 shows the first draft of the redesigned substrate region.

The incident laser beam is guided towards the substrate between the cold finger and the surrounding copper tube which is connected to the first stage of the cryocooler. A dielectric mirror directs the light towards the $20 \times 20 \text{ mm}^2$ HOPG-substrate. Such mirrors can be manufactured to reflect light of a certain wavelength and angle of incidence without changing its polarization. The cold shield which is connected to the cold finger (second cooling stage) possesses apertures to allow the laser beam passage to the substrate and the detector. Both, the radiation shield and the cold shield have apertures in front of the substrate to let the conversion electrons leave the CKrS towards the spectrometer section. The length of the shields is approximately 10 cm. This is a compromise between the wish for good shielding (long shields) and the room available inside the CPS. The quality of the shielding relates to the maximum angle at which a residual gas molecule can enter the cold shield and still hit the substrate.

Figure 5.2 does not contain the capillary which is intended to run between the cold finger and the outer copper tube at the back side of the substrate. Plans are to split the capillary at the cold shield and have a nozzle at each side of the substrate so that the laser beam is not blocked. Also, an electron detector has been developed and is currently being reworked to monitor the electron flow from the WGTS. It will be positioned at the radiation shield of CKrS directly behind the substrate [Res11]. To reduce the signal noise, the preamplifier has to be close to the detector and in will most likely be mounted to the radiation shield as well.

5.2. Concept of the CKrS at the CPS

As indicated in figure 5.1 the CKrS enters the CPS from above and operates in the area of the T_2 - β -flux tube. Figure 5.3 shows the CKrS in operating position. The three main sections are colored grey, red and blue. The cryo- and pumping section (grey) contains the cold head (a) and a turbo molecular pump (b). These are decoupled by bellows (c) from the rest of the setup to avoid vibration during operation therein. Here also the vacuum window (d) is provided for the ellipsometry laser beam to enter into the vacuum region.

The cryo- and pumping section is electrically insulated from the ablation section (red) by a ceramic insulator (e). This separation is required when a voltage is applied to the CKrS in order to accelerate the conversion electrons from the ^{83m}Kr to pass the potential barriers inside the spectrometers. The bellows (f) allows the CKrS to be moved from the operating position inside the CPS to the ablation chamber (g) which sits on top of a CF250 all-metal gate valve (h, company: VAT, type: 48148-CE44). The bellows (company: COMVAT, custom made) can be elongated by as much as 120 cm from its shortest extension.

For cleaning purposes or during tritium and argon removal, the CKrS is moved back into the ablation chamber. At those occasions the gate valve will be closed. This way the CPS is not contaminated during ablation and during argon regeneration no tritium can reach the CKrS. The ablation chamber also holds a getter pump (SAES MK5) with a pumping speed of 240 L(H_2)/s (figure 5.4).

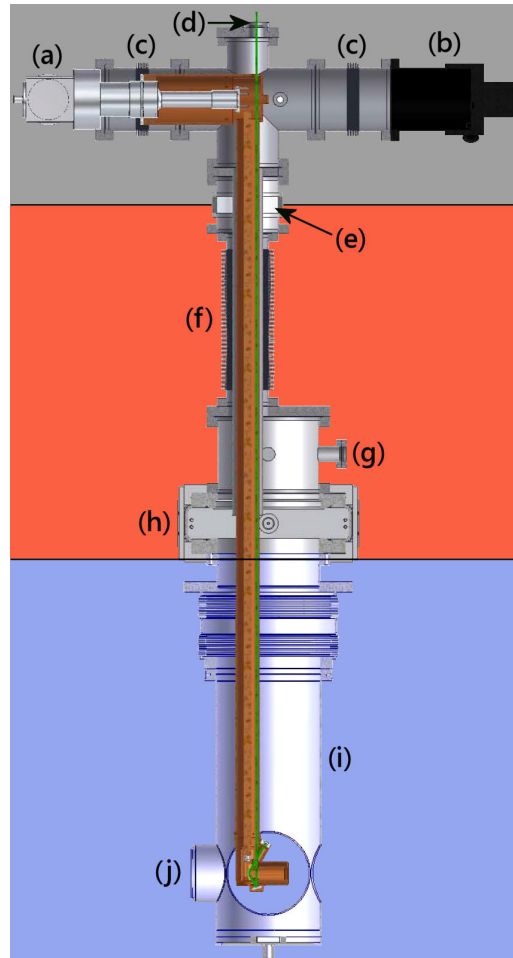


Figure 5.3.: **The CKrS at the CPS** in operating position. The details are found in the text beside the figure. Design [Bau13].

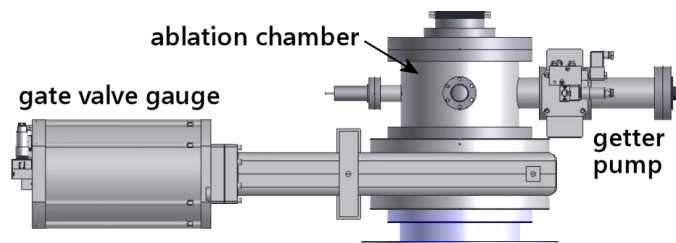


Figure 5.4.: **Front view of the ablation chamber.** Design [Bau13]

Beneath the gate valve (blue area) is the CPS (i) and the flux tube which is contained in the pipe to the left (j).

5.3. Moving the CKrS inside the CPS

During operation the CKrS will have to be moved to various positions inside the CPS. Since at pump port no. 2 no guiding magnets are present, the magnetic containment around the beam line drops there and the flux tube widens significantly (figure 5.5).

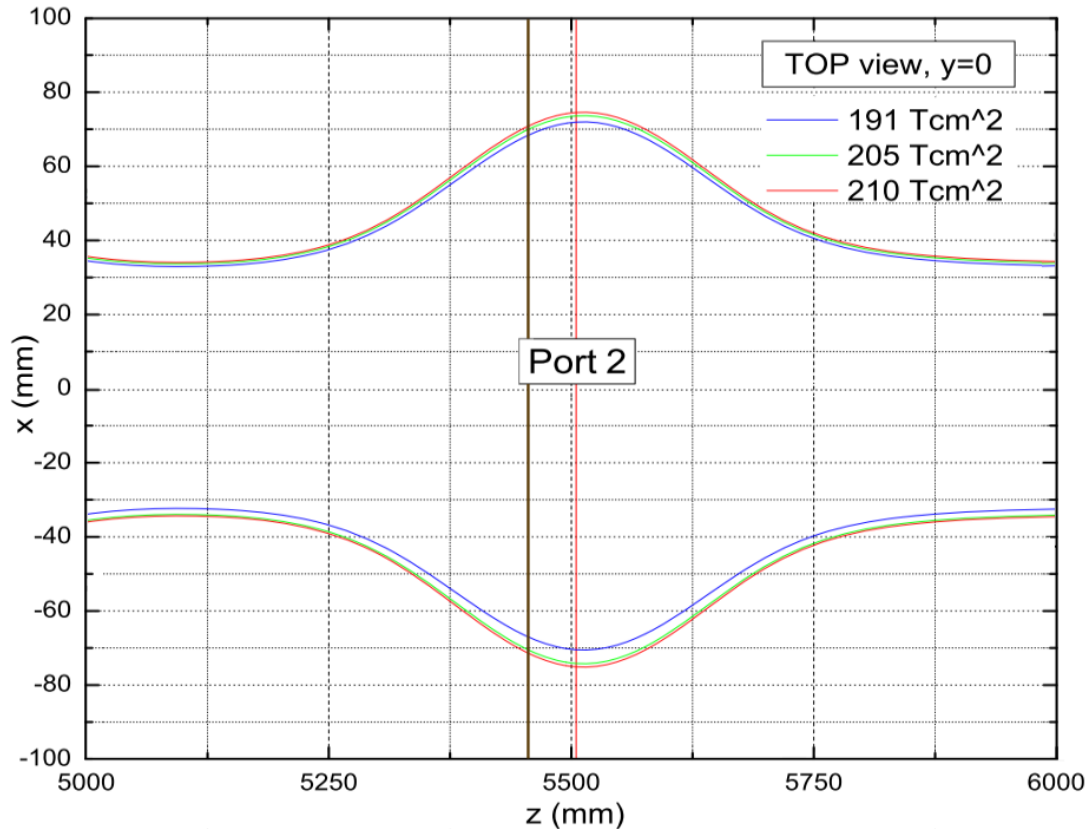


Figure 5.5.: **The flux tube** at the location of the CKrS has a diameter of ≈ 15 cm at its widest for $191 \text{ T} \cdot \text{cm}^2$ if all magnets of KATRIN are activated. The substrate of the CKrS will be moved in the x/y -plane at $z = 5455$ mm while the center of pump port 2 will be at $z = 5505$ mm when the CPS is in cold state. Figure [Gil11].

In order to scan the whole flux tube and thereby illuminate each detector pixel separately, the substrate has to be moved in a radius of about 7 cm around the center of the flux tube in the x/y -plane. For this reason, the CKrS will be mounted on a system of scaffolds and frames. This for one thing facilitates the necessary mobility and also allows separation of the vibrating parts from the rest of the setup. Figure 5.6 shows the first version of such a framework.

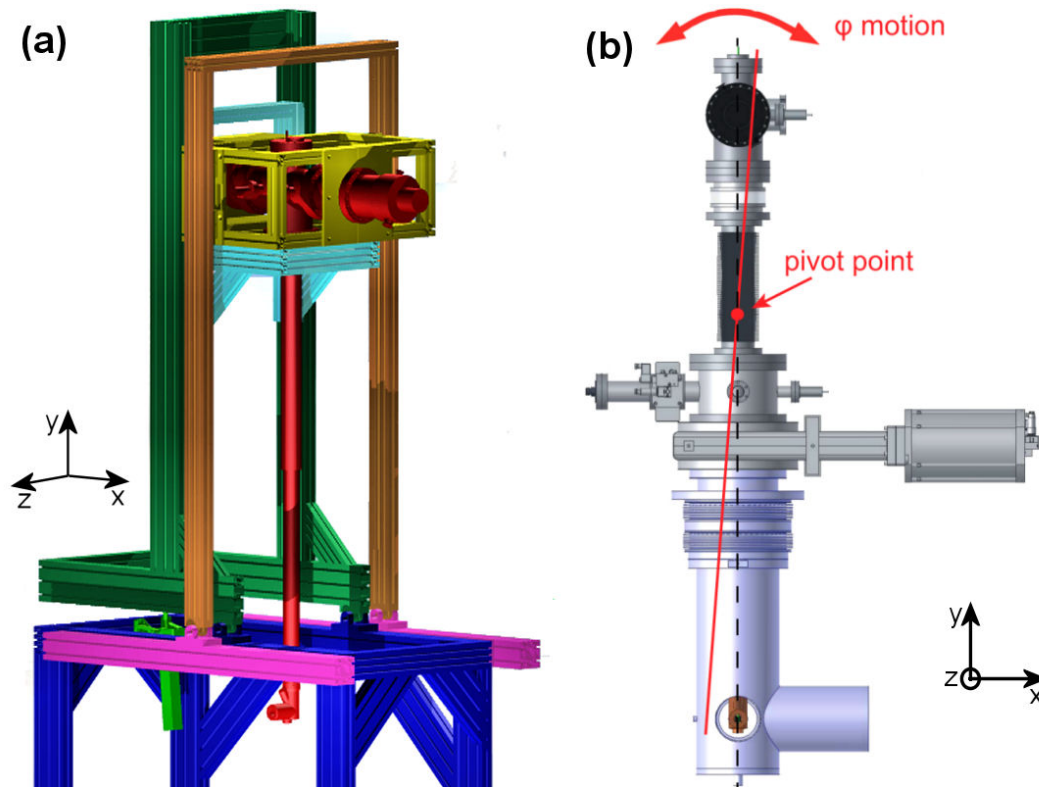


Figure 5.6.: **Moving the CKrS** is done in a framework (a). The TMP and cold head are fixed to the yellow frame which is guided by the brown outer frame in y -movement (up/down). This is pivot mounted to the magenta scaffold which stands on a platform above the CPS. The rest of the CKrS is mounted to the cyan frame and is guided by the green outer frame in y -movement. This for its part is pivot-mounted to the blue scaffold which stands on the ground floor. In this position the CKrS would be fully retracted from the CPS. In picture (a) the CKrS is depicted without the surrounding vacuum components. Picture (b) shows a frontal view of the new CKrS design. The pivot point lies inside the bellows. Designs (a) [Ort11], (b) [Bau13].

As noted above, certain parts of the setup are separated by bellows to avoid vibrations. These components also have to be mounted on separate frames. One frame holds the vacuum pump and the cold head while the other holds the vacuum chamber to which those vibrating components are connected via bellows. Each frame is guided by a different outer frame which are each mounted to different scaffolds. Both outer frames have the same pivot axis. In this configuration the CKrS can be tilted by up to $\pm 3.6^\circ$ which makes the scanning in x -direction (or, more precisely, in φ -direction) possible.

5.4. Motion control

The mobility of the CKrS will be provided by a system of servo motors, drive modules, lifting gear and a computer program which was programmed in LabVIEW. A test setup has been built to facilitate two-dimensional movement. Several functions were implemented

such as automated positioning along with position read-out, use of limit switches and setting a reference position for absolute position measurement.

Please note that the full extent of all the details to this topic cannot be covered in this work. For more information on special technical problems, the reader is kindly referred to the appropriate manuals and data sheets which are cited in the text. Appendix A comprises some details of the test setup and the LabVIEW program.

5.4.1. The test setup

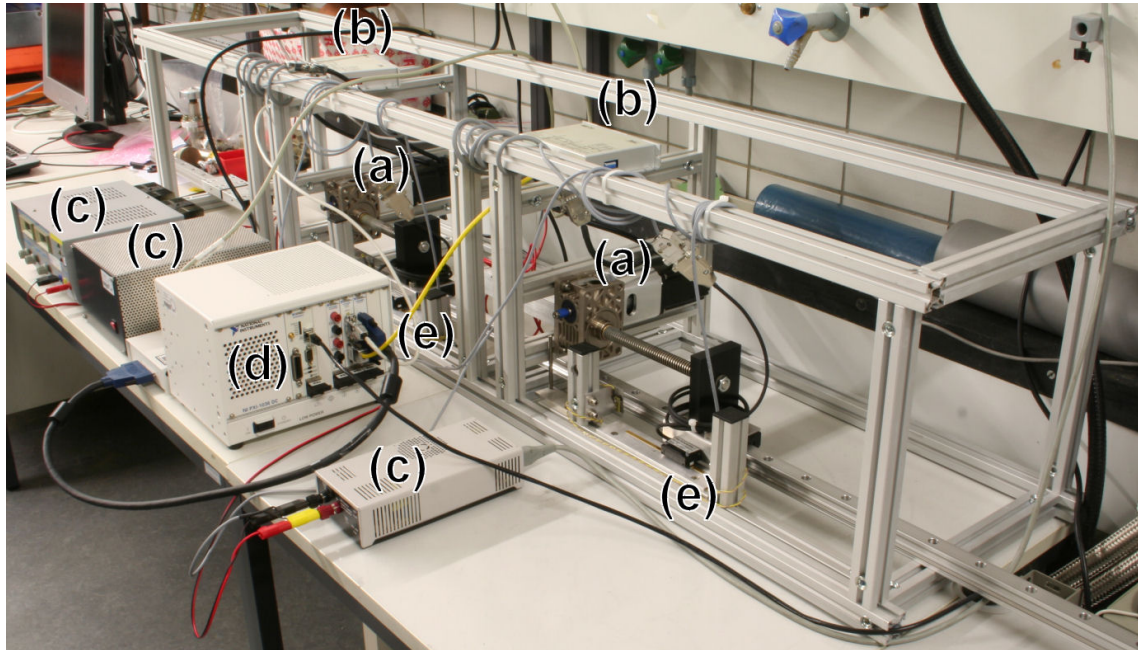


Figure 5.7.: **The test setup for the motorization of the CKrS.** The motors (a) and controllers (b) are supplied by the power supplies (c). The PXI computer (d) serves as a real time processor between the software and the drive modules. The signals from the optical positioning sensors (e) are also processed by the PXI computer.

The test setup (figure 5.7) consists of an aluminum skeleton made from Kanya extrusion in which the motors, lifting gears, limit switches and linear guiding for the moving parts are fixed. Basically the user provides commands such as “move to position x” or “define the zero for absolute position determination” which are put in via a standard PC which runs LabVIEW. The commands are processed on a real-time PXI computer which relays them to the drive modules. These modules are addressed via a CanOpen interface (some details will be discussed in section A.2) and supplies the motor with the necessary power for the movement. The position, velocity and acceleration are determined in terms of increments by the motor’s internal encoder. A certain number of increments constitute a motor revolution which in turn constitutes a certain feed from the shaft of the lifting gear (figure 5.8). A slide is fixed to the end of the shaft and can be moved back and forth on the linear guiding (figure 5.9). Its movement, however, is restricted by limit switches on either side.

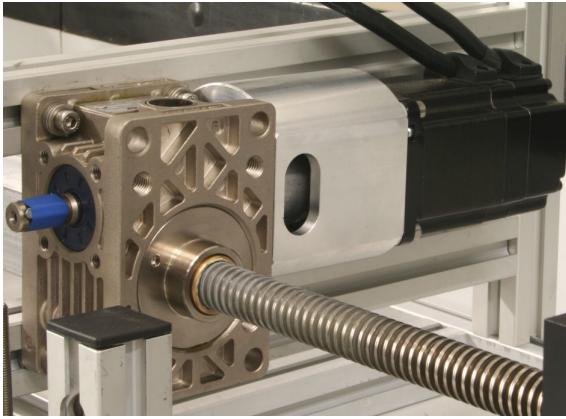


Figure 5.8.: **Motor and gear** are connected by a coupler. Depending on the rotating direction of the motor, the shaft is either extended or retracted.

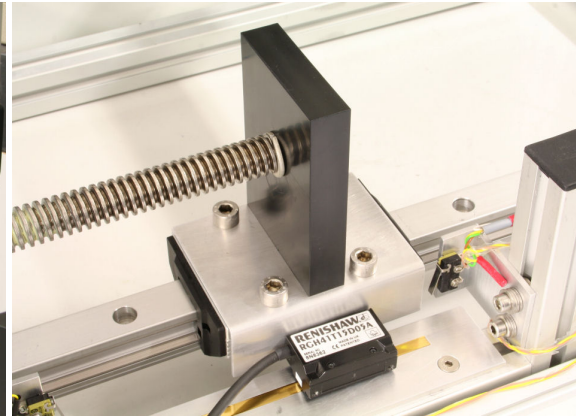


Figure 5.9.: **The slide** moves between the limit switches along the linear guiding and holds the sensor for absolute position determination.

A sensor which is attached to the slide moves over an optical scale and measures the current position (figure 5.10). The reference (zero) position can be defined by using a

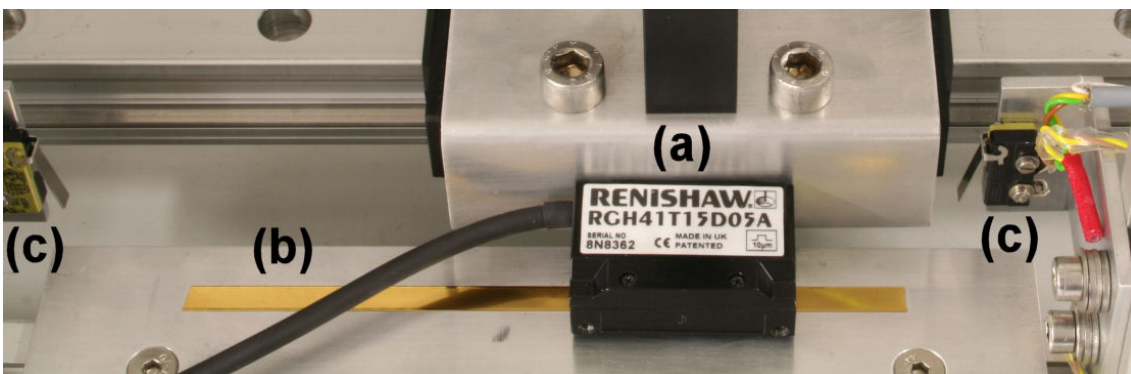


Figure 5.10.: **The position sensor** (a) reads its current position from the gold-plated steel scale (b) below. If it moves too far to the right or the left, the slide hits a limit switch (c) and the movement is discontinued.

certain function of the controller which allows movement until the limit switch break point is hit and the switching circuit is opened. Any offset before this break point can be chosen as the reference point. The LabVIEW program which will be covered in section 5.4.2 sets both encoders to zero at the reference point. If during normal operation a position beyond one of the break points is targeted, power to the motor will be cut by the drive module as soon as the limit switch circuit is opened.

The motors and gears

The motors in this setup (company: Isel, type: EC 60S without breaks) are brushless 3-phase servo motors and have a rated torque of 0.5 Nm^1 [Ise10]. Each motor drives a lifting gear (company: ZIMM, type: Z-5-SL), to which they are connected by a coupler. This type of motor comes with an integrated encoder which allows positioning and position read-out. The left cable in figure 5.8 connects the motor to the power supply, the right cable carries the encoder signals. Each is connected to a different connector at the drive module.

The default encoder resolution is 4000 increments (inc) per motor revolution. The gear translation ratio is 16:1 which means 16 motor revolutions make for one revolution of the gear shaft which in turn constitutes a feed of 4 mm [Noz07]. This results in an overall resolution of 16000 inc/mm or $16 \text{ inc}/\mu\text{m}$.

The drive module

Two of Isel’s IMD 20 drive modules (figure 5.11) are implemented in this setup. They are the central component of the motion control. Every other component is either directly or indirectly connected to them, except for the absolute position read-out system.

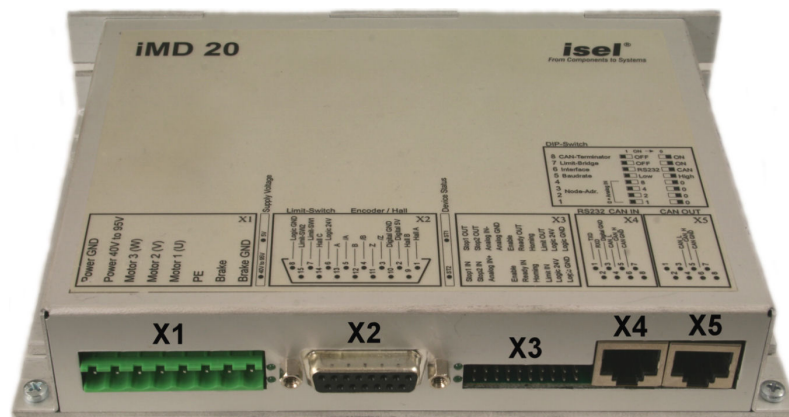


Figure 5.11.: **The IMD 20** controls the power supply (50 V) for the motor (X1), provides power for the encoder (5V) and handles its signals as well as limit switch read-out (X2). The X3 connector supplies the 24 V for the logic and X4 handles the control commands from the computer. The connector X5 allows synchronous control of several motors which, however, was not tested in the course of this work.

This drive module provides various modes of operation which have to be activated depending on the intended function. Normal operation in this setup requires the “profile position mode” which in turn requires a target position, velocity and acceleration to be entered before starting the motion. There is also a “homing mode” which allows the definition of a

¹Should this not be sufficient for the new CKrS setup, they could easily be substituted for EC 60L motors with a rated torque of 0.75 Nm.

reference position using a limit switch. If a limit switch is hit during normal operation and power to the motor is cut, the mode “moving the axis away from the limit switch” has to be activated. Only now a remotely controlled movement is possible. After the limit switch is closed again the “profile position mode” can be resumed [Ise08]. Some technical details on the IMD 20 drive module are provided in appendix A.1.

The PXI system



Figure 5.12.: **The PXI-system** consists of a chassis that holds several modules. The real-time controller module (slot 1), the CAN controller module (slot 4) and the timing- and digital-I/O module (slot 5) are required for the test setup.

PXI is a PC-based platform for measurement and automation systems which combines PCI bus features with the modular, Eurocard packaging of CompactPCI. Figure 5.12 shows the configuration of the PXI system in this setup.

Embedded into the chassis (PXI-1036DC) is a real-time (RT) controller (PXI-8146RT, slot 1) which is the computer in this system. It is connected to any other module in the chassis and receives their data or supplies the commands. A PC which runs LabVIEW serves as user interface and is connected to the RT-controller by an ethernet crossover cable. The LabVIEW program itself is loaded to and run on the controller during operation.

The CAN controller module (PXI-8464/2 series 2, slot 4) has two ports to each of which

an IMD 20 drive module is connected. Both ports are addressed separately with different sets of commands to allow independent control of both motors.

Slot 5 of the PXI chassis houses a counter/timer with digital I/O module (PXI-6602). This module receives a signal from the position sensor each time it passes an increment on the position scale. The signals from the counter along with the resolution of the sensor allow calculation of the current position.

The absolute position read-out

The absolute position read-out is an optical, linear distance measurement system in which all positioning issues of the CKrS and associated security measures are managed. The main components are the position sensor (company: Renishaw, type: RGH41T15D05A), the gold plated steel scale (company: Renishaw, type: RGS40-S), the limit switches and the signal processing elements (PXI-system, IMD 20 drive).

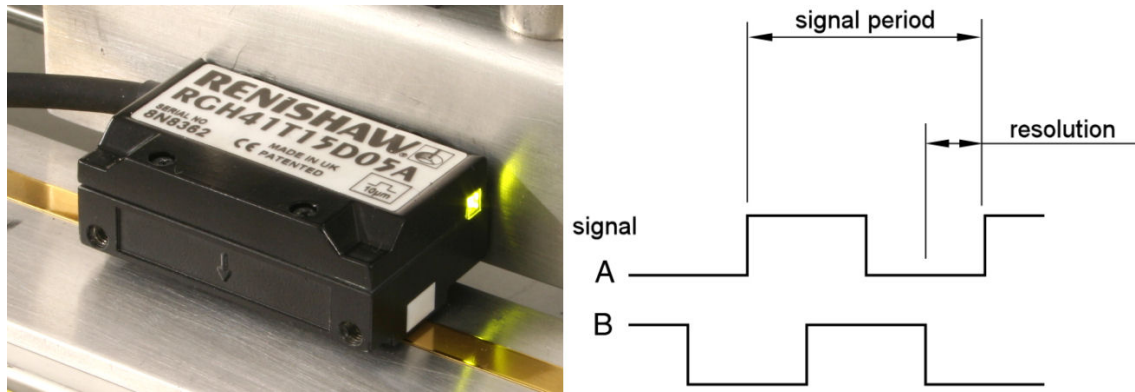


Figure 5.13.: **The position sensor** moves over the optical scale and produces two signals when passing an increment of the scale. Two signals A and B are produced. These are shifted by 90° . (Right figure adapted from original in [Ren08].)

The sensor (figure 5.13) produces two rectangular signals A and B with a signal period of $40 \mu\text{m}$ which is also the pitch of the optical scale. These signals are shifted by 90° . Since the edges of signal A have a distance of $1/4$ of a signal period to the closest edges of signal B, the sensor resolution is $10 \mu\text{m}$. These signals are fed to the counter module of the PXI system via a connector block (NI SCB-68, figure 5.14).

There are a few restrictions to the mounting of the sensor above the scale, since the measurement happens without contact. For example, the bottom side of the sensor head and the surface of the scale must be mounted in parallel with a maximum tilt of 1° in or across moving direction and the distance between them must be between 0.7 and 0.9 mm. Also, the edges of the scale and the long edges of the sensor head have to be parallel with a maximum contortion of 1° . The correct installation can be monitored by the LED at the side of the sensor. A green light means the sensor is mounted correctly. The light has to be green or at least orange along the entire traversing range. A red light indicates a faulty installation [Ren08].

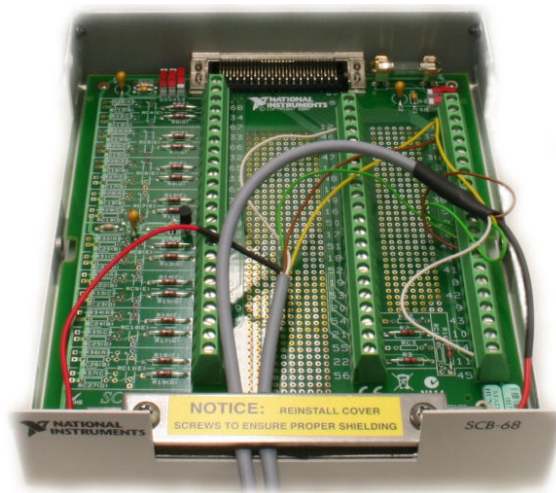


Figure 5.14.: **The connector block** connects the signal cables from the position sensors (grey cables) with the counter module by a cable at its back.

For absolute position measurement a reference point is required. This is provided by one of the limit switches in the setup. Here the limit switches are simple contact switches which are closed during positioning operation and open when hit by the slide. To acquire the reference position, the IMD 20 drive has to be set to “homing mode” and an offset from the switch point has to be chosen as the zero. In this setup the reference position is set to $100\ \mu\text{m}$ before the switch point.

The limit switches will be the hardware security measure at the CPS since this is a confined space. The area of movement will be strictly defined and limited to prevent improper use and damage. The bottom of the CPS will serve as reference point for CKrS positioning.

Using only the motor encoder for positioning would pose a risk, since it only counts motor revolutions. In case of a faulty coupling or other unforeseen malfunctions the positioning would be off and remain unnoticed.

Absolute positioning works by comparing the position value from a motor encoder with the value from the respective sensor. First the target position is assumed according to the motor encoder values. Then the difference to the motion sensor value is calculated and the position is adjusted accordingly. There is a backlash of $\approx 20\text{--}30\ \mu\text{m}$ between these values which is unavoidable but also negligible.

5.4.2. The LabVIEW VI

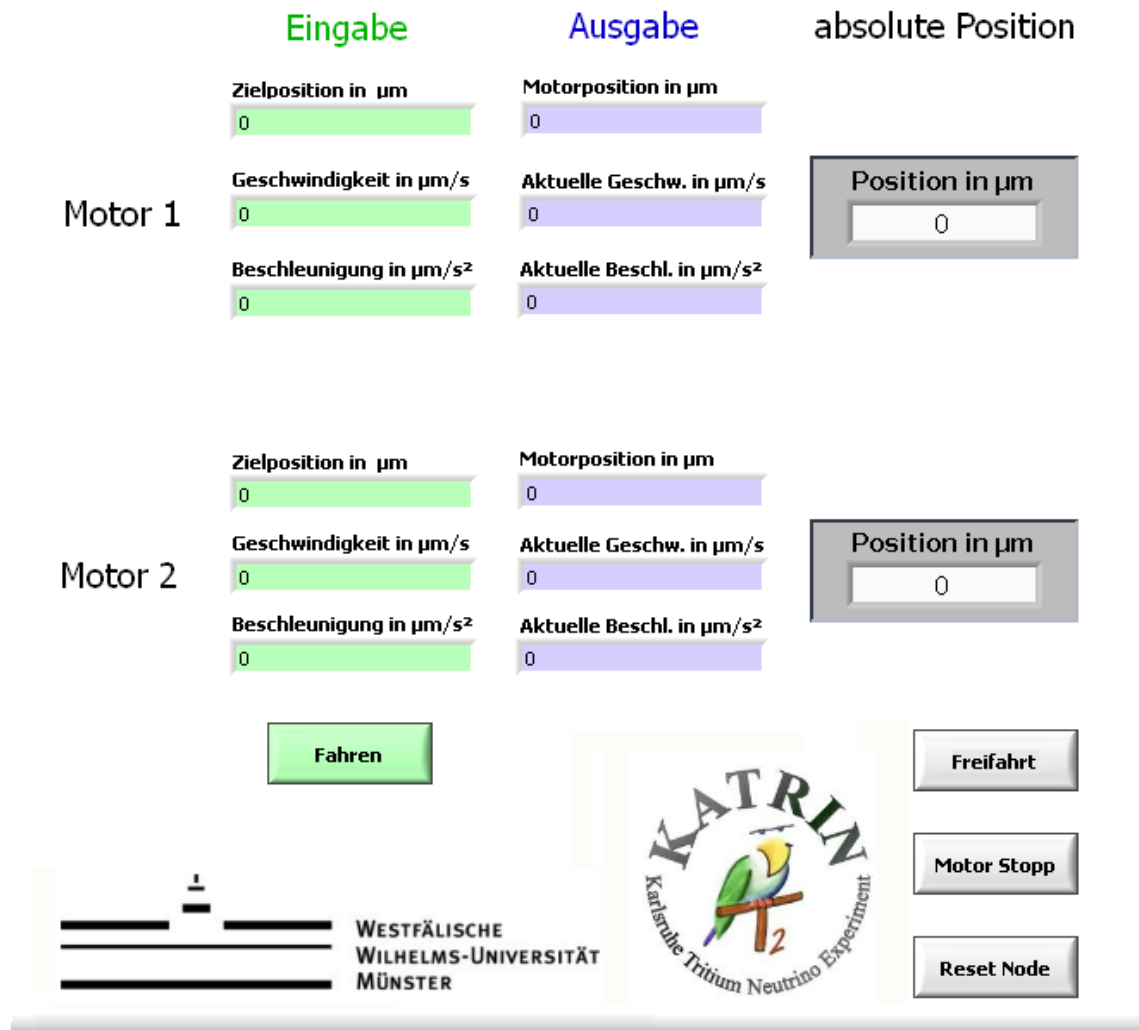


Figure 5.15.: The user interface for the motion control is written in LabVIEW and runs on a Windows PC.

The LabVIEW VI (Virtual Instrument), *Motorsteuerung_v2.vi*, is able to test all necessary functions of the future CKrS motor control. It allows a complete remote control of the motors and execution of several error correcting functions via a fairly straightforward user interface (figure 5.15).

When the VI is activated, after loading to the PXI system, the user is prompted by a pop-up window to select the type of motor to be initialized from a drop-down menu (left side of figure 5.16). There are two types to be chosen from, although currently only the EC 60S are installed in the setup. Initialization means that several parameters have to be set, for the motor to function properly. This for example includes the rated current of 6900 mA for the EC 60S or 10500 mA for the EC 60L which has to be provided by the IMD 20 drive. Also the conversion factor between encoder increments and user units, in this case μm , is



Figure 5.16.: **Pop-up windows** inform the user of the current step. Left: The user chooses a type of motor to be initialized. Right: The user has to stand by during homing mode.

set here. It is put in as numerator (16) and divisor (1) for both motors². This is also the value of the 16 inc/ μm ratio which was calculated in section 5.4.1.

After successful initialization, the drive module is set to “homing mode” and both slides are moved to their respective negative limit switch and then 100 μm away from the switch point. This is called homing offset and is preset to 100 user units (μm). Any other offset may be chosen at will. At the beginning of the homing procedure a pop-up window appears which informs the user of the ongoing activity (right side of figure 5.16). During this time no other function is possible. After the zero position is assumed the drive is set to “profile position mode” and the pop-up window vanishes.

Now normal operation can commence. The VI is designed to execute the basic function of targetting a desired position (μm) and assuming it at the desired speed ($\mu\text{m}/\text{s}$) and acceleration ($\mu\text{m}/\text{s}^2$). These three parameters can be put into the green boxes in the user interface. The upper cluster of boxes belongs to motor 1 (left motor in the setup) and the lower cluster to motor 2. The input is acknowledged by pressing the button “Fahren” and the motion begins. The blue boxes contain the current position, velocity and acceleration values for the motors. These position values are calculated from the number of increments the respective motor encoder counts. The absolute position values are displayed in the grey boxes.

There are three additional buttons which help to solve a number of problems that may arise during the operation. If a position beyond the break point of a limit switch was targeted and power to the motor is cut, the button “Freifahrt” sets the drive module to “moving out of the limit switch” mode, and automatically returns to a position before the break point. The button “Motor Stopp” cuts power to the motor. This function was used during testing to prevent noise development when a target position lies between two increments and the motor continually jumps between the two. Without power, the motor produces no mechanical resistance and may be manipulated by outside forces. The effects of having a great weight pull at the associated axis should be examined prior to installation at the CPS. The third button “Reset Node” resets the drive and may be used when a fault is detected. However, resetting the drive restores it to default parameter values and re-initialization and a homing procedure is required before operation is resumed. Therefore the VI is stopped automatically after the reset and needs to be restarted.

²This value is the same because both motors use the same encoder resolution by default. The resolution may be changed should the need arise.

Many of these directly accessible functions and also the ones that run in the background are organized in SubVIs and accessed by the main VI as needed. This way the program becomes more clearly arranged. Details on programming using the CANopen protocol are available in appendix A.2.

6. Characterization of the laser ablation

An absolutely important criterium for the success of calibrating the retarding potential of the main spectrometer via the CKrS is the cleanliness of the HOPG substrate. Condensed residual gas on the substrate means a change in the work function for the ^{83m}Kr conversion electrons and with it a shift in the energy line position [Ost08]. The CKrS employs two means for cleaning the substrate: a resistive heater that heats the complete substrate from the back side and an ablation laser which heats the surface of the substrate where the gas is condensed on. With the ablation laser it is possible to achieve high temperatures on the substrate surface.

This chapter deals with the application of laser ablation by scanning the complete substrate. For this purpose, the LabVIEW program which was developed in [Mur11] was enhanced to allow automated scanning. Several characteristics of the ablation laser, including the beam profile, different types of power adjustment and the effects of high-intensity ablation on the HOPG substrate, have been examined. A quadrupole mass spectrometer was used to determine the gas composition inside the vacuum chamber during the ablation.

6.1. The setup for ablation

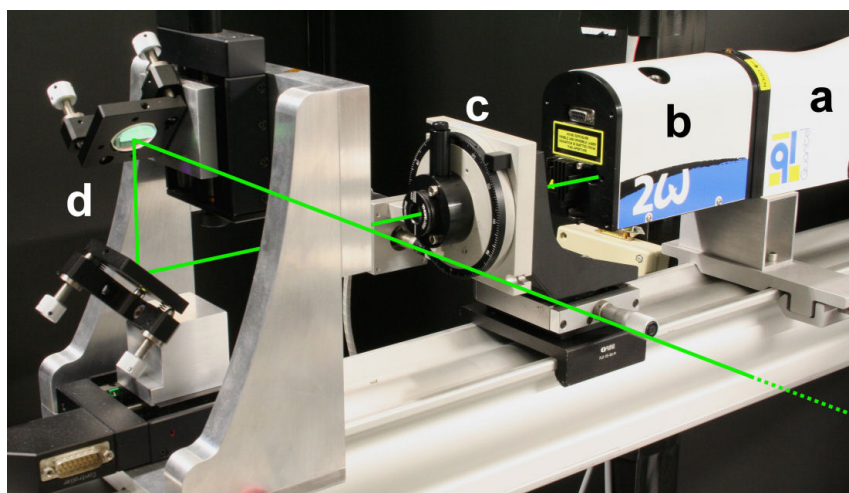


Figure 6.1.: **The laser ablation setup** consists of a pulsed Nd:YAG laser (a), a second harmonics generator module (b), a Glan laser polarizer for power adjustment (c) and movable mirrors to guide the laser beam (d).

The laser ablation setup (figure 6.1) consists of four main components:

6.1.1. The ablation laser

The ablation laser (company: Quantel, type: Brilliant) is a Q-switched (pulsed) Nd:YAG (Neodymium-doped Yttrium Aluminium Garnet) solid state laser with an output energy of 360 mJ/pulse at an output wavelength of 1064 nm, a pulse rate of 10 Hz and a pulse length of ≈ 5 ns. [Qua08]. The active medium is excited by optical pumping through a flash lamp which produces heat that needs to be dissipated. Therefore, the optical head (figure 6.2) is connected to a water cooling unit by an umbilical.



Figure 6.2.: **The ablation laser** consists of an optical head (a), a second harmonics generator module (b) and a power supply and cooling group cabinet (not shown) to which the optical head is connected by an umbilical.

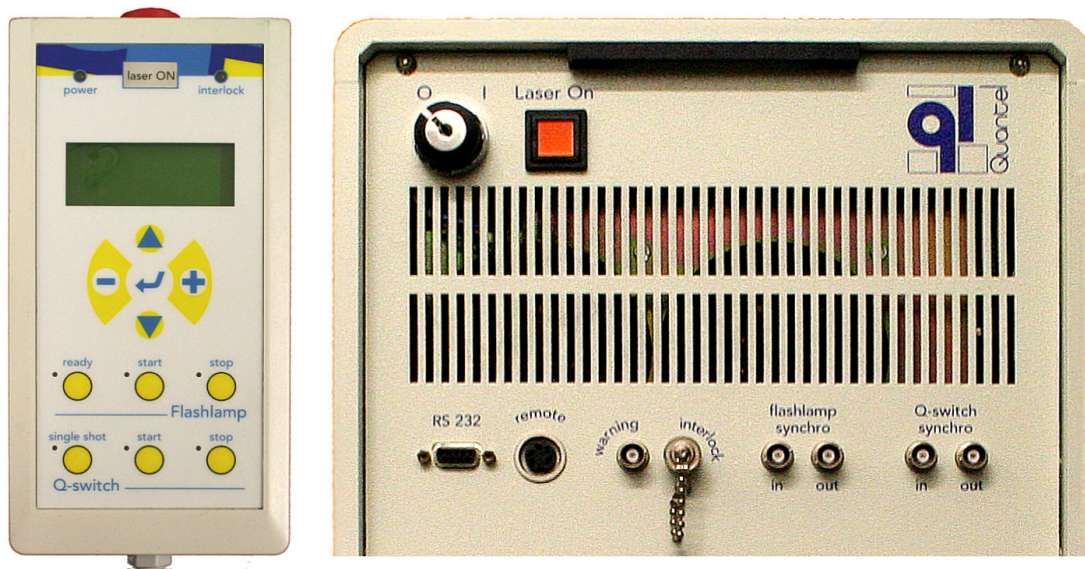


Figure 6.3.: **The remote control box** (left) allows manual control of the laser. It is connected to the “remote” connector on the power supply and cooling group cabinet (right). The “RS-232” connector allows computer control.

There are two ways to control the laser:

1. A remote control box (left picture in figure 6.3) allows manual input for any parameter or mode and length of the laser operation.
2. The RS-232 interface on the power supply and cooling group cabinet (right picture in figure 6.3) allows computer control of the laser via a LabVIEW program.

Q-switching

The laser is Q-switched which means the quality factor Q of the laser cavity is modulated. A high Q factor corresponds to low resonator losses and vice versa. During pulse-pumping by the flash lamp, the Q-switch is set to prevent the light from travelling back and forth in the cavity so laser operation cannot occur when the population inversion reaches the threshold population. When the Q factor is set to a high value, the laser will exhibit a gain that is far greater than the losses and the stored energy will be released in form of a short and intense light pulse.

If the pump pulse is applied to the active medium starting at time $t = 0$, the population inversion for a 4-level laser (figure 6.4) is [Sve10]

$$N(t) = N_{\infty}[1 - \exp(-t/\tau)] \quad (6.1)$$

where the maximal population inversion is given by

$$N_{\infty} = R_p \tau. \quad (6.2)$$

Here R_p is the pump rate which is assumed to be constant during the length of pumping pulse and τ is the lifetime of the excited state that produces the laser light when decaying. For a Nd:YAG laser τ is $230 \mu\text{s}$ [Sve10]. Figure 6.5(a) shows the time behavior of $N(t)$ during pumping at a low Q factor. The pump pulse duration should not be considerably longer than τ because much of the pump power after this point would be wasted through spontaneous decay instead of increasing the inversion energy significantly. The internal fire order of the flash

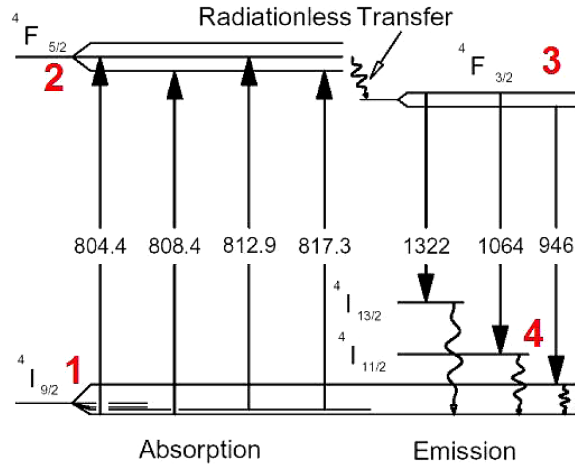


Figure 6.4.: **Energy levels for the Nd:YAG laser.** The transitions $2 \rightarrow 3$ and $4 \rightarrow 1$ are radiationless. The transition $3 \rightarrow 4$ produces the characteristic 1064 nm and other wavelengths. Figure [Den10].

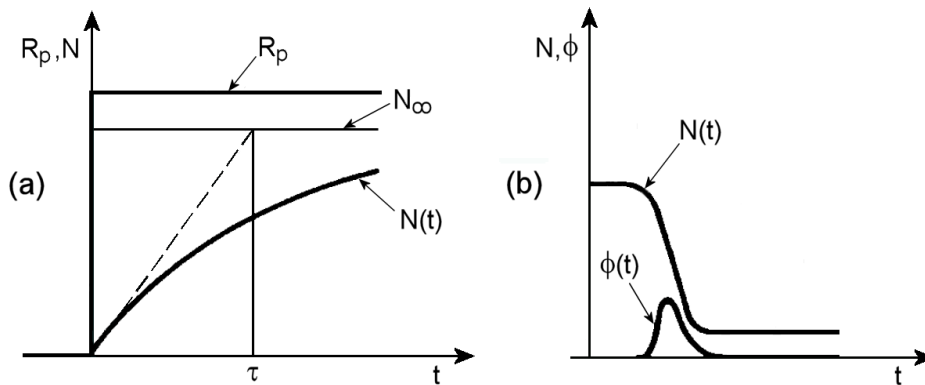


Figure 6.5.: **Sequence of events in a Q-switched laser:** (a) Idealized time behavior of the pump rate R_p and of the population inversion $N(t)$ before Q-switching. (b) Time behavior of population inversion $N(t)$ and photon number $\phi(t)$ after Q-switching. Figure adapted from [Sve10].

lamp in the Brilliant laser has a duration of 50 μs [Qua10].

Figure 6.5(b) shows the behavior of $N(t)$ and the number of photons in the cavity $\phi(t)$ after the Q-factor has been increased. The stimulated emission of photons becomes dominant and reduces the population inversion very quickly. The rising of $\phi(t)$ corresponds to the decrease of $N(t)$. At the point where more photons leave the cavity than are created, $\phi(t)$ starts to drop until it reaches zero. The amount of population inversion left after laser operation, depends on the dynamics of the Q-switching process [Sve10].

The ablation laser is Q-switched by an active electro-optical shutter. Active in this context means that a voltage is applied to the shutter which determines its transparency for the laser light. The shutter comprises a Pockels cell which consists of a nonlinear crystal with refractive indices depending on the applied DC voltage. The induced birefringence is proportional to this voltage. This is called the Pockels effect. The phase difference between an electromagnetic wave polarized perpendicular (ordinary axis) and one polarized parallel to the optical axis (extraordinary axis) of the crystal is [Sve10]

$$\Delta\varphi = k\Delta nL \quad (6.3)$$

where the wave number $k = 2\pi/\lambda$, the value of the induced birefringence $\Delta n = n_o - n_e$, and L is the crystal length.

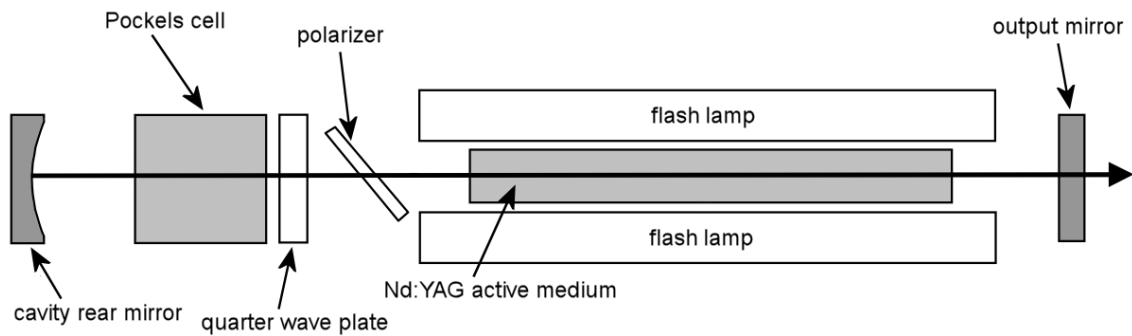


Figure 6.6.: **Schematic layout of the ablation laser.** The components of the Q-switch are the polarizer, the quarter wave ($\lambda/4$) plate and the Pockels cell. Figure adapted from [Qua10].

Figure 6.6 shows a schematic layout of the Nd:YAG laser. The transmission axis of the polarizer is parallel to the polarization of the laser light emitted from the active medium. The optical axis of the $\lambda/4$ plate lies at an angle of 45° to this polarization. This means that $\Delta\varphi_{\lambda/4} = \pi/2$ between the ordinary and the extraordinary ray. After passing the $\lambda/4$ plate, the light is therefore polarized circularly. If no voltage is applied to the Pockels cell, $\Delta\varphi_{Pockels} = 0$ and the circular polarization remains intact when the light passes through. After reflection at the cavity rear mirror the polarization of the light is again changed by the $\lambda/4$ plate and again $\Delta\varphi_{\lambda/4} = \pi/2$. The light is now linearly polarized but because of the total phase change, $\Delta\varphi_{total} = \pi$, the resulting polarization is perpendicular to the transmitting axis of the polarizer and thus the light is blocked (see figure 6.7).

If now the correct voltage is applied, the Pockels cell creates another $\lambda/4$ plate, so that $\Delta\varphi_{Pockels} = \pi/2$. This results in $\Delta\varphi_{total} = 2\pi$ and the polarization of the light is again

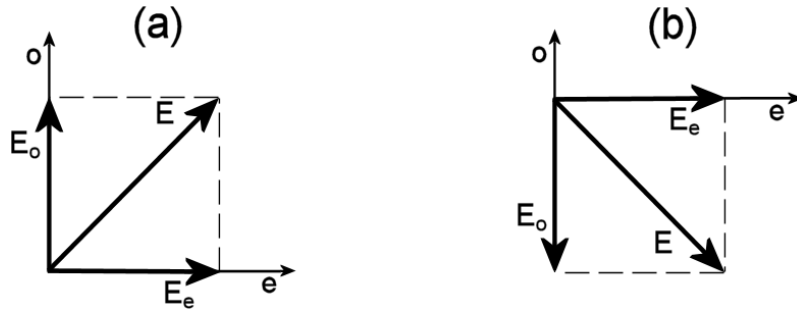


Figure 6.7.: **The polarization state before (a) and after (b) passing the $\lambda/4$ plate twice.** The phase difference between E_o and E_e is π while the polarization state has been rotated by $\pi/2$. The orientation of E in (a) is the same as the polarizer transmission axis.

parallel to the polarizer transmission axis. Now the Q factor is high and laser operation is possible.

There is a delay between flash lamp firing and Q-switching, because of the lamp's response time ($175 \mu\text{s}$ until the electrical pulse is at its maximum after flash lamp firing starts) and the time the Neodymium requires to reach maximum fluorescence ($285 \mu\text{s}$ after flash lamp firing starts) [Qua08]. Section 6.2.1 will show that the adjustment of the delay allows an approximate laser power adjustment.

6.1.2. The second harmonic generator

The optical head is equipped with a second harmonic generator (SHG) module which doubles the output wavelength to 532 nm and reduces the output energy to 180 mJ/pulse at the same time.

Second harmonic generation happens when coherent light of sufficient intensity travels through a nonlinear medium. The passing electromagnetic wave causes the electrons in the material to oscillate and emit electromagnetic waves themselves. At small field strength the oscillation is small and Hooke's law applies. The polarization in the x -direction¹ in this case is [Dem06]

$$P_x = \varepsilon_0 \chi^{(1)} E_{0x} \cos \omega t \quad (6.4)$$

where $\chi^{(1)}$ is the electromagnetic susceptibility of first order. At rising light intensity the electrons are further moved from their nuclei and start being influenced by the nuclear charges of neighbouring atoms. When calculating the polarization, these effects of second order have to be considered [Dem06].

$$P_x = \varepsilon_0 (\chi^{(1)} E_{0x} \cos \omega t + \chi^{(2)} E_{0x}^2 \cos^2 \omega t) \quad (6.5)$$

As it holds $\cos^2 x = 1/2(1 + \cos 2x)$ this results in

$$P_x = \varepsilon_0 (1/2 \chi^{(2)} E_{0x}^2 + \chi^{(1)} E_{0x} \cos \omega t + \chi^{(2)} E_{0x}^2 \cos 2\omega t). \quad (6.6)$$

¹For P_y and P_z analogous equations apply.

The polarization P_x comprises a constant term, one term which is a function of ω and another one describing the part of the electromagnetic field oscillating with 2ω . Equation 6.6 explains that each atom or molecule of the medium which is hit by the incident wave ω emits a scatter wave ω (Rayleigh scattering) and a harmonic wave at 2ω .

In isotropic media the phase velocities of the incident wave and the harmonic wave are generally different, $v_{Ph}(2\omega) = c/n(2\omega) \neq c/n(\omega) = v_{Ph}(\omega)$. After a distance of

$$\Delta z = \frac{\lambda/2}{n(2\omega) - n(\omega)} \quad (6.7)$$

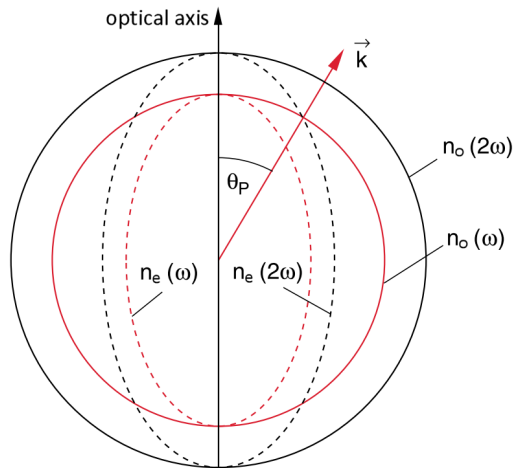


Figure 6.8.: **On phase matching** of the incident wave ω and the harmonic wave 2ω in birefringent crystals. Figure [Dem06].

the harmonic wave that propagates in the same direction (optical second harmonic generation). However, the angle θ_p corresponds only to a certain wavelength and is different for others [Dem06]. Depending on the electric field strength in a laser, the conversion efficiency can reach nearly 100% [Sve10].

This SHG module comprises a highly deuterated KD*P (KD_2PO_4) crystal. When the phases are not matched properly, the crystal can be rotated by turning the adjustment screw on top of the module. A set of dichroic mirrors isolates the required wavelength and guides the beam towards the output port.

6.1.3. The Glan-Laser polarizer

The Glan-Laser calcite polarizer (GLP, company: Thorlabs, type: GL10-A) in front of the laser is used for adjusting the laser power which reaches the substrate. Its underlying principle is that of a Glan-Thompson polarizer.

The Glan-Thompson polarizer comprises an optically negative, uniaxial crystal (calcite) which is cut in half as shown in figure 6.9. The cut surfaces are then joined together by a transparent glue. When unpolarized light enters the polarizer through one of its

travelled inside the medium after generation, the harmonic wave would be phase-shifted by π compared to the incident wave and would prevent the 2ω oscillation of the dipoles. No “macroscopic” wave can form from the singular 2ω waves and conversion to the harmonic wave is nearly zero.

The solution to this problem lies in the birefringence of anisotropic materials. When the incident wave is polarized at a certain angle θ_p (phase matching angle) to the optical axis of an optically negative ($\Delta n = n_e - n_o < 0$) uniaxial crystal, the index of refraction $n_e(2\omega)$ is the same as $n_o(\omega)$. The phase velocity is thus the same for both waves and the singular 2ω waves add in-phase to one another. This way a part of the incident wave is transformed to

entry surfaces, to which the optical axis is parallel, it is split into an ordinary (o) and an extraordinary (e) beam. If the light enters the crystal perpendicularly to the entry surface, the two beams propagate in parallel but at different speeds, c/n_o and c/n_e until they reach the cut surface. The glue (i.e. Canada balsam) has a refractive index n_g which is smaller than n_o but greater than n_e . If the angle at which the beam hits the cut surface is greater than the angle of total reflection β_t for the ordinary beam ($\sin \beta_t = n_g/n_o$), the ordinary beam is totally reflected. Then the transmitted light comprises only the extraordinary beam which is completely linearly polarized [Dem06].

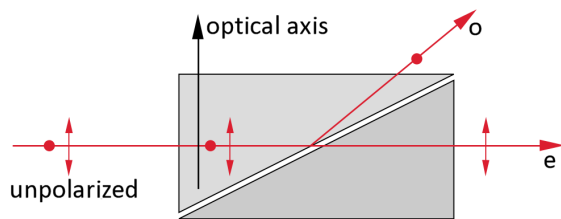


Figure 6.9.: **Glan-Thompson polarizer** [Dem06].

The polarized laser light can be described as an ordinary beam and an extraordinary beam (comparable to the splitting of E into E_o and E_e in figure 6.7 (a)) whose intensities depend on the orientation of the polarization to the optical axis. The polarizer is mounted to a rotary table to allow the adjustment of the orientation and thus the adjustment of the laser power. The ordinary beam is absorbed in a beam dump

which is basically an anodized screw inside an anodized tube (figure 6.10). The anodization ensures maximum absorption. The end of the screw is pointed rather than flat to prevent reflection back into the GLP. The power of the extraordinary beam was measured in the course of this work and the results will be presented in section 6.2.3.

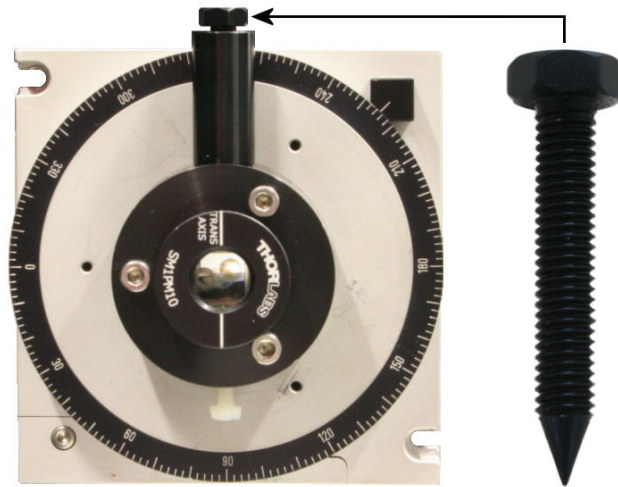


Figure 6.10.: **The Glan-Laser polarizer** in its rotary mount. The screw serves as a beam dump and is located at the side where the ordinary beam leaves the GLP.

6.1.4. The dichroic guiding mirrors

The last component in the laser ablation setup are the dichroic guiding mirrors. Metal mirrors (gold, silver, aluminum) have a reflectivity of usually 90% in the visible spectral range. This means that a non-negligible portion of the light is absorbed by the metal.

In laser applications usually a much higher reflectivity is required. Dichroic mirrors are multi layer systems with very low absorption. Neighbouring layers have different refractive indices [Dem06]. The incident beam is partially reflected and partially transmitted at the first layer. The same happens with the transmitted beam at the second layer and so on. This is the principle of multiple beam interference which was introduced in section 4.2. For maximum reflectivity the reflected beams need to be phase matched.

Consider a two-layer mirror (figure 6.11) with incident light of wavelength λ and an angle of incidence $\alpha = 0$. The polarization of the light shifts by π if reflected at a medium with higher optical density and remains the same if reflected at a medium with lower optical density. If $n_{air} < n_1 > n_2 > n_3$, there is only a phase shift upon reflection at the first layer

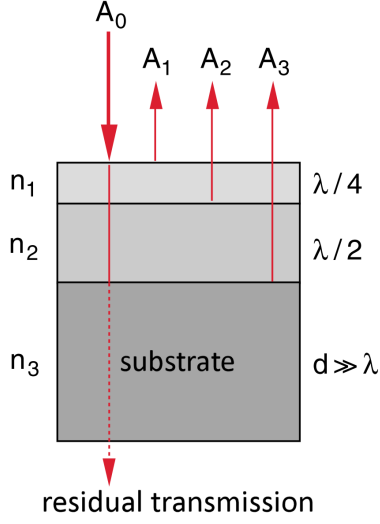


Figure 6.11.: **Interference of the reflected amplitudes** in a two-layer dichroic mirror with $n_1 > n_2 > n_3$ [Dem06].

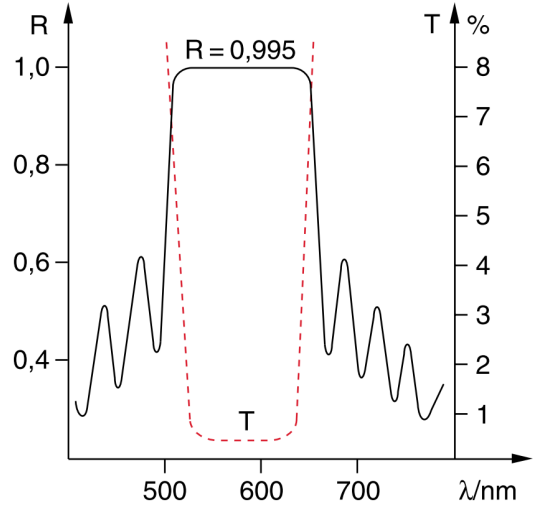


Figure 6.12.: **Reflectivity $R(\lambda)$** of a 12-layer dichroic mirror [Dem06].

(n_1) and constructive interference can occur when the first layer has a thickness of $\lambda/4$ and the second layer has a thickness of $\lambda/2$. The reflectivity of the three different reflecting surfaces are [Dem06]

$$R_1 = \left(\frac{n_1 - 1}{n_1 + 1} \right)^2, \quad R_2 = \left(\frac{n_2 - n_1}{n_2 + n_1} \right)^2 \quad \text{and} \quad R_3 = \left(\frac{n_3 - n_2}{n_3 + n_2} \right)^2. \quad (6.8)$$

The total intensity then is [Dem06]

$$I_R = \left| \sum_{p=1}^3 A_p \right|^2 = A_0 \left[\sqrt{R_1} + \sqrt{R_2}(1 - \sqrt{R_1}) + \sqrt{R_3}(1 - \sqrt{R_1})(1 - R_2) \right]^2. \quad (6.9)$$

Mirrors produced according to this principle can possess a reflectivity of 99.995%. However, their function is limited to a certain spectral range (figure 6.12). The same holds for the angle of incidence. Dichroic mirrors can also be made to retain or change the polarization of light if required.

The laser ablation setup holds two such mirrors but the specifications of the mirrors are unknown. However, comparison of measured data with [Ost08] shows that a sufficient amount of laser light reaches the substrate and the mirrors are not damaged during high-intensity laser irradiation.

Anti-reflective (AR) coating, i.e. on the vacuum window through which the laser beam enters the vacuum chamber, also uses the principle of multi layer surface coating. However, the layers are configured in a way that interference from the reflected beams is destructive.

6.2. Measurements and analyses

This section deals with measurements performed to determine the functionality of the laser ablation setup. These include the effects of different types of power adjustment (specifically, variation of the delay between flash lamp and Q-switch, the flash lamp voltage and the orientation of the GLP) and the scanning of the beam profile.

6.2.1. Adjustment of the laser output power

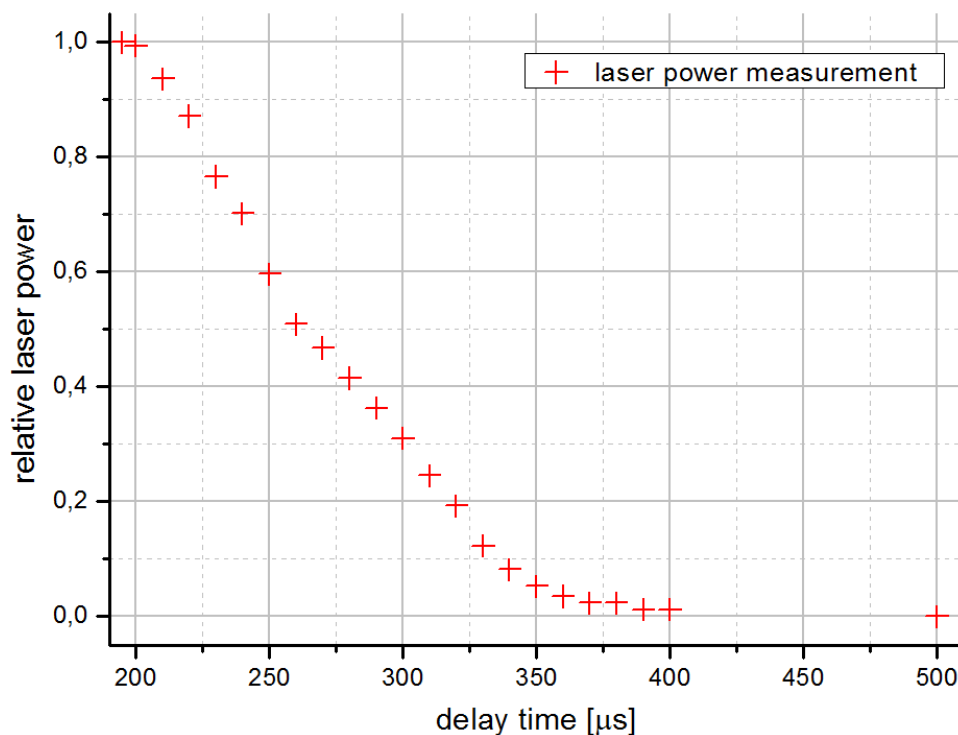


Figure 6.13.: **Dependence of the laser output power on the delay between flash lamp firing and Q-switching.** The raw data to this measurement can be found in appendix B.1, table B.1.

There are two laser parameters which can be varied in order to change the laser output power. The first is the delay between the flash lamp firing and the Q-switching order (FLQ-delay).

The measurements displayed in this section were taken using a power/energy meter (company: Coherent, type: FieldMaxII-TO) and a thermopile sensor² (company: Coherent, type: PM3). With this configuration, the relative laser output power was measured. During the variation of the FLQ-delay, the flash lamp voltage was set to the maximum of 1380 V and the laser power reaching the sensor was reduced by the GLP which was set to 307° ($\approx 1\%$ of the maximum power (see appendix B.3, table B.5)). Figure 6.13 shows the laser output power in relation to the delay. The development of the power output has a maximum at the lowest delay time of 195 μs . Between 200 and 330 μs the drop in laser power is approximately linear. A higher delay results in more disexcitation through spontaneous emission before the Q-switch opens and therefore a lower energy output. At a delay of approximately 400 μs the population inversion has already dropped below the laser threshold and no beam is generated when the Q-switch is opened. The maximum delay time is 500 μs .

Varying FLQ-delay can be a good measure to roughly adjust the laser power reaching the substrate. However, the fine adjustment should still be done with the GLP. Reducing the laser output power via the delay can also help reducing or preventing further damage to the GLP.

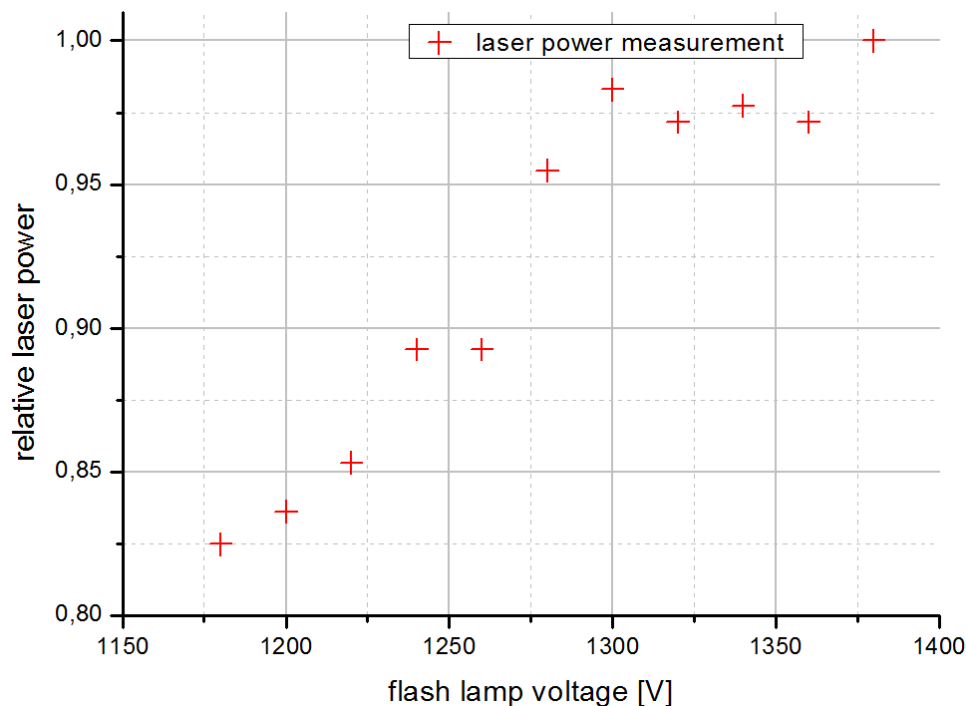


Figure 6.14.: **Laser power in relation to the flash lamp voltage.** The raw data to this measurement can be found in appendix B.1, table B.2.

²The thermopile sensor coating had been damaged in earlier experiments and was not suitable to measure the absolute laser power. However, the relative power distribution could be obtained by normalizing the measured values.

The second parameter regulating the laser power output is the voltage applied to the flash lamp. A higher luminosity from the lamp results in more atoms in the active medium being excited in one flash. During the measurements the delay was set to $195 \mu\text{s}$ for maximum power output and the laser power reaching the sensor was again reduced by the GLP again set to 307° (1% maximum power). Figure 6.14 shows the laser output power in relation to the applied flash lamp voltage.

The applicable flash lamp voltage ranged from 1180 to 1380 V. This resulted in a variation of the laser power between ≈ 82 and 100% of the maximum power. Due to the limited range and erratic response in changing this parameter, it is recommended to choose and maintain a certain adjustment during measurements.

6.2.2. The beam profile

Before examining the absolute laser power measurement and adjustment, it is important to know the size and power distribution inside the beam spot.

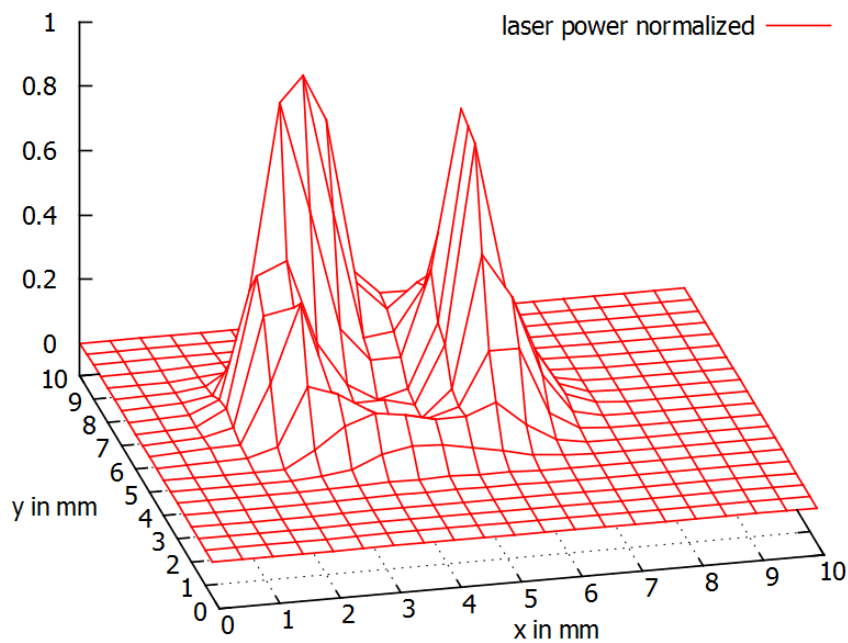


Figure 6.15.: The normalized ablation laser beam profile.

For this reason, the beam spot has been mapped using a 0.5 mm aperture, the movable mirrors and the FieldMaxII-TO laser power/energy meter. The aperture was fixed in front of the PM3 thermopile sensor which was positioned at a distance of ≈ 1 m from the laser output port. The same is the distance between the laser output port and the HOPG substrate. The step size for the movement of the laser spot was 0.5 mm in x - and y -direction.

The $10 \times 10 \text{ mm}^2$ area was initially scanned in steps of 1 mm. Only where the measured values started rising above the background level, measurements at the intermediate 0.5 mm

steps were taken. The FLQ-delay was set to $280 \mu\text{s}$ and the flash lamp voltage to 1280 V. This results in output of 30-35% of the maximum laser power. At each position, 250 measurements were taken during pulsed laser operation at 10 Hz. The raw data from this measurement is displayed in appendix B, table B.3. In the background region an interpolation between the measured values was done. Table B.4 in appendix B shows the normalized values after subtracting the lowest measured background value. Figure 6.15 shows a three dimensional representation of this table.

The beam spot contains two regions of high intensity divided by an area of almost zero power in the center. Figure 6.16 shows a more quantitative image of the power distribution. The contour lines are set in steps of 10% of the maximum beam power. To determine the

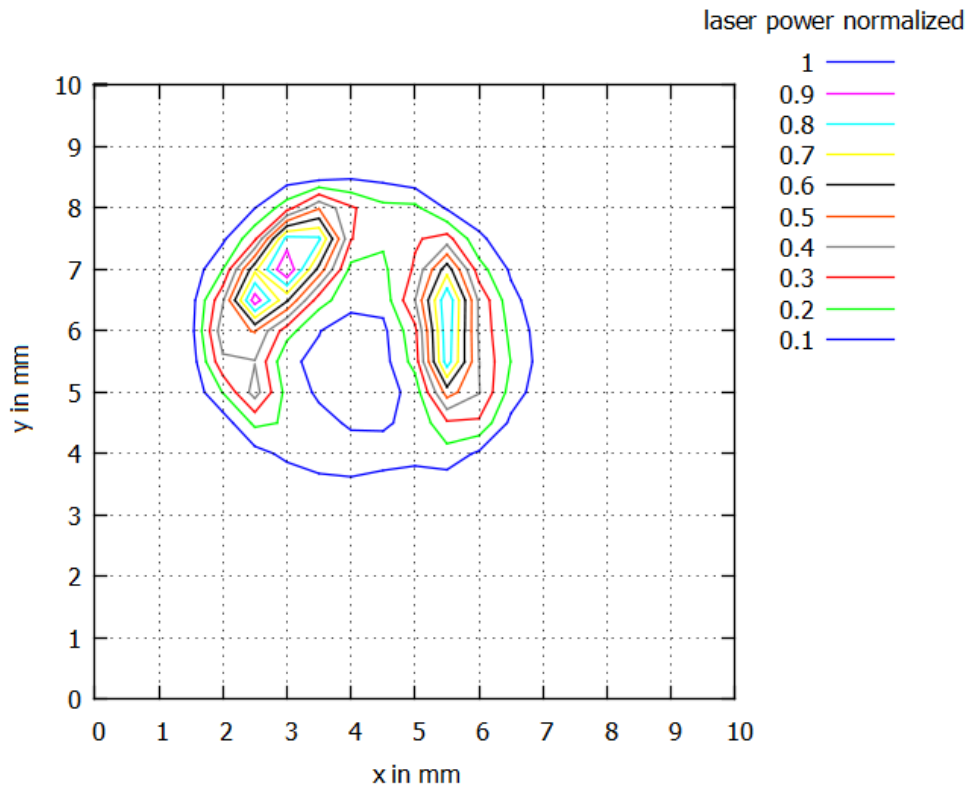


Figure 6.16.: **The power distribution shown as contour lines.** The maximum lies at $P_{max}=(3,7)$. The blue area near the beam spot center is an area of almost zero intensity.

spot size, the area with at least 10% of the maximum intensity was chosen. For simplification, the area of low intensity in the center was also included.

The analysis was done by comparing the number of pixels inside the 10 % contour line (spot) with the number of pixels that made up the rectangle that included and was touched by the spot on all sides (figure 6.17a). The ratio³ between the pixels inside the spot and the $(364\pm 1)\times(326\pm 1)$ pixels of the rectangle is $(200\pm 0.5)/255$. Then the dimensions of the rectangle were compared to those of the image of a $6\times 6 \text{ mm}^2$ reference area with the

³The ratio was derived from one of the color channels (red, blue, green) of the histogram while the spot was white (all color values = 255) and the background was black (all color values = 0). The mean color value of the whole picture for any color channel was 200.

same pixel resolution (figure 6.17b). The reference area contains $(415 \pm 1) \times (406 \pm 1)$ pixels.

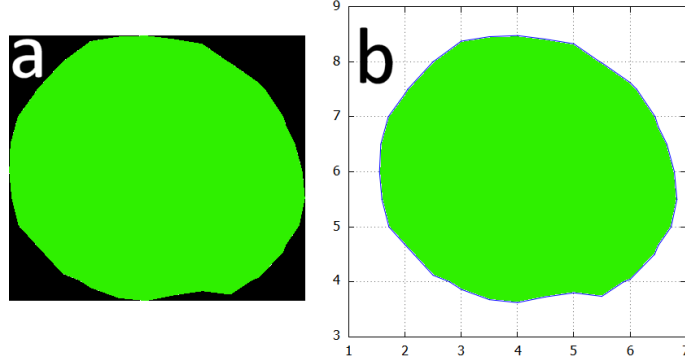


Figure 6.17.: **Analysis of the beam spot size** using the pixel ratio between the spot and the black rectangle (a) and the rectangle and the 6×6 mm² image of the same resolution (b).

The spot size is then determined by

$$A_{spot} = A_{ref. area} \cdot \frac{\text{rectangle pixels}}{\text{ref. area pixels}} \cdot \text{pixel ratio}. \quad (6.10)$$

Numerically this is

$$\begin{aligned} A_{spot} &= 36 \text{ mm}^2 \cdot \frac{(364 \pm 1) \times (326 \pm 1)}{(415 \pm 1) \times (406 \pm 1)} \cdot \frac{(200 \pm 0.5)}{255} \\ &= (19.89 \pm 0.12) \text{ mm}^2 \end{aligned} \quad (6.11)$$

at a distance of about 1 m from the laser. This is in good accordance with the spot size determined in [Mur11] by measuring the spot produced on burn paper.

Instead of the expected Gaussian distribution (TEM₀₀ mode⁴, figure 6.18) for the laser power, the beam profile seems to be a mixture of different laser modes which mainly contains the TEM₁₀ mode (figure 6.19). This indicates a misalignment of the laser resonator mirrors which gives a rise to other modes besides the TEM₀₀ mode. This misalignment may also cause a severe loss in the laser power, since the power of the TEM₀₀ mode seems to be missing almost completely [Kue12]. Possible damage of the SHG module, may be another explanation for this kind of beam profile. This could easily be tested by removing the SHG module and repeating the beam profile measurement or by using burn paper to at least check if the spot reaches the minimum intensity to react with the paper all across its interaction area. Should this not be the case a misalignment of the resonator mirrors would be the likely explanation for the beam profile.

⁴The transversal electromagnetic modes (TEM) have neither electric nor magnetic field components in the direction of propagation. The TEM_{nm} mode has n nodes (areas of zero intensity) in x -direction and m nodes in y -direction.

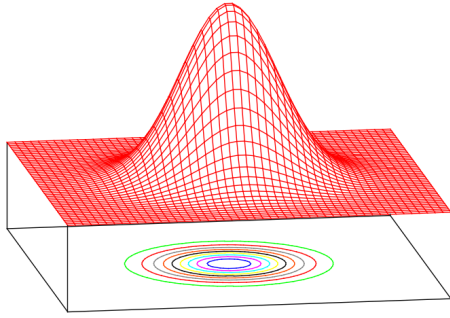


Figure 6.18.: The TEM_{00} mode is a two dimensional Gaussian distribution which should be produced according to [Qua08].

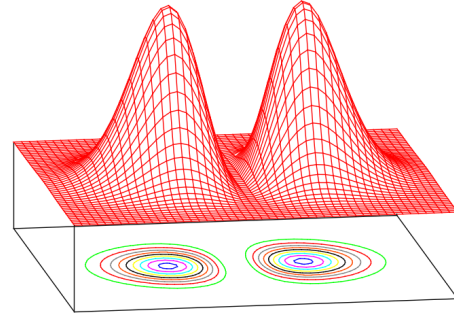


Figure 6.19.: The TEM_{10} mode has two intensity peaks divided by a zero intensity trench.

6.2.3. Adjusting the laser power using the GLP

The absolute laser power was determined by measurement in the low transmission region of the GLP. This time a different power/energy meter (company: Coherent, type: Fieldmaster GS) and a pyro sensor (type: LN-P5) were used. The laser output was set to maximum using the FLQ-delay of $195 \mu\text{s}$ and the flash lamp voltage of 1380 V. The GLP extinction axis lies at roughly 313° , so the area between 302° and 324° was chosen for this measurement to remain well inside the power levels the sensor could handle without being damaged. A rough estimate concerning these power levels was made based on the measurements in [Mur11]. The measurement area was scanned in steps of 1° and 21 measurements of single pulse energies were taken at each position. The resulting values were then fitted with the function

$$y(x) = y_0 + a \cdot \sin^2\left(\pi \cdot \frac{x - xc}{w}\right) \quad (6.12)$$

with the fit parameters y_0 (offset), a (amplitude), xc (phase shift) and w (function period). The plot of the measured values and the fit function is shown in figure 6.20. The values for the fit parameters are:

$$\begin{aligned} y_0 &= (0.02 \pm 0.01) \text{ mJ} \\ a &= (38.38 \pm 0.65) \text{ mJ} \\ xc &= (-47.20 \pm 0.03)^\circ \\ w &= 180^\circ \text{ (fixed value}^5\text{)} \end{aligned}$$

The error bars display the standard deviation calculated from the 21 values measured at each GLP position. The energy amplitude of a single shot suggests that in the 10 Hz mode the laser has a mean spot power of $(383.8 \pm 6.5) \text{ mW}$ or a mean power of $(1930.59 \pm 34.69) \text{ mW/cm}^2$ when the GLP is set for full transmission. This is about 38% of the laser power determined by [Mur11] ($\approx 1000 \text{ mW}$) and less than 22% of the 1800 mW specified by [Qua08].

⁵The function period had to be fixed, otherwise the fit did not yield useful results.

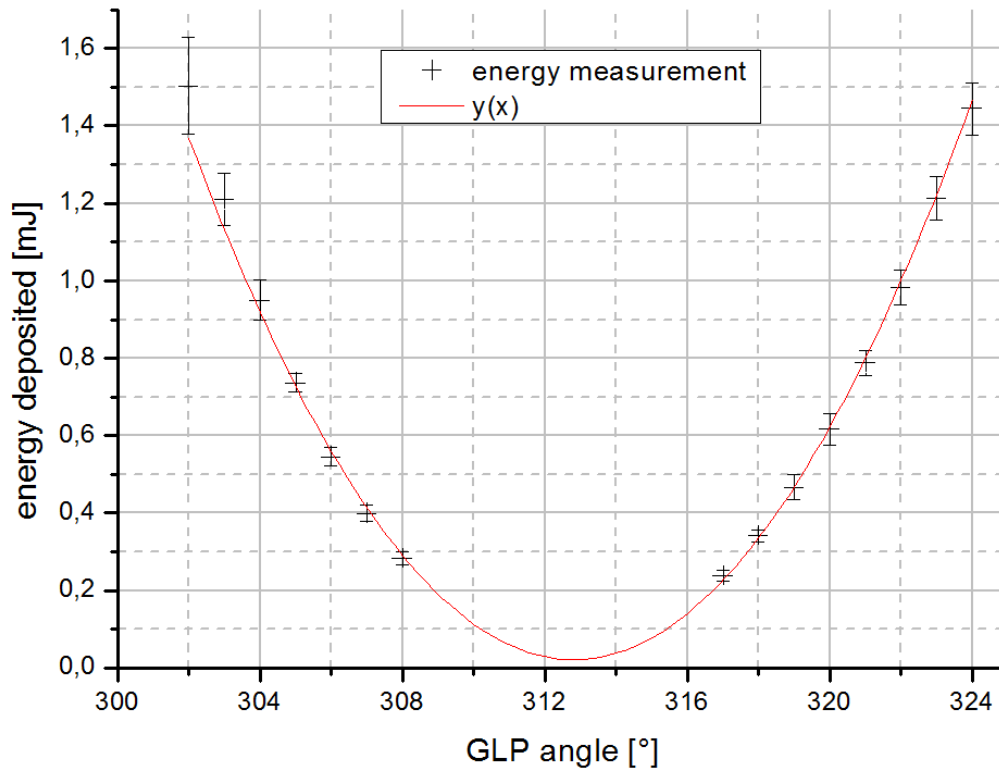


Figure 6.20.: **Plot of the data and the fit function.** The region in between 308° and 317° could not be scanned because the sensor could not measure energies below 0.2 mJ.

At closer inspection, the GLP shows signs of damage (figure 6.21). More specifically the discolorations seem to be the result of damage to the glue which joins the two calcite prisms together when observed from different angles. These discolorations absorb a significant part of the laser power as a second series of measurements has shown.



Figure 6.21.: **The damaged GLP.**

An attempt was made to aim the laser beam through an undamaged part of the GLP. This time 10 measurements at each position were taken. The mean values and the fit function are displayed in figure 6.22. It shows that the energy reaching the energy meter sensor indeed increases. Due to the diameter of the beam and the dimensions of the discolorations in the GLP, it was not possible to determine whether the beam completely passed the GLP through an undamaged part. It is possible that some of the power from the beam edges was still absorbed by the discolored region or the mount of the GLP.

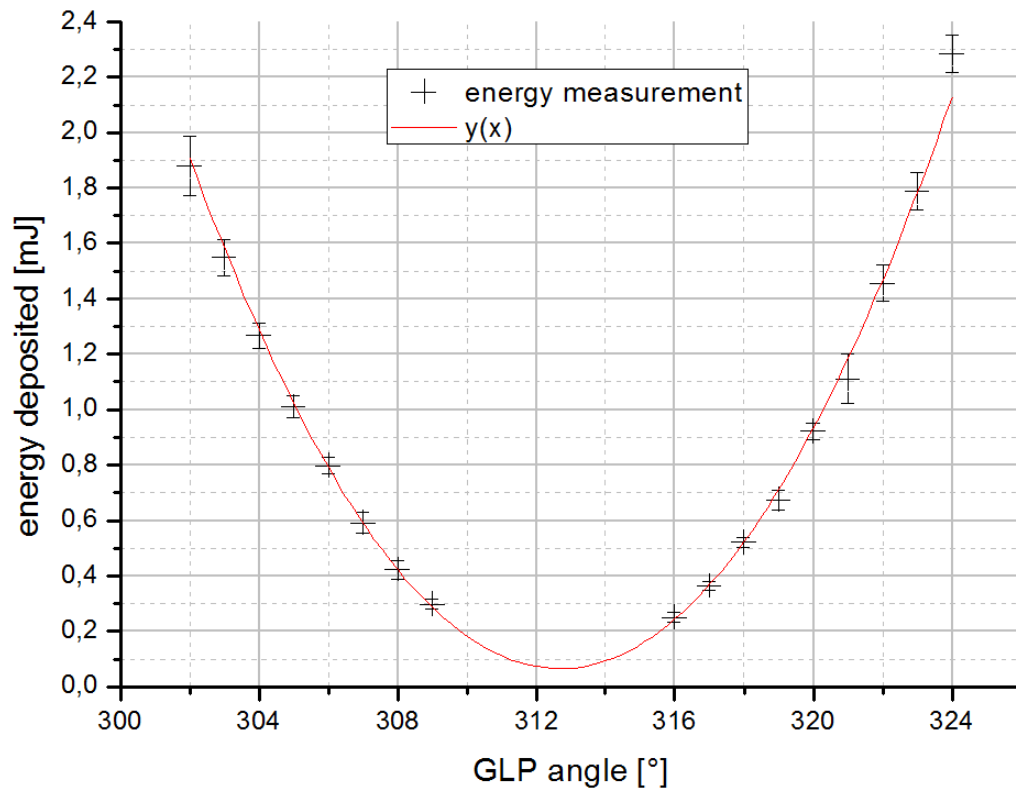


Figure 6.22.: **The measurement through an undamaged part of the GLP** shows slightly more laser energy reaching the sensor.

The values for the fit parameters are:

$$\begin{aligned}
 y_0 &= (0.06 \pm 0.01) \text{ mJ} \\
 a &= (53.61 \pm 0.78) \text{ mJ} \\
 xc &= (-47.31 \pm 0.03)^\circ \\
 w &= 180^\circ \text{ (fixed value)}
 \end{aligned}$$

The maximal beam power in 10 Hz mode rises to (536.1 ± 7.8) mW or (2695.3 ± 42.5) mW/cm². This is about 30% of the intended power of 1800 mW.

This makes the discolorations of the GLP one of the causes for the reduced laser power but certainly not the only one. The beam profile suggests either the absence of the TEM₀₀ mode due to a maladjusted resonator and/or losses inside the SHG module. Losses inside the SHG module can be caused by damage to its light transmitting components or by partial phase mismatching between the incident wave and the harmonic wave. Also, the effects of aging of the Nd:YAG rod may reduce the laser output power. Since no precise reduction factors can be gained from either measurement, it is not possible to exclude other power reducing effects.

The damage of the GLP is unexpected since the damage threshold is 10 J/cm² coming from a pulsed test laser at 532 nm, 10 ns pulse length, 10 Hz repetition rate and a spot

cross section of 0.75mm [Tho12]. Even at full power the ablation laser would have an energy output of only $\approx 0.95 \text{ J/cm}^2$ per pulse. However, the pulse length is only $\approx 4 \text{ ns}$. This leads to a maximum peak laser power of $\approx 237.5 \text{ MW/cm}^2$ while the test laser has a peak power of 1 GW/cm^2 . Considering these values, the damaging of the GLP should not have occurred. No satisfactory explanation for the cause of this damage could be found. Speculations have been made that nonlinear effects may play a role since the pulse duration of the ablation laser is shorter than that of the test laser, but these could not be verified due to a lack of information in this regard.

Since the damage is already done and the GLP absorbs part of the laser energy, it can be assumed that the deterioration of the GLP transmission capabilities will accelerate during its further use. However, even the reduced power today is still sufficient for laser ablation. In earlier ablation laser tests it was determined that a laser power of 200 mW/cm^2 was enough to clean the HOPG substrate [Ost08].

6.3. Scanning the substrate

A scanning routine for the ablation laser has been developed to allow complete cleaning of the substrate. In order for the user to remain outside the hazard area and operate the ablation laser without being dependent on the remote control box, the *TESTAblation.vi* which was developed in [Mur11] was expanded to allow laser control in addition to mirror control. Figure 6.23 and table 6.1 show the absolute position values for the mirrors at each checkpoint in the scanning procedure. The checkpoints A, B, K and L identify

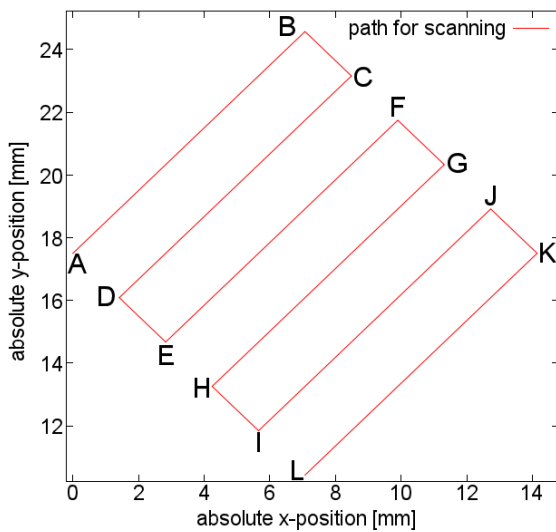


Figure 6.23.: The ablation scanning path.

checkpoint	x [mm]	y [mm]
A	2.500	17.500
B	9.571	24.571
C	10.985	23.157
D	3.914	16.086
E	5.328	14.672
F	12.399	21.743
G	13.814	20.328
H	6.743	13.257
I	8.157	11.843
J	15.228	18.914
K	16.642	17.500
L	9.571	10.429

Table 6.1.: Checkpoint coordinates for the ablation scanning path.

the corners of the $10 \times 10 \text{ mm}^2$ substrate. The programming for the Q-switch operation allows a sequence of inhibited and fired shots to be repeated as long as the scanning progresses. By setting the number of inhibited and fired shots, the mean laser power can be varied.

6.3.1. Changes to the HOPG surface after high-intensity ablation

Initially, the goal was to determine the laser power threshold above which the substrate was free of any krypton or residual gas after applying this ablation process. At this point the (P,C) values (see section 4.3) from ellipsometry measurements would not change no matter how many times the ablation process was repeated.

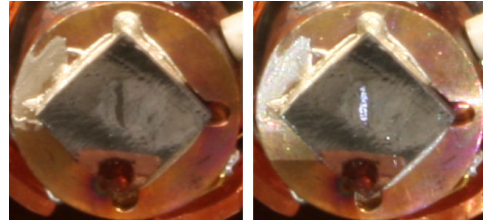


Figure 6.24.: **The damage to the HOPG substrate** was made visible by illuminating the substrate with a lamp from the side.

The examination of photographs of the HOPG substrate taken before the experiments with the ablation laser for this work had started, revealed damage to its surface where the laser had hit during earlier tests (figure 6.24). Furthermore, through a incorrect estimate on the applicable laser power, a much too high setting was chosen in the initial stage of the tests. The laser power used in the following measurements was by a factor of ≈ 2 greater than assumed. This way the laser power used in [Ost08] and [Mur11] was exceeded almost at the beginning of the experiments which most likely changed the surface of the HOPG substrate even more.

The changes to the HOPG surface due to high-intensity laser ablation were observed in a series of ellipsometry measurements after ablation with laser energies ranging from minimal to maximal laser power reached through the variation of the GLP orientation (figure 6.25). In this measurement the compensator was fixed at 45° and only the polarizer was rotated to find the minimum. This type of ellipsometry is called P-ellipsometry⁶. In this measurement, each second 4 shots were fired and 6 were inhibited. This was repeated a maximum of 99 times and the mirror movement speed was adapted accordingly.

The measurement starts out with a krypton layer of $\approx 250 \text{ \AA}$ ⁷. The increase in laser power of up to $\approx 400 \text{ mW/cm}^2$ appears to result in the expected hyperbolical approach to a stable P-value which would indicate cleanliness of the substrate. At higher laser powers the P values become unsteady. Since the substrate is sufficiently cleaned at 300 mW/cm^2 [Ost08], these P-values indicate damage to the HOPG surface⁸.

For the conversion from GLP angle to laser power, the fit parameters in [Mur11] were chosen. The reason is that the discovery of the damage to the GLP happened only several month after the measurement. Since it is unknwn when this damage occurred, it is assumed that the full power was transmitted by the GLP at that time. The power scale considers the factor of $2/5$ from the fact that only 4 of 10 shots are fired and the assumed factor

⁶The P-ellipsometry generally does not find the minimum of zero light intensity. The depth of the minimum varies with the film thickness and at a krypton film thickness of $> 600 \text{ \AA}$ ($\approx +20^\circ$ relative to the P-value of a clean substrate) the minimum becomes too flat to be identified [Spi11].

⁷This is an estimate depending on a the P-value of $\approx 64.5^\circ$ for a clean substrate from measurements in [Mur11] and simulations on the relations between the krypton film thickness and the P-value in [Spi11].

⁸To allow comparison to data from earlier works, the mean laser power is used as an indicator for the ablation power. However, it is the author's opinion that the pulse power or pulse energy would be better suited.

of 2 by which the indicated power in [Mur11] had been reduced. Table B.6 (Appendix B.4) contains the underlying values to the plot in figure 6.25.

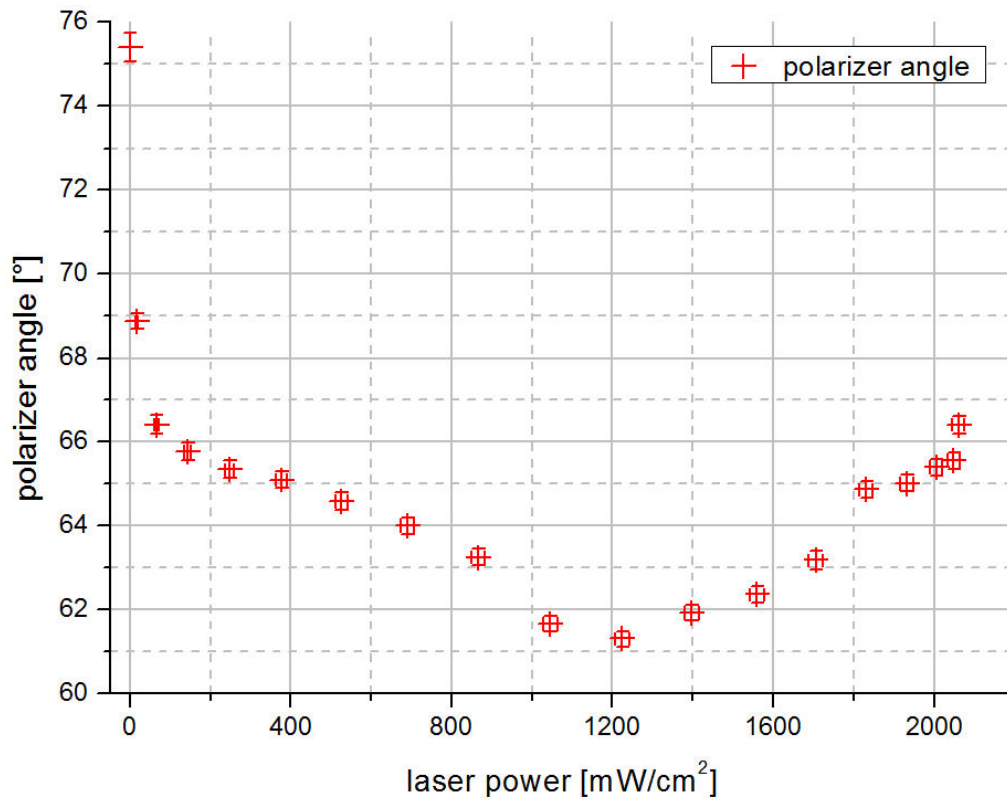


Figure 6.25.: **Increasing the ablation power** results in the decrease of the P-value up to the point where the surface starts to change due to the high temperatures. Increasing the laser power beyond $\approx 400 \text{ mW/cm}^2$ produces an erratic response.

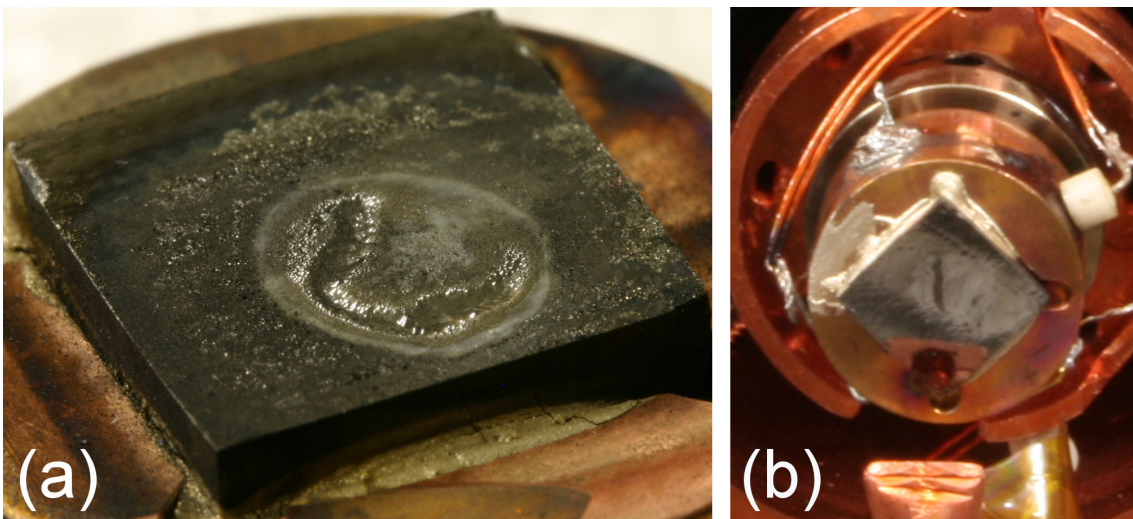


Figure 6.26.: **The damage to the HOPG substrate** extends beyond the beam spot (a). A HOPG substrate prepared for ellipsometry has a smooth and reflecting surface (b).

In an attempt to determine damaging capabilities of the ablation laser and the extent of possible damage to the HOPG substrate, the GLP was removed from the optical path and the ablation laser was set to fire at a single spot of the substrate for 300 seconds at 10 Hz. This resulted in a macroscopic exposure especially in the beam spot regions of high intensity. Figure 6.26(a) shows a closeup view of the substrate after this procedure.

Usually the HOPG, when prepared for ellipsometry measurements, has a smooth and reflective surface like in figure 6.26(b) (except of course for the small scratch in the center). After this procedure there is an imprint of the beam profile on the HOPG surface which is apparent by the two broader and deeper trenches which are connected by a narrower trench of lesser depth (compare to figure 6.15). The coarse and blackened area around the spot has a ring-like shape (halo). At the far edge of the sample, the surface appears smooth but discolored.

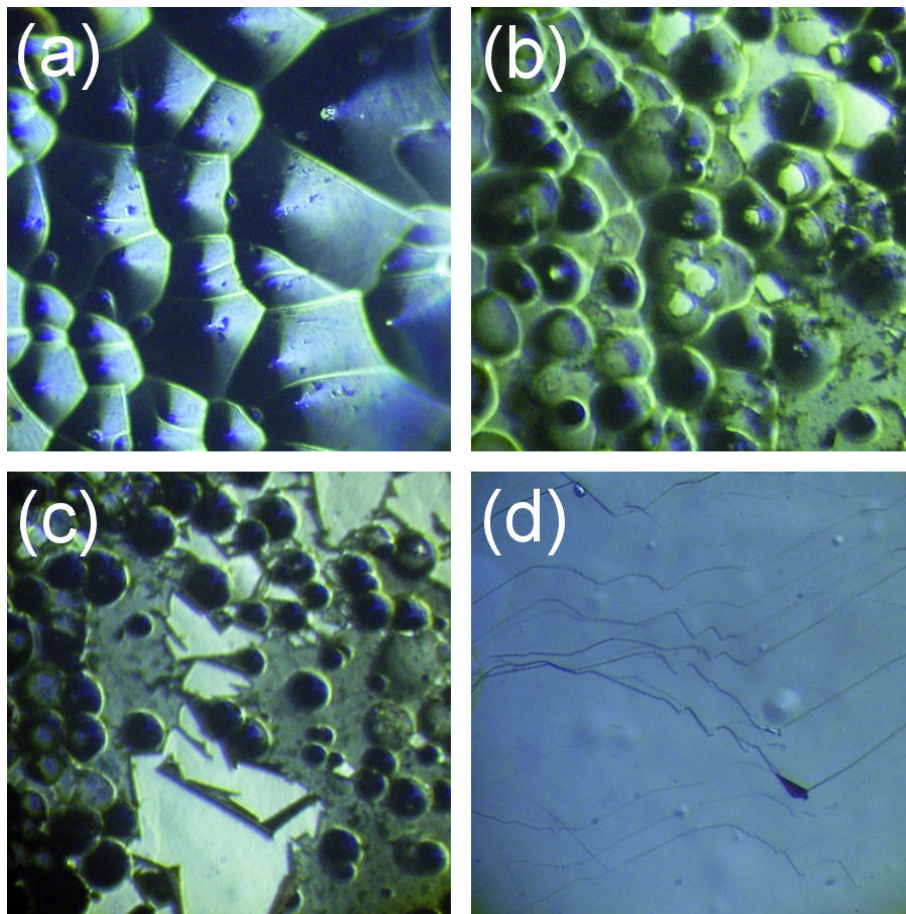


Figure 6.27.: **Microscopical analysis of the HOPG surface** reveals the melting of the surface in the area hit by the laser beam (a), (b) and the peeling of the surface layer in the surrounding coarse areas (c). The surface of an undamaged HOPG sample is clean and smooth between the layer steps (d). Magnification factor of pictures (a)—(c): 16x, (d): 10x.

Images taken through a microscope reveal that the surface appears to have melted into cone like (figure 6.27(a)) or beady structures (figure 6.27(b)) where the laser beam hit

the surface. In the area where the surface is coarse remnants of the original surface can be found which appears to peel at the edges (figure 6.27(c)). Figure 6.27(d) shows an undamaged HOPG surface which is smooth between the layer steps.

Discussion on the ablation of HOPG

Many experiments have been made in the area of pulsed laser ablation on HOPG using lasers with wavelengths ranging from the UV to the IR and pulse widths ranging from less than 100 fs to several tens of ns. The findings and conclusions from some of these experiments are presented in this section to illustrate the mechanisms of the ablation process on the one hand, and to compare the results to those of experiments conducted under similar conditions on the other hand.

The ablation of HOPG can be very clean, precise and reproducible when conducted with a tightly focused (to the wavelength regime) laser beam and an ultra-short pulse width (120 fs) [Shi00]. The high-intensity radiation is absorbed by the electrons in the optical skin depth. The atoms in the skin layer are thus ionized and form a near-solid density plasma. Due to the mass difference between the atoms and the electrons, the energy transfer occurs weakly during the pulse duration. Since with ultra-short pulses the pulse width falls below the lattice heating time only the solid material in the interaction volume is vaporized and ejected with high kinetic energies while the surrounding material is left intact. In ultra-short pulsed laser ablation the depth per pulse is directly proportional to the square of electron temperature implying that the electron temperature governs the ablation process [Mom96].

The energy transfer to the lattice becomes significant when the pulse width is increased to the ns regime. During the pulse duration the heat diffusion involves a much larger volume than the focus volume and the electrons and ions are in thermal equilibrium. Experiments with pulsed laser ablation showed that damage through thermal shocking at the edges of the interaction area increases as the pulse width increases. Furthermore, the scattering of the cracked material by exiting plasma, plastic flow of the graphite and peeling of the surface was observed in a halo around the focus area. This kind of collateral damage becomes pronounced at pulse widths of a few ps [Shi00].

The difference between ablation with shorter and longer pulses suggests that longer pulses create thermal waves leading to a large halo or vapor dust ring around the area of interaction [Shi00]. In experiments with an 193 nm, 14 ns excimer laser, this halo was characterized as a mechanically soft region with nanocrystalline and turbostratic⁹ carbon [Mec99].

The minimal energy fluence that allows ablation is called damage threshold. Using a 120 fs pulsed Ti:Sapphire laser (825 nm) the damage threshold was found to be 0.25 J/cm² for HOPG [Shi00]. This was reduced to 0.13 J/cm² when using a 90 fs, 620 nm wavelength dye laser [Rei92]. These values were much lower than the 0.9 J/cm² achieved with a 248 nm wavelength, 23 ns pulsed laser [Win97], suggesting that the damage threshold decreases when the pulse width is reduced.

⁹Turbostratic carbon still exhibits the parallel atomic layer structure but the layers have no preferred orientation to one another.

Several species of carbon can be generated in the laser ablation of graphite with nanosecond pulses. These are electronically excited neutral carbon atoms as well as singly and doubly charged atomic carbon ions [Tog96], [Mue93]. During the pulsed laser vaporization (308 nm, 16 ns pulse width) of carbon, the formation of carbon clusters C_n^+ (where n lies between 2 and 7) was detected by time-resolved ion mass spectrometry. The most abundant ions were C^+ and C_3^+ which was attributed to recombination processes in the gas phase [Ari98]. 30 ns laser pulses generated primarily C_4^+ and C_3^+ . In contrast, during ablation with 500 fs pulses no evidence for cluster formation could be found [Mue93].

Raman spectroscopy¹⁰ of a pure graphite surface reveals a sp^2 hybridization. Ablation of that surface results in sp^3 hybridized amorphous carbon being created at and around the ablated spot which is more pronounced, the greater the pulse width. After ablation with ns pulses, the presence of diamond-like carbon (DLC, more strictly sp^3 hybridized than amorphous carbon¹¹) in the focus area and the halo around it could be detected [Mec99].

The creation of DLC happens as the pressure and temperature on the irradiated surface are locally raised. In this environment the preferred phase is sp^3 and the sp^2 carbon is transformed to DLC. This process occurs irrespective of the pulse duration. However, for ultra-short pulses the detection rate for DLC on the surface is low since the heating is localized and the species are ejected with very high kinetic energies. The vast majority of the transformed DLC is thus removed in the ablation process [Shi00].

6.4. Quadrupole mass spectrometry

To analyze the composition of the gas inside the vacuum chamber during the ablation a quadrupole mass spectrometer (QMS) has been employed. The QMS distinguishes between ions with different m/q ratios, where m is the ion mass mass in terms of atomic mass units (amu) and q is its charge in terms of unit charges. The vacuum setup of the CKrS uses the residual gas analyzer (RGA) “Transpector2” made by Inficon.

6.4.1. The principle of quadrupole mass spectrometry

This section provides a brief overview over the functionality of a QMS. A QMS comprises three main components, each serving a different function:

1. **The ion source** generates ions from the gas molecules inside the vacuum chamber. To achieve this, a heated cathode produces low energy electrons (usually 50-150 eV) which ionize a small portion of the gas molecules. The energy of these electrons

¹⁰In Raman spectroscopy monochromatic light is scattered at a sample. From the difference between the frequency of the incident light and the frequencies of the scattered light, information on the sample material can be gained.

¹¹The distortion of the bond angles in the tetrahedral structure determines the quality of the sp^3 hybridization [Shi00].

determines how many and what sort of ions are produced (single or multiple charge). The ion current, i^+ , can be calculated from [BAL]

$$i^+ = i^- \cdot l \cdot s \cdot p \quad [\text{A}] \quad (6.13)$$

where

- i^- is the current of ionizing electrons [A],
- l the mean free path [cm]
- s the differential ionization¹² [$1/(\text{cm} \cdot \text{mbar})$]
- p the partial pressure of the analyzed gas [mbar]

Depending on the complexity of the ionized molecule, fragment ions can be produced. As an example, table 6.2 shows the cracking pattern of CO_2 produced with 70 eV electrons.

m/q	intensity	ion
12	2.46	$^{12}\text{C}^+$
16	6.24	$^{16}\text{O}^+$
22	1.78	$^{12}\text{C}^{16}\text{O}_2^{++}$
28	6.55	$^{12}\text{C}^{16}\text{O}^+$
29	0.06	$^{13}\text{C}^{16}\text{O}^+$
44	100.0	$^{12}\text{C}^{16}\text{O}_2^+$
45	1.16	$^{13}\text{C}^{16}\text{O}_2^+$
46	0.41	$^{12}\text{C}^{16}\text{O}^{18}\text{O}^+$

Table 6.2.: **The cracking pattern of CO_2** at 70 eV electron energy. The intensity values are normalized to that of the most commonly produced ion ($^{12}\text{C}^{16}\text{O}_2^+ = 100.0$). Intensities of less than 0.01 are not shown [BAL].

Electric fields guide the ions towards the ion selecting section.

2. **The quadrupole mass filter (QMF)** was developed by W. Paul in 1953. The QMF consists of four ideally hyperbolically shaped¹³ rod electrodes (figure 6.28). The potential in this configuration is [Bla07]

$$\Phi(\vec{r}, t) = \Phi_0(t) \cdot \frac{x^2 - y^2}{r_0}. \quad (6.14)$$

If $\Phi_0(t)$ is a constant voltage U , an ion inside the QMF oscillates harmonically in the x/z -plane while its amplitude in y -direction increases exponentially until it hits the electrode. If the DC voltage is overlayed with an alternating voltage, the QMF becomes periodically focusing and defocusing in each direction. At certain frequencies

¹²The differential ionization states how many ionizations occur inside the distance of 1 cm at a pressure of 1 mbar and a given temperature.

¹³Usually cylindrical electrodes are used. If the ratio of the round rod radius to the radius r_0 of the QMF (see figure 6.28) is made equal to 1.148, the resulting electric field is a reasonably good approximation to the desired hyperbolic shape [Tra07].

this leads to a stable trajectory for an ion with a certain m/q ratio. For an alternating current V with the frequency ω equation 6.14 becomes

$$\Phi(\vec{r}, t) = (U + V \cdot \cos \omega t) \cdot \frac{x^2 - y^2}{r_0}. \quad (6.15)$$

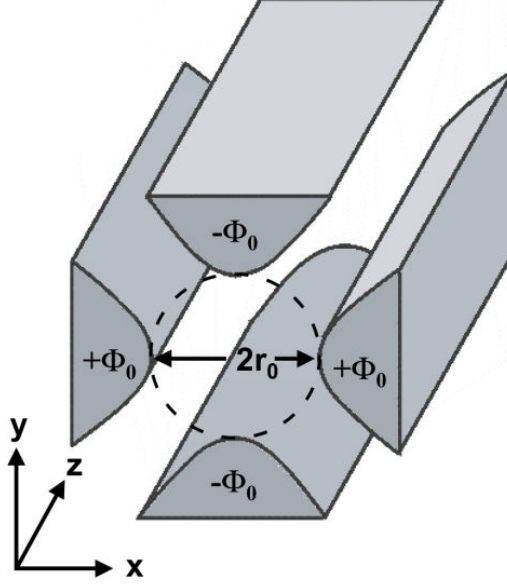


Figure 6.28.: **The rod electrodes of the QMF.** Opposing electrodes have a distance of $2r_0$ to one another and are kept at the same potential. The potential on the other rods has an opposite sign. Figure [Bla07].

For an ion with single positive charge and mass m the equations of motion are [Bla07]

$$\ddot{x} + \frac{2e}{mr_0^2} \cdot (U + V \cdot \cos \omega t) \cdot x = 0, \quad (6.16)$$

$$\ddot{y} - \frac{2e}{mr_0^2} \cdot (U + V \cdot \cos \omega t) \cdot y = 0, \quad (6.17)$$

$$\ddot{z} = 0. \quad (6.18)$$

In a homogenous electric field the time dependent part would be zero when averaged in time. Since the quadrupole field is inhomogenous a small resetting force remains which acts in the direction of reduced field strength (the central axis). This results in periodic movement around the z -axis in x - and y -direction. The movement in z -direction remains steady.

Through the transformation to dimensionless parameters the equations of motion in x - and y -direction become Mathieu's differential equations [Bla07]

$$\frac{d^2 x}{d\xi^2} + (a_x + 2q_x \cdot \cos 2\xi) \cdot x = 0 \quad (6.19)$$

$$\frac{d^2 y}{d\xi^2} - (a_y + 2q_y \cdot \cos 2\xi) \cdot y = 0 \quad (6.20)$$

with

$$a_x = -a_y = \frac{8eU}{mr_0^2\omega^2}, \quad q_x = -q_y = \frac{4eV}{mr_0^2\omega^2}, \quad \omega t = 2\xi. \quad (6.21)$$

Here $a_u/4$ ($u = x, y$) is the ratio between the potential energy eU of the DC field and the kinetic energy $mv^2/2 = mr_0^2\omega^2/2$ of the oscillation amplitude r_0 , and $q_u/2$ is the ratio between E_{pot} in the AC field and E_{kin} .

Solving equations 6.19 and 6.20 for given m and V gives information on the behavior of the ions in the QMF. Since both directions of motion are described by the same differential equation, it is sufficient to consider the normal form of Mathieu's differential equation [Bla07]

$$\frac{d^2u}{d\xi^2} + (a_u - 2q_u \cdot \cos 2\xi) \cdot u = 0 \quad \text{with} \quad u = x, y. \quad (6.22)$$

Figure 6.29 shows the graphical representation of a solution to Mathieu's equation which is simultaneously stable for the x - and y -direction.

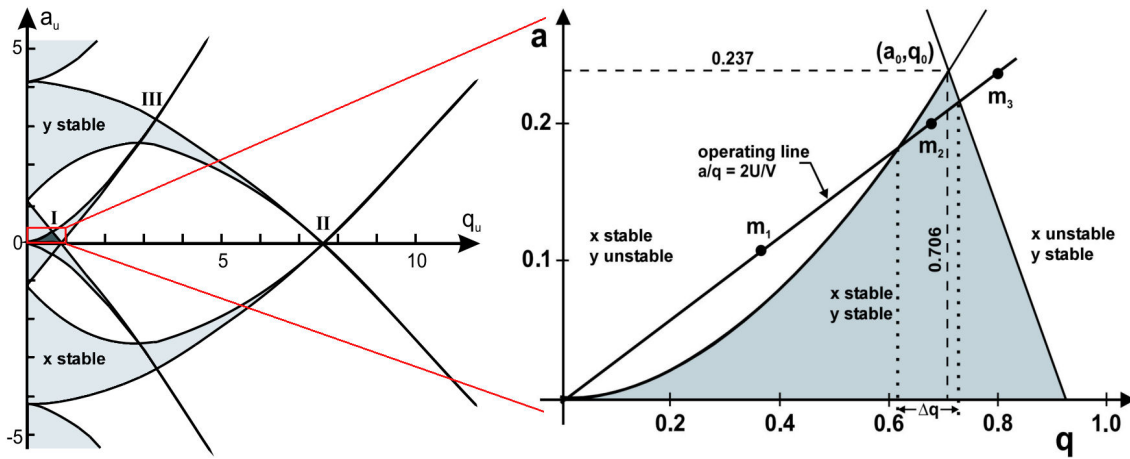


Figure 6.29.: **Stable region of the solution for Mathieu's differential equation.** The shaded areas represent the stable regions for the x - or y -direction. The overlapping area in the magnified picture is an area of stability for both directions. For a given U/V ratio, an operating line through the origin of the coordinate system intersects with this area of stability. The closer this intersection is to the tip $(q_0, a_0) = (0.706, 0.237)$ the smaller becomes the mass range in which the movement is stable. Figure adapted from [Bla07].

An operating line which is defined by the ratio $U/V = \text{const.}$ contains the operation points for all ion masses. Ions that are too light (m_1) are stable in the y/z -plane, but unstable in the x/z -plane. The opposite holds for too heavy ions (m_3). The range for ion masses that lead to a stable oscillation in both directions is adjustable by varying U/V . This range can be calculated from the q or a values of the intersection of the operating line with the boundaries of the area of stability and equation 6.21.

The transformation of equation 6.21 to [Bla07]

$$U = \frac{a_x m^2 r_0^2 \omega^2}{8e} = -\frac{a_y m^2 r_0^2 \omega^2}{8e}, \quad V = \frac{q_x m^2 r_0^2 \omega^2}{4e} = -\frac{q_y m^2 r_0^2 \omega^2}{4e} \quad (6.23)$$

and the resulting stability diagram in figure 6.30 clarify the functionality of the QMF. The areas of stability for m_1 , m_2 and m_3 have the same shape as in a/q -space,

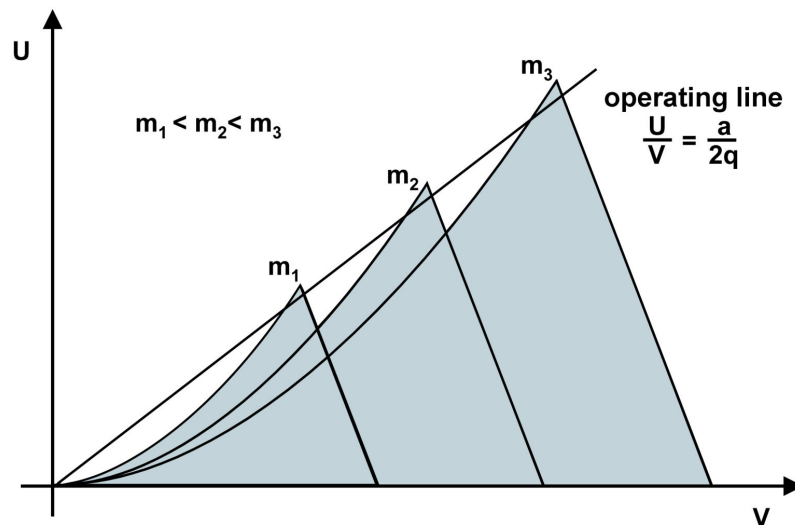


Figure 6.30.: **The stability diagram in (U, V) space** shows the regions of stability for different masses depending on the magnitude of U and V . Figure adapted from [Bla07].

however, their dimensions are stretched by a mass-weighted factor. The simultaneous and proportional increase of U and V (a/q has to remain constant) leads to movement along the operating line and ions with increasing masses can successively be detected. This results in a spectrum with a mass resolution.

3. **The ion detector** can be a Faraday cup in which the ions are collected as a current. This current is transformed to a signal by a sensitive current to voltage transformer. In case of very weak ion currents, a secondary electron multiplier may be used to amplify the signal. For this purpose the ions are accelerated to a few keV before producing secondary electrons at a conversion dynode. These electrons may then be accelerated towards the next dynode where they produce an even greater number of secondary electrons. This may be done several times to achieve a current gain of several orders of magnitude, typically 10^7

6.4.2. Mass spectra taken during the ablation process

The procedure of increasing the ablation power which was discussed in section 6.3.1 has been monitored by the RGA. In this instrument the e^- are produced with the energy of 102 eV [Tra07]. Figure 6.31 shows the development for the ratio $m/q = 12$ amu/e. The amount of the gas adding up to the 12 amu/e signal is displayed as the ion current at the detector. The scale is logarithmic for more clarity.

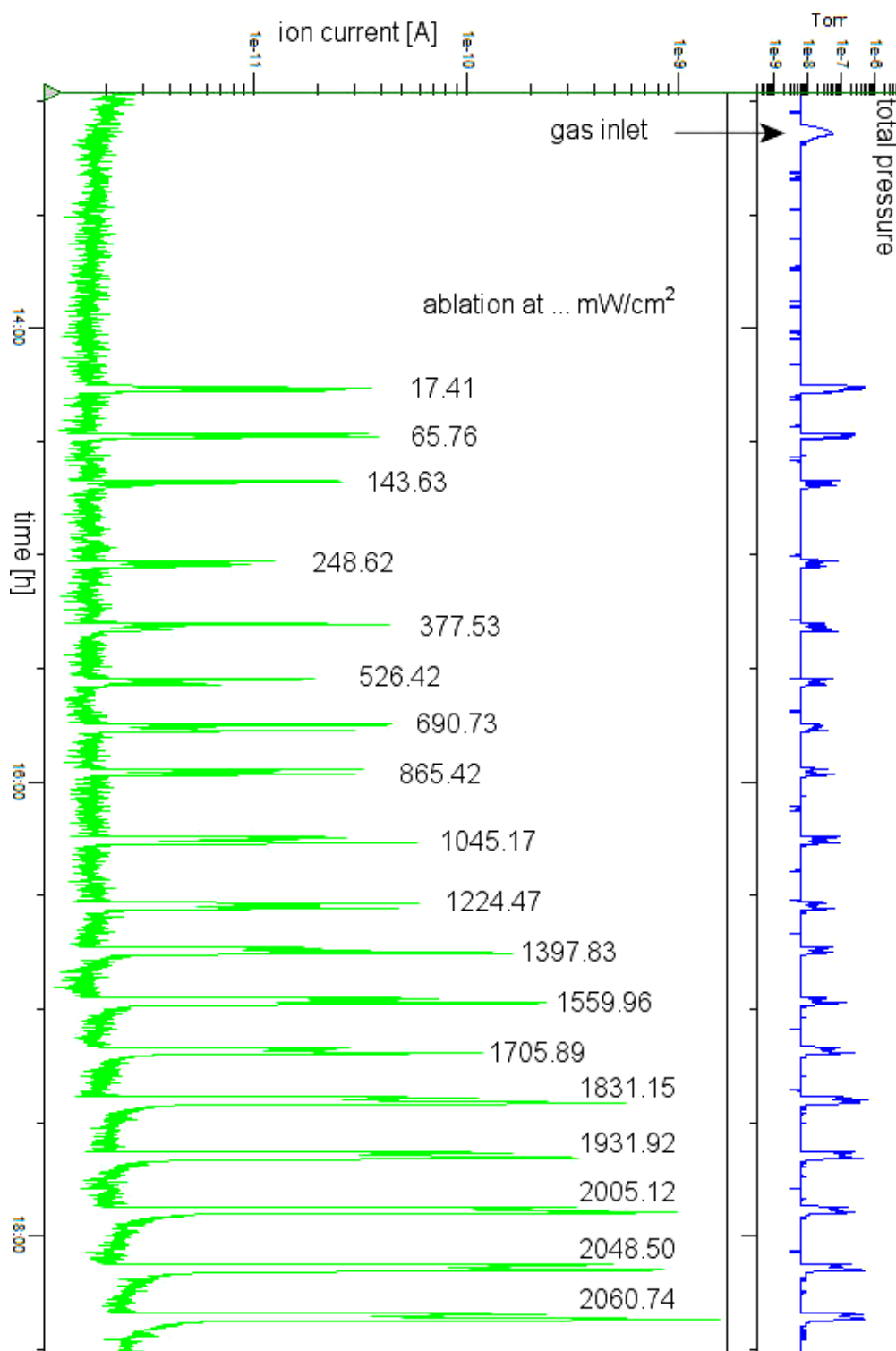


Figure 6.31.: **Analysis of the 12 amu/e bin of the mass spectrometer** (green line) during the ablation with increasing power shows an increase of almost two orders of magnitude between low-intensity and high-intensity ablation. The power values are taken from table B.6. The first ablation with 0.04 mW/cm^2 does not register. The blue graph shows the total pressure inside the vacuum chamber.

During each ablation step a peak occurs, except for the first step where the laser power is minimal (0.04 mW/cm^2). In the total pressure graph an additional peak is visible which stems from the gas inlet.

The 12 amu/e bin shows the current from C^+ ions which can stem from CO , CO_2 or the HOPG. At low intensities the C^+ peak appears to hold at approximately the same level. At about 1000 mW/cm^2 , the ion current during ablation begins to increase until the maximum laser power is applied. The difference between the ion current at low-intensity and high-intensity ablation is nearly two orders of magnitude.

From the development of the total pressure, four points were selected for closer analysis. Figure 6.32 shows the residual gas mass spectrum (a) taken before the first ablation and mass spectra taken during the gas inlet (b), low-intensity ablation (c) and high-intensity ablation (d).

- **(a):** The residual gas mass spectrum shows the presence of hydrogen as a large H_2^+ peak (2 amu/e) and a small H^+ peak (1 amu/e). The H^+ originates mostly from the fragmentation of H_2 and perhaps to a small percentage from water molecules. The presence of water is visible through the 18 amu/e (H_2O^+) and the 17 amu/e (OH^+) peaks. The small 16 amu/e peak indicates the presence of oxygen from air, water or carbon dioxide and monoxide. In addition to CO , CO_2 and air the 28 amu/e peak suggests the presence of molecular nitrogen. The 44 amu/e peak indicates trace amounts of CO_2^+ and/or N_2^+O .

Since this setup contains carbon and hydrogen which can bond in various ways, some types of hydrocarbon fragments (C_nH_m^+) may be present as well.

- **(b):** During the krypton inlet the hydrogen peaks remain nearly unchanged as does the water peak. The peaks at $80, 82, 83, 84$ and 86 amu/e show the different isotopes of krypton. The peak heights appear to correspond to the isotopic composition of krypton¹⁴. Doubly ionized krypton shows at $40, 41, 42$ and 43 amu/e . The 28 amu/e peak indicates triply ionized krypton¹⁵. The appearance of a small 14 amu/e peak which stems from atomic nitrogen suggests that part of the 28 amu/e peak is caused by N_2^+ . At the time of this measurement the krypton gas had been stored in the mixing chamber for several month. As explained in section 3.2.1 the gas could have been contaminated during this time through outgassing from the chamber walls. Since the mixing chamber was evacuated from air atmosphere at some point, there should always be some air adsorbed at the chamber walls which eventually is partly released into the chamber over time. This may be the source of the increased nitrogen during gas inlet.
- **(c):** During the low-intensity ablation the distribution of the krypton peaks remains nearly the same as in (b). However, comparison with the hydrogen peak shows that now much more krypton gas is present in the vacuum chamber. The difference here is that while the krypton was guided towards the HOPG substrate during the gas inlet, it moves in all directions and mostly away from the substrate after being ablated.

¹⁴ ^{80}Kr : 2.29%, ^{82}Kr : 11.59%, ^{83}Kr : 11.50%, ^{84}Kr : 56.99%, ^{86}Kr : 17.28%.

¹⁵The ionization energies for krypton are I: 13.999 eV , II: 24.359 eV and III: 36.95 eV . The values relate to the respective previous ionization step [CRC83].

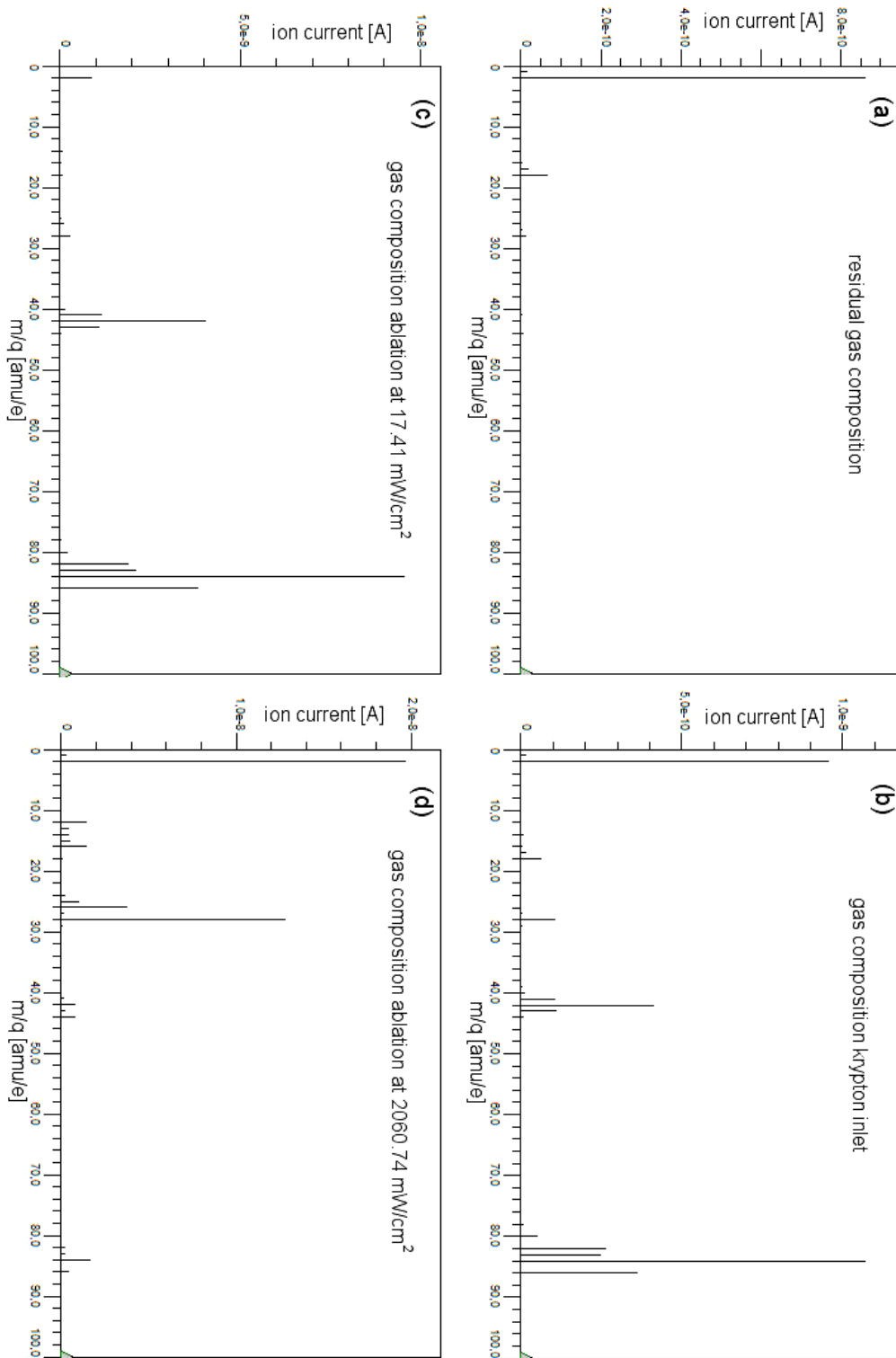


Figure 6.32.: **Mass spectra** of the residual gas composition inside the vacuum chamber (a), the gas composition during the Kr gas inlet (b) and during the low and high-intensity ablation (c) and (d).

This results in a much higher concentration of krypton gas in the area around the ion source of the RGA.

The 28 amu/e peak being comparatively smaller than during gas inlet suggests either a reduction in triple ionization of krypton or a reduction in the N₂ concentration. It is also possible that this peak appears smaller due to signal fluctuations which can be significant at the relatively short measurement time of 32 ms at every m/q bin.

- **(d):** During the high-intensity ablation the amount of H₂ increases by about an order of magnitude. This is accompanied by the presence of significant quantities of hydrocarbon fragments. Table 6.3 shows the possible sources for the peaks in this spectrum. The relatively high concentration of molecules that include one or

mass [amu]	ion	sources
1	H	hydrogen, water, acids, HY
2	H ₂	hydrogen
12	C	carbon monoxide or dioxide, HY
13	CH	HY
14	CH ₂ N	HY nitrogen
15	CH ₃	HY
16	CH ₄ O	HY oxygen, carbon monoxide or dioxide, water
24	C ₂	HY
25	C ₂ H	HY
26	C ₂ H ₂	HY
27	C ₂ H ₃	HY
28	C ₂ H ₄ CO N ₂	HY carbon monoxide or dioxide nitrogen, air
41	C ₃ H ₅ ⁸² Kr	HY DI krypton
42	C ₃ H ₆ ⁸⁴ Kr	HY DI krypton
43	C ₃ H ₇ ⁸⁶ Kr	HY DI krypton
44	C ₃ H ₈ CO ₂	HY carbon dioxide
82	⁸² Kr	krypton
83	⁸³ Kr	krypton
84	⁸⁴ Kr	krypton
86	⁸⁶ Kr	krypton

Table 6.3.: **Possible contents of the vacuum chamber during high-intensity ablation.** HY = hydrocarbon fragment, DI = doubly ionized [Inf03].

more carbon atoms could arise from the HOPG being ablated at high power. The increase in H₂ may be caused by heating of parts of the interior through the scattered

laser light. This might lead to hydrogen being desorbed from those parts and being available for reactions. Another possibility the release of stored hydrogen from the HOPG. Molecular hydrogen in ground state is nearly spherical with a kinetic diameter of 2.89 Å which makes it too wide to penetrate the hexagonal structure of the HOPG with a lattice constant of 2.46 Å [Waq07]. However, the presence of defects in the surface structure could allow the accumulation of H₂ through van der Waals forces. Experiments with atomic hydrogen, which is also present in small amounts, have shown that since it has a Bohr radius of only 0.5 Å it is capable of entering the bulk of HOPG and recombine to H₂ to be stored below the surface. Chemisorption of atomic hydrogen on HOPG is also possible. Desorption of atomic hydrogen from HOPG through heating partly leads to the creation of molecular hydrogen [Nik08]. However, the degree of hydrogenation of the HOPG is unknown and therefore the contribution by this factor is not quantifiable, as are the other effects for that matter.

After multiple ablation procedures at increasing intensities, the presence of krypton may stem from the desorption through heating of parts of the interior by scattered laser light. The krypton films had been prepared and ablated for weeks. During ablation the krypton would be desorbed from the HOPG and be distributed across the vacuum chamber, allowing adsorption at the cold shield and the substrate holder.

6.4.3. The adsorption of gasses at the HOPG surface

The carbon atoms in HOPG are very strictly sp²-hybridized (σ bonds to three neighbouring carbon atoms) which results in the planar hexagonal structure. The remaining p-orbital assumes a delocalized π -bond. In this configuration, carbon is chemically nearly inert and non-polar. Noble gases such as krypton, xenon or argon are physisorbed to HOPG as are N₂ and O₂ [Fau90], [Ulb02]. Physisorption is fundamentally caused by van der Waals forces which originate from interaction between induced, permanent or transient electric dipoles. Due to the fluctuating character of the electrons in atoms and molecules, they represent transient dipoles. The van der Waals force is the sum of the attractive and repulsive forces between these dipoles. Even the non-polar HOPG exhibits this behavior. The desorption

name	desorption energy [kJ/mol]	converted to meV/atom
water	46 ± 3	477 ± 31
oxygen	12 ± 1	124 ± 10
nitrogen	13 ± 1	135 ± 10
xenon	24 ± 2	249 ± 21
carbon dioxide	24 ± 2	249 ± 21
carbon monoxide	13 ± 1	135 ± 10
HOPG (interlayer)	4.2 ± 0.3	44 ± 3 [Liu11]

Table 6.4.: **Binding energies** of some gasses inside the vacuum chamber on HOPG [Ulb06].

energy of i.e. oxygen (O₂) to HOPG is 10-12 kJ/mol (depending on the O₂ coverage on the HOPG surface) which is 104-124 meV per molecule [Ulb02]. The binding energy has been determined through thermal desorption. Table 6.4 is a small excerpt from a compilation of the desorption energies of a number of gases on HOPG [Ulb06]. The value for krypton

could not be found but since it is also a noble gas, the energy necessary for desorption from HOPG should be near that of xenon.

7. Summary and outlook

In this work, several aspects concerning the condensed ^{83m}Kr source (CKrS) were discussed. A new setup design was introduced which facilitates the installation at the cryogenic pumping section (CPS) of the KATRIN experiment. Significant changes have to be made to the geometry of the substrate region and a system of movable frames and scaffolds will be implemented to which all other components of the CKrS will be mounted. To achieve the kind of mobility necessary to scan the entire flux tube of KATRIN, a set of lifting gears and computer controlled motors will be employed at the CKrS. The flux tube is scanned by moving the HOPG substrate with the ^{83m}Kr film and thus by directing the conversion electrons consecutively towards each pixel of the detector. A LabVIEW program has been written and all functions necessary for that task have been implemented and tested.

However, in order to ensure a truly automated scanning procedure, the program will need to be extended. Up to now all basic functions are available, but it is necessary to move to each desired position by manual input at the computer. A sequence of movements and idle times for measurements, would allow the targetting of all or a part of the detector pixels successively. This is easily achieved by implementing a routine that causes the positioning function to process a list of position values. This way with the push of a single button, a complete measurement cycle can be initiated.

The ablation setup has a number of shortcomings as several tests and observations have revealed. The beam profile has shown a deficit in power in the center of the beam which indicates that instead of the laser ground mode, mainly the TEM_{10} mode is excited. This could mean that the resonator mirrors are misaligned. Alternatively the second harmonics generation (SHG) module may be damaged and part of the beam could be lost therein. Furthermore, the laser operates at reduced power which can be attributed to various causes, but mostly to the Glan-Laser polarizer (GLP) which is discolored and absorbs a significant part of the laser power. The missing laser power in the beam center is another factor.

While the laser setup performed sufficiently well during the tests, these issues should be addressed before the implementation of the CKrS at the KATRIN experiment. To ensure reproducible results when using the ablation laser, the functionality regarding the power output needs to be restored. Several tests and adjustments can be performed on site, such as removing the SHG module to check the raw laser output or adjusting the phase matching of the SHG module. However, the manufacturer recommends that the adjustment of the laser resonator mirrors should be done by a specialist. Also the GLP needs to be replaced. In order to prevent damaging a new GLP, the laser output power should be reduced by adjusting the FLQ delay accordingly. Since the laser has far more power than necessary for the ablation of krypton and residual gas, this is easily possible.

One very important issue that needs to be addressed before its operation at the KATRIN experiment begins, is the achieving of laser class 1 for the ablation laser. For this purpose, a box will have to be constructed that encases the optical path between the laser output port and the vacuum window including every optical component in between to prevent direct or indirect irradiation of areas where personnel may be present.

Results from ablation procedures have been presented. Ellipsometric measurements on the HOPG substrate showed that its surface was modified at sufficiently high intensities. The irradiation of a single spot resulted in extensive damage to the substrate surface. The peeling and melting of the surface layers was visible in microscopic observation. The damage to the area of interaction was attributed to the high-intensity irradiation while additionally the surrounding area exhibited thermal damage due to the long laser pulse duration.

The residual gas analysis showed that molecular hydrogen accounts for the greatest percentage of the residual gas content in the vacuum chamber. The presence of water was also notable. During the inlet of krypton gas a slightly elevated presence of nitrogen was detected. This was attributed to the krypton gas being contaminated due to long storage in the mixing chamber at a relatively low pressure. During the low-intensity ablation the expected peaks of singly or multiply ionized krypton isotopes could be observed. During the high-intensity ablation the amount of hydrogen in the vacuum chamber rises significantly which may be an indication for the release of hydrogen stored at or below the surface of the HOPG. At this intensity the formation of a diversity of hydrocarbon fragments occurs. A getter pump will be available at the CPS to reduce the hydrogen content of the vacuum system.

A. Technical details on the motion control

A.1. Details on the IMD 20 drive module

Figure A.1 shows a more detailed view of the connectors on the IMD 20 drive module. Motors which are controlled via the IMD 20 operate at 40–95 V and the EC 60S motors in particular require a current of 6.9 A at the rated speed of 3000 rpm (the peak current is 20 A). Connector X1 provides the power for the motor from pins (W), (V) and (U). The input from a 50 V power supply also happens at X1. The two LEDs between X1 and X2

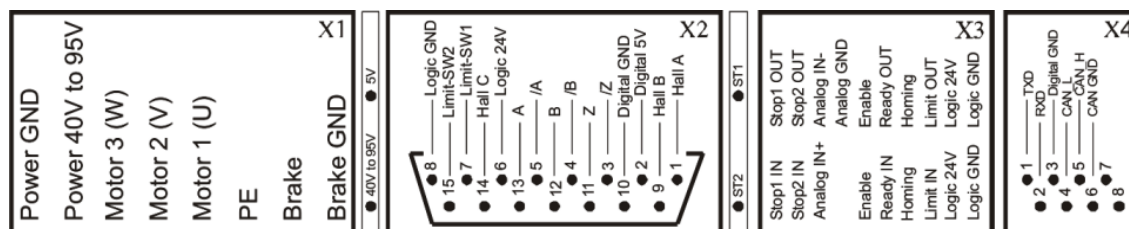


Figure A.1.: The IMD 20 connectors X1 to X4 are in use during operation [Ise08].

indicate whether sufficient voltage is applied to the motor (40–95 V) and to the encoder (5 V).

Via X2, the drive module receives the signals from the encoder and the hall sensors of the motor. Also, the status of the limit switches is monitored here. The LEDs next to X2 indicate the drive status. If both are illuminated the module is operational. However, in case of a fault in the system, one or both LEDs may flash a certain number of times. This code indicates the nature of the problem¹.

The X3 connector supplies the drive with the 24 V for the logic functions which in this case are the limit switches.

X4 is used for communication with the PXI system. Here the commands are received and the data from the encoder as well as drive status information are transmitted. These can then be processed by the PXI system and visualized at the LabVIEW PC.

At the side of the IMD 20 drive module is a DIP² switch which sets the communication parameters for the module. The DIP switch is queried only once, when the module is activated or after a reset. Switches 1 to 4 define the node ID at which the drive can be

¹Details on the fault code can be found in [Ise08].

²DIP: dual in-line package

accessed by the computer. A node ID of 0 activates the analogue input and communication with the drive is only possible via serial (RS-232) interface. The baud rate³ can be set by switch 5. The baud rate has to be the same at the transmitting and the receiving end. In low speed mode (switch 5 = 1), the signal rate is 20 kBd. When switched to high speed mode (switch 5 = 0) a baud rate of up to 1 MBd can be chosen. Switch 6 sets the type of interface (RS-232 or CAN bus) for the signal transfer. With switch 7 activated the “limit switch chain In” and “limit switch chain Out” are connected. If one or both limit switches are activated, the contact is open and power to the motor is cut. Switch 8 terminates the CAN bus with a resistor of 120 Ω if activated.

Since this setup uses the CAN bus at highest baud rate for communication and only one motor and drive per direction of movement, switches 5 to 8 are always in position 0 (on) and the node ID has to be at least 1 or greater.

The CAN network has to be terminated by a 120 Ω resistor at each end. The drive module contains such a resistor which can be activated by the DIP switch CAN terminator. At the PXI system the termination happens inside the DE-9 plug of the connecting cable (figure A.3). The resistor has to connect the CAN High and the CAN Low lead [Ise08].

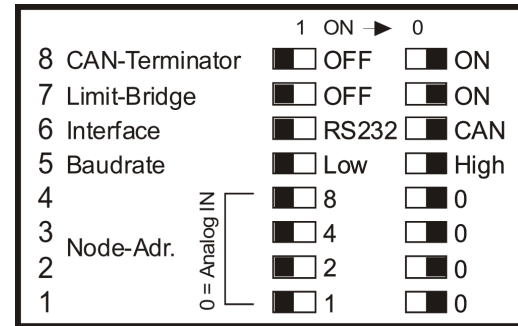


Figure A.2.: Schematic of the DIP switch at the side of the IMD 20 drive module [Ise08].

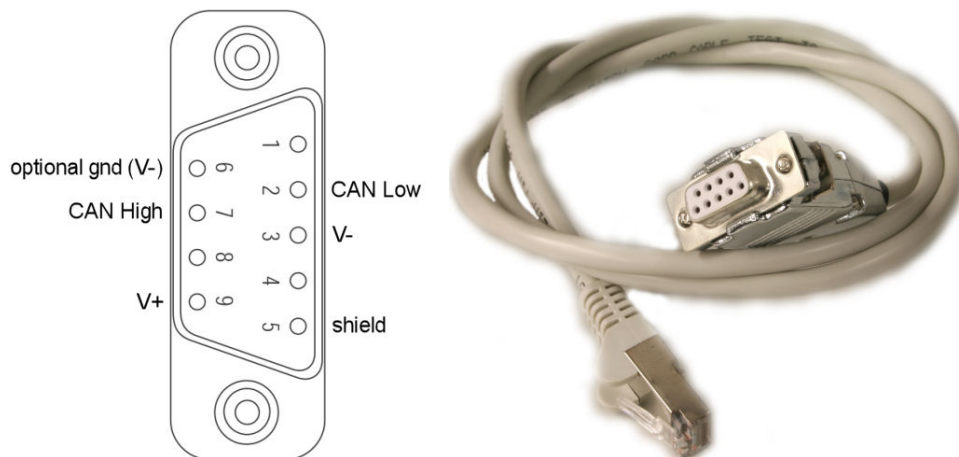


Figure A.3.: The cable connecting the CAN controller and the IMD 20 and its lead assignment at the DE-9 jack.

³Baud rate (Bd) is the unit of symbol or pulse rate. A baud of 1 kBd is synonymous to a symbol rate of 1000 symbols per second. In digital systems 1 Bd = 1 bit.

A.2. CANopen

The *Motorcontrol_v2.vi* is programmed using the CANopen DS402 device profile for drives and motion control [Ise08]. Write or read commands called “objects” are entered as a four digit hexadecimal number called “index”. Many objects offer several functions which are accessed by the “sub-index”, a two digit hexadecimal number. Write commands require a value (such as position or velocity) which is put in as a decimal number. This value is then converted to a signed or unsigned 8-, 16-, or 32-bit integer depending on the range of the possible values. With a read command such an integer is produced and needs to be translated to a decimal number for comprehensible output.

Figure A.4 shows a simple example for a position read command. First a “CANopen

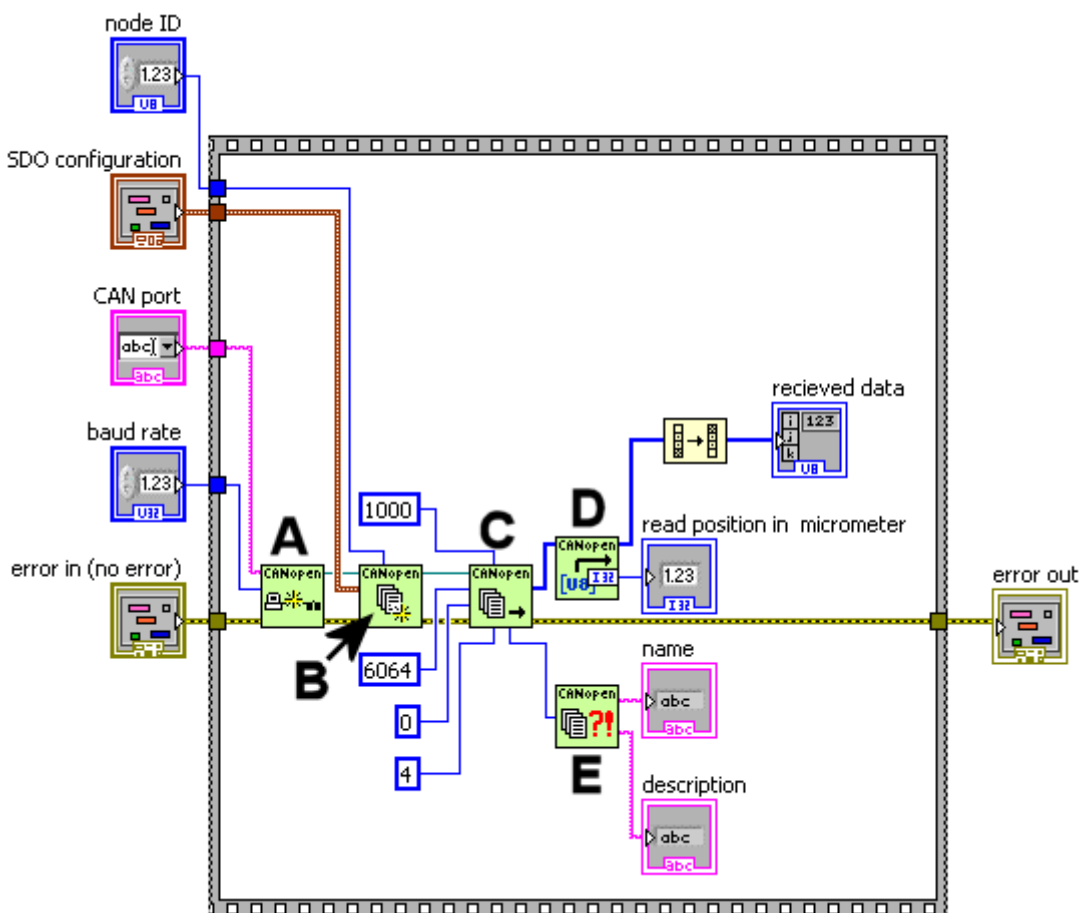


Figure A.4.: The `read_position` SubVI structure is representative for all implemented functions using the CANopen protocol.

interface” (A) is created for the CAN port (port 1 or 2 on the PXI-CAN module) and the baud rate for the data transfer is defined. The following “service data object” (SDO) (B) enables access to the object dictionary (a list of all possible write and read commands) for the drive. The drive is addressed by its node ID which is defined by the DIL switch. Now the “SDO read object” (C) reads the value of the desired parameter from the object

library. The object has an index of 6064 and a sub-index of 00 (only one 0 is displayed) and is a signed 32-bit integer. The data size of 4 byte and the timeout of 1000 ms are set by default. Since CANopen uses the little-endian format (least significant byte first) for the output and LabVIEW uses the big-endian format (most significant byte first), the data has to be converted by the “fetch from data [I32]” SubVI (**D**) before output. Optionally the completion code from the SDO can be displayed with name and description by the “SDO completion code to string” SubVI (**E**).

For a write command merely the “SDO read object” has to be replaced by the “SDO write object” SubVI. Some commands are read only and some are write only while others can be read or written. A complete set of objects used for the IMD 20 can be found in [Ise08]. These and other LabVIEW SubVIs for the programming of a CANopen based network using an IMD20 are accessed from the driver library which can be obtained via National Instruments (NI).

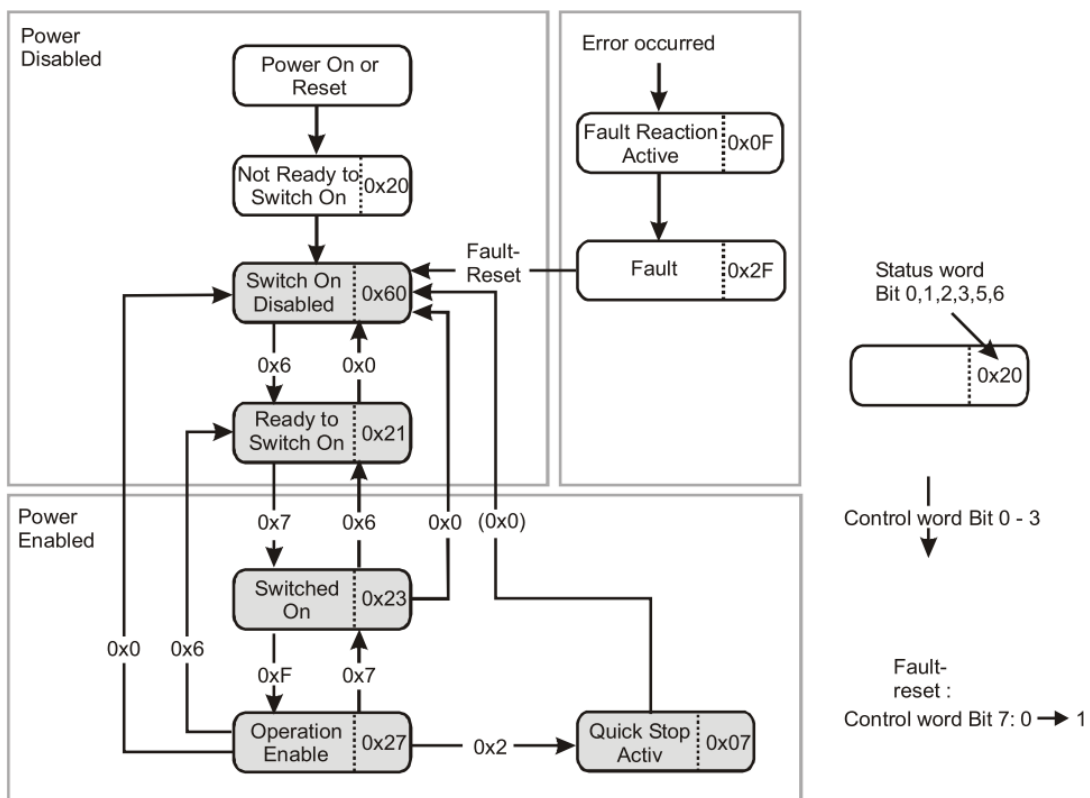


Figure A.5: **Schematic of the state machine** [Ise08]. The state of the drive can be queried by the status word. The values next to the state denomination show the output value (for example 23 for “Switched On”) for such a query.

An important characteristic of the IMD20 drive is that some commands have to be given in a certain order to make it operational. For this reason the drive module comprises a state machine that monitors the state the drive is in and determines which states can be accessed next. The diagram in figure A.5 shows a description of this state machine.

When power is turned on, first the drive is initialized (Not Ready to Switch On). After initialization, the drive remains in a state where all drive functions and the final stage are blocked. This is the post-initialization state (Switch On Disabled). Now the User has to input the appropriate commands to make the drive module operational. The state of the drive is changed by the control word, a 16 bit object (bits are counted 0, 1, 2, ...), which controls the most basic functions of the drive. Unlike any other object in the library it is used in every mode of operation the drive module has to offer. The control word index is 6040 with a sub index of 00. This sequence makes the drive operational up to the point where only the “start motion” command has to be given.

1. Index: 6040, sub index: 00, value: 6 (U 16)⁴ (011 in binary code). This command actually does not change the state of the drive or the final stage but merely sets the state from post-initialization to active user control (Ready to Switch On).
2. Index: 6040, sub index: 00, value: 7 (U 16) (111 in binary code). Now the final stage is released, but the drive functions are still blocked (Switched On)
3. Index: 6040, sub index: 00, value: F (U 16) (1111 in binary code). This enables all drive functions and the motor can be accessed by a single command.

Before starting the motion the user may now want to set the mode of operation, for example “profile position mode” and the motion parameters. Also the conversion factor between encoder increments and μm has to be defined.

4. The mode of operation is set by index: 6060, sub index: 00, value: 1 (I 8).
5. conversion factor numerator: index: 6093, sub index: 01, value: 16 (U 32).
6. conversion factor divisor: index: 6093, sub index: 02, value: 1 (U 32).
7. Target position: index: 607A, sub index: 00, value (I 32).
8. Final velocity: index: 6082, sub index: 00, value (U 32).
9. Acceleration: index: 6083, sub index: 00, value (U 32).

The mode of operation and the conversion factor can be set before, during or after steps 1 to 3, because these objects are not subject to the processes in the state machine. However, the movement parameters have to be put in after the “profile position mode” is activated and before the motion is started. The command to start movement in any mode of operation except the velocity control mode⁵ is given by setting bit no. 4 of the control word to 1 while all the previously set bits (0 to 3) have to remain as they were. The command for starting motion is therefore:

10. Index: 6040, sub index: 00, value: 31 (U 16) (11111 in binary code)

⁴The U 16 declares that the value has to be converted to a unsigned 16-bit integer. There are 8-, 16-, and 32-bit formats which can be signed (prefix I) or unsigned (prefix U).

⁵The command to start motion in velocity control mode is simply given by sending the command to change the velocity.

If the state of the drive is unknown, the status word (index: 6041, sub index: 00 (U 16)) can be queried. Figure A.5 shows the values of the status word for each state. This object constitutes a comparison tool for if-then functions in the program. If, for example, the homing mode is activated and the zero position is acquired, the status word has a different value than after the reference run is completed. Also, faults can be identified by use of this object and reset by setting bit 7 of the control word to 1.

B. Tables

B.1. Measurement data on laser parameters

FLQ-delay [μ s]	laser power [arb. units]
195	2.00
200	1.99
210	1.89
220	1.78
230	1.60
240	1.49
250	1.31
260	1.16
270	1.09
280	1.00
290	0.91
300	0.82
310	0.71
320	0.62
330	0.50
340	0.43
350	0.38
360	0.35
370	0.33
380	0.33
390	0.31
400	0.31
500	0.29 (background value)

Table B.1.: **Table on power adjustment through variation of the FLQ-delay.** Flash lamp voltage: 1380 V, GLP angle: 307°.

flash lamp voltage [V]	laser power [arb. units]
1380	2.07
1360	2.02
1340	2.03
1320	2.02
1300	2.04
1280	1.99
1260	1.88
1240	1.88
1220	1.81
1200	1.78
1180	1.76

Table B.2.: **Table on power adjustment through variation of the flash lamp voltage.**
FLQ-delay: 195 μ s, GLP angle 307°.

B.2. Measurement data on the beam profile

y in mm	0	1	2	3	4	5	6	7	8	9	10	x in mm				
10	0,76	0,77	0,76	0,77	0,79	0,79	0,81	0,81	0,82	0,82	0,83	0,83				
9	0,83	0,85	0,85	0,86	0,93	0,86	0,92	0,85	0,84	0,83	0,83	0,83				
8	0,83	0,84	1,01	1,85	3,58	6,15	4,2	3,25	3,23	1,74	1,16	0,94	0,9	0,87	0,86	0,85
7	0,85	0,93	1,1	2,95	8,14	11,69	6,95	2,6	2,73	4,19	7,98	3,42	1,67	0,96	0,87	0,85
6	0,83	0,91	1,44	5,85	6,28	3,39	1,89	1,29	1,57	3,73	10,3	4,97	2,62	1,29	0,93	0,88
5	0,87	0,98	1	2,99	5,62	2,54	1,66	1,22	1,36	2,26	6,74	5,2	2,47	1,14	0,91	0,88
4	0,86	0,85	0,86	1,23	3,19	2,84	2,22	1,7	1,76	2,05	3,86	3,85	1,57	0,97	0,87	0,88
3	0,88	0,88	0,88	0,92	1,07	1,5	1,69	1,64	1,45	1,26	1,02	0,93	0,88	0,88	0,88	0,88
2	0,86	0,84	0,85	0,88	0,87	0,87	0,87	0,87	0,87	0,85	0,85	0,85	0,85	0,85	0,85	0,85
1	0,86	0,87	0,86	0,89	0,89	0,89	0,89	0,87	0,87	0,86	0,86	0,86	0,86	0,86	0,86	0,86
0	0,85	0,84	0,84	0,85	0,85	0,85	0,85	0,85	0,85	0,86	0,86	0,85	0,85	0,86	0,87	0,85

Table B.3.: Raw data from the beam profile measurement (arbitrary units).

y in mm	0	1	2	3	4	5	6	7	8	9	10	x in mm					
10	0,000	0,001	0,000	0,000	0,001	0,002	0,003	0,003	0,003	0,004	0,005	0,005	0,005	0,005	0,005	0,006	0,006
9	0,003	0,004	0,005	0,004	0,005	0,005	0,006	0,009	0,005	0,006	0,006	0,006	0,005	0,006	0,006	0,006	0,006
8	0,006	0,007	0,008	0,008	0,009	0,009	0,016	0,009	0,015	0,008	0,008	0,007	0,007	0,006	0,007	0,006	0,006
7	0,006	0,007	0,008	0,012	0,016	0,024	0,047	0,061	0,089	0,072	0,033	0,021	0,016	0,015	0,010	0,009	0,008
6	0,006	0,007	0,015	0,023	0,100	0,258	0,493	0,315	0,228	0,226	0,090	0,037	0,016	0,013	0,011	0,010	0,009
5	0,007	0,009	0,011	0,023	0,081	0,279	0,841	0,817	0,305	0,214	0,288	0,340	0,121	0,034	0,016	0,010	0,009
4	0,008	0,012	0,016	0,031	0,200	0,675	1,000	0,566	0,168	0,180	0,314	0,661	0,243	0,083	0,018	0,014	0,009
3	0,007	0,011	0,015	0,054	0,386	0,960	0,615	0,241	0,135	0,136	0,398	0,891	0,382	0,131	0,032	0,014	0,011
2	0,006	0,010	0,014	0,062	0,466	0,505	0,241	0,103	0,048	0,074	0,272	0,873	0,385	0,170	0,048	0,016	0,012
1	0,008	0,013	0,017	0,039	0,378	0,395	0,114	0,082	0,084	0,060	0,239	0,855	0,399	0,197	0,052	0,019	0,012
0	0,010	0,015	0,020	0,022	0,204	0,445	0,163	0,082	0,042	0,055	0,137	0,547	0,406	0,156	0,035	0,014	0,012
	0,010	0,012	0,014	0,016	0,043	0,222	0,190	0,134	0,086	0,091	0,118	0,284	0,283	0,074	0,019	0,012	0,011
	0,009	0,009	0,008	0,009	0,009	0,061	0,127	0,159	0,145	0,124	0,124	0,160	0,082	0,027	0,012	0,011	0,011
	0,010	0,010	0,010	0,010	0,016	0,028	0,068	0,085	0,081	0,063	0,046	0,024	0,016	0,011	0,011	0,011	0,011
	0,011	0,011	0,011	0,011	0,011	0,013	0,015	0,018	0,016	0,020	0,016	0,016	0,012	0,011	0,011	0,011	0,011
	0,010	0,010	0,009	0,009	0,010	0,011	0,013	0,014	0,013	0,015	0,013	0,013	0,011	0,010	0,010	0,010	0,010
	0,009	0,008	0,007	0,008	0,008	0,010	0,011	0,011	0,010	0,010	0,010	0,010	0,010	0,010	0,009	0,008	0,009
	0,009	0,009	0,009	0,009	0,009	0,010	0,011	0,011	0,011	0,011	0,011	0,010	0,010	0,009	0,009	0,010	0,009
	0,009	0,010	0,010	0,010	0,009	0,011	0,012	0,012	0,011	0,010	0,010	0,010	0,010	0,009	0,009	0,010	0,010
	0,009	0,009	0,008	0,008	0,009	0,010	0,010	0,010	0,010	0,010	0,009	0,009	0,010	0,009	0,009	0,010	0,009
	0,008	0,008	0,007	0,007	0,007	0,008	0,008	0,008	0,008	0,008	0,008	0,009	0,009	0,008	0,009	0,010	0,009

Table B.4.: Normalized data without background.

B.3. Power adjustment via the GLP

GLP angle [°]	laser power [mW/cm ²]	GLP angle [°]	laser power [mW/cm ²]
223	1930.59	269	925.41
225	1927.77	271	858.27
227	1920.27	273	791.65
229	1908.11	275	725.87
231	1891.36	277	661.27
233	1870.11	279	598.15
235	1844.45	281	536.83
237	1814.50	283	477.59
239	1780.42	285	420.73
241	1742.38	287	366.52
243	1700.55	289	315.24
245	1655.14	291	267.13
247	1606.37	293	222.42
249	1554.48	295	181.33
251	1499.73	297	144.06
253	1442.37	299	110.80
255	1382.69	301	81.70
257	1320.98	303	56.91
259	1257.54	305	36.55
261	1192.68	307	20.71
263	1126.71	309	9.48
265	1059.96	311	2.91
267	992.75	313	1.03

Table B.5.: **Table on the power adjustment through GLP orientation.** The GLP angle is the absolute value taken from the scale of the GLP mount. These values are calculated from the fit parameters obtained from the measurements through the damaged central part of the GLP.

B.4. Measurement data on HOPG damage

GLP angle [°]	P_{laser} [mW/cm ²]	u_P [mW/cm ²]	polarizer angle [°]	u_{pol} [°]
313	0.04	0.14	75.41	0.34
308	17.41	2.94	68.87	0.19
303	65.76	5.67	66.41	0.22
298	143.63	8.25	65.76	0.20
293	248.62	10.62	65.34	0.20
288	377.53	12.73	65.10	0.20
283	526.42	14.52	64.59	0.21
278	690.73	15.98	64.00	0.19
273	865.42	17.06	63.26	0.19
268	1045.17	17.78	61.66	0.19
263	1224.47	18.13	61.31	0.19
258	1397.83	18.15	61.93	0.18
253	1559.96	17.88	62.37	0.19
248	1705.89	17.40	63.18	0.21
243	1831.15	16.78	64.86	0.20
238	1931.92	16.13	65.01	0.20
233	2005.12	15.57	65.40	0.20
228	2048.50	15.20	65.56	0.20
223	2060.74	15.08	66.41	0.21

Table B.6.: **The data on figure 6.25.** The error values for the laser power are calculated from the fit data in [Mur11] and an assumed 0.3° error for the GLP angle. The error on the polarizer angle is calculated by the ellipsometry program.

Bibliography

- [Abe11] K. Abe et al. (Superkamiokande Collaboration) “Search for Differences in Oscillation Parameters for Atmospheric Neutrinos and Antineutrinos at Super-Kamiokande”, Phys. Rev. Lett. 107 (2011) 241801, 2011
- [Aha05] B. Aharmim et al. (SNO Collaboration), Electron Energy Spectra, Fluxes, and Day-Night Asymmetries of ^8B Solar Neutrinos from the 391-Day Salt Phase SNO Data, 2005
- [Ahm01] Q. R. Ahmad et al. (SNO Collaboration), Phys. Rev. Lett. 87, 071301 (2001)
- [Alt03] G. Altarelli, K. Winter (Hrsg.), Neutrino Mass, Springer-Verlag, 2003
- [Ang04] J. Angrik et al., KATRIN Design Report 2004, FZK Scientific Report 7090, <http://www-ik.fzk.de/katrin/>
- [Ari98] E. Arimondo et al., Laser vaporization of carbon in the presence of carbon dioxide, Appl. Phys. A 66, 407-411 (1998), 1998
- [Ash04] Y. Ashie et al. (Super-Kamiokande Collaboration), hep-ex/0404034
- [Azz87] R. M. A. Azzam, N.M. Bashara, Ellipsometry and Polarized Light, North Holland 1977
- [Bah95] “Solar models with helium and heavy-element diffusion.”, J.N. Bahcall, M.H. Pinsonneault, Reviews of Modern Physics, Vol. 67, No. 4, 1995
- [BAL] BALZERS AG, brochure on “Partialdruckmessung in der Vakuumtechnik”, BG 800 169 PD (8711)
- [Bau12] S. Bauer et al., Ellipsometry with polarisation analysis at cryogenic temperatures inside a vacuum chamber, paper in preparation, expected 2012
- [Bau13] S. Bauer, dissertation in preparation, expected 2013
- [Bea80] J. Beamson, et. al., J.Phys. E13 (1980) 64, 1980
- [Bla07] K. Blaum, University of Mainz, lecture: “Massenspektrometrie und Teilchenfallen WS 07/08”, 2007
- [Cha14] J. Chadwick, Verh. d. Deutsch. Phys. Ges. 16 (1914) 383
- [Cha32] J. Chadwick, Nature 129 (1932) 312
- [CRC83] CRC Handbook of Chemistry and Physics, 64th Edition, 1983
- [Dav96] “A Review of Measurements of the Solar Neutrino Flux and their Variation.”, R. Davis Jr., Nuclear Physics B (Proc. Suppl.) 48, 284-298 (1996)

- [Dem06] W. Demtröder, Experimentalphysik 2, ISBN 3-540-21473-9, 2006
- [Den10] Prof. Dr. C. Denz, lecture on applied physics, WWU Münster, 2010
- [Fau90] J.W.O. Faul et al., Ellipsometric thickness and coverage of physisorbed layers of Xe, Kr, Ar and N₂ on graphite, Surface Science 227:390-394, 1990
- [Fer34] E. Fermi, Z. Phys. 88 (1934) 161 - 177
- [Fra11] F.M. Fränkle et. al., Radon induced background processes in the KATRIN pre-spectrometer, <http://dx.doi.org/10.1016/j.astropartphys.2011.06.009>
- [Fuk02] S. Fukuda et al., Phys. Lett. B539, 179 (2002)
- [Gil10] W. Gil et al., "The Cryogenic Pumping Section of the KATRIN Experiment" Applied Superconductivity, IEEE Transactions on , vol.20, no.3, pp.316-319, 2010
- [Gil11] W. Gil, Calculations on the magnetic fields for the cryogenic pumping section of the KATRIN experiment (not released), 2011
- [Gre12] B. Grees, diploma thesis, University of Münster, in preparation
- [Gro09] Grohmann S et al. Cryogenics 49, Issue 8 (2009)
- [Hug08] K. Hugenberg, Diplomarbeit, Institut für Kernphysik, Westfälische Wilhelms-Universität Münster, 2008
- [Inf03] Inficon, Technical Note: General RGA Spectrum Interpretation Guide, http://www.inficon.com/download/en/Spectrum_Guide.pdf, 2003
- [Ise08] http://www.isel-data.de/manuals/DATEN/EN/ELECTRONICS/Poweramplifiers/IMD20/IMD20_IMD40_OperatingInstruction.pdf, IMD 20 manual, 2008
- [Ise10] http://www.isel-data.de/manuals/DATEN/EN/ELECTRONICS/Motors/EC-servomotors/970476_DM001-Datenblatt_EC_60_Servomotoren.pdf, datasheet, 2010
- [Kau02] W. Kaufmann, Phys. Zeitschr. 4 (1902) 54
- [Kaz08] Kazachenko O et al, NIM A 587 (2008)
- [Kla01] H. V. Klapdor-Kleingrothaus et al., Eur. Phys. J. A 12 (2001) 147 - 154
- [Kla04] H. V. Klapdor-Kleingrothaus et al., Phys. Lett. B586 (2004) 198 - 212
- [Kra05] Ch. Kraus, B. Bornschein, L. Bornschein, J. Bonn, B. Flatt, A. Kovalik, B. Ostrick, E.W. Otten, J.P. Schall, Th. Thümmel, Ch. Weinheimer, Eur. Phys. J. C 40 (2005) 447
- [Kod01] K. Kodama et al. (DONUT Collaboration), Phys. Lett. B504 (2001) 218 - 224
- [Kue12] M. Kues and S. Dobner, Institute for Applied Physics, WWU Münster, Assessment on the beam profile, private communication, 2012
- [Lar10] Larson, D., Dunkley, J., Hinshaw, G., et al. 2010, arXiv:1001.4635v2
- [Leb10] M. Leber phd thesis, Univ. of Washington, Seattle (2010)

- [Liu11] Z. Liu et al. Interlayer binding energy of graphite - A direct experimental determination, <http://arxiv.org/pdf/1104.1469v1.pdf>, 2011
- [Lob85] V.M. Lobashev, P. E. Spivak, Nucl. Instr. and Meth. A 240 (1985) 305
- [Lob11] V. M. Lobashev et al., Phys. Rev. D 84, 112003 (2011)
- [Mas07] S. S. Masood et al., hep-ph/0706.0897 v1 (2007)
- [Mec99] Á. Mechler et al., Excimer laser irradiation induced formation of diamond-like carbon layer on graphite, Applied Surface Science 138-139 (1999) 174-178, 1999
- [Mis06] MissMJ (Wikipedia author), http://en.wikipedia.org/wiki/File:Standard_Model_of_Elementary_Particles.svg, 2006
- [Mom96] C. Momma et al., Short-pulse laser ablation of solid targets, Optics Communications 129 (1996) 134-142, 1996
- [Mue93] F. Mueller et al., Comparative study of deposition of thin films by laser-induced PVD with femtosecond and nanosecond laser pulses, Proc. SPIE Vol. 1858, p. 464-475, 1993
- [Mur11] Michael Murra, bachelor thesis, "Set up of an ablation laser system for the Krypton conversion electron source of the KATRIN experiment" University of Münster, 2011
- [Nag06] Sz. Nagy et al., On the Q-value of the tritium β -decay, Europhys. Lett. 74 (2006) 404
- [Nak10] K. Nakamura et al. (Particle Data Group), JP G 37 , 075021 (2010)
- [NI1] http://www.ni.com/pdf/products/us/4daqsc386-393_386-387.pdf, PXI-6602 data sheet
- [Nik08] A. Nikitin, C-H bond formation at the graphite surface studied with core level spectroscopy, Surface Science 602 (2008) 2575-2580, 2008
- [Nol02] W. Nolting: Grundkurs Theoretische Physik 3, 6. Auflage, Springer-Verlag, 2002
- [Noz07] <http://www.nozag.ch/nozag/catalogue/zserie//PDF/page13.pdf>, data sheet, 2007
- [Nudat2] <http://www.nndc.bnl.gov/nudat2/>, Datenbank National Nuclear Data Center und Brookhaven National Laboratory
- [Ort11] H.-W. Ortjohann, private communication, 2011
- [Ost08] B. Ostrick, Dissertation, Inst. f. Kernphysik, Westfälische Wilhelms-Universität Münster, 2009
- [Ott08] Otten, E., & Weinheimer, C. 2008, Rept.Prog.Phys., 71, 086201
- [Pau30] Wolfgang Pauli, "Offener Brief an die Gruppe der Radioaktiven bei der Gauvereins-Tagung zu Tübingen" (dated December 4, 1930), reproduced in: R. Kronig and V. Weisskopf (Eds.), Wolfgang Pauli, Collected Scientific Papers, Vol.2, Interscience, New York (1964) 1316 - 1317
- [Per75] M. L. Perl et al., Phys. Rev. Lett. 35 (1975) 1489

- [PI] PI, M-060 Series Rotation Stages, www.physikinstrumente.com/en/pdf/M060_Datasheet.pdf
- [Pic92a] A. Picard, et. al. Nucl. Instr. Meth. 63 (1992) 345
- [Pic02b] A. Picard, et. al. Z. Phys. A342 (1992) 71-78
- [Pra11] M. Prall, Dissertation, Institut für Kernphysik, Westfälische Wilhelms-Universität Münster, 2011
- [Put12] R. de Putter et al., “New Neutrino Mass Bounds from Sloan Digital Sky Survey III Data Release 8 Photometric Luminous Galaxies,” arXiv:1201.1909 [astro-ph.CO].
- [Qua08] http://www.quantel.fr/industrial-scientific-lasers/media/produit/fichier/53_BrilliantVA0608.pdf, Quantel Brilliant laser, data sheet, 2008
- [Qua10] Quantel Brilliant / Brilliant B user manual v6.0, 2010
- [Rei59] F. Reines and C. L. Cowan, Phys. Rev. 113, 273-279 (1959)
- [Rei92] D. H. Reitze, Optical properties of liquid carbon measured by femtosecond spectroscopy, Phys. Rev. B 45, 2677-2693 (1992)
- [Ren08] [http://resources.renishaw.com/en/details/Installation+guide%3a+RGH41+series+readhead\(29113\)](http://resources.renishaw.com/en/details/Installation+guide%3a+RGH41+series+readhead(29113)) installation guide, 2008
- [Res11] O. Rest, Setup and test of an electron monitor detector for the KATRIN experiment, bachelor thesis, 2011
- [Rie11] Riess, A. G., Macri, L., Casertano, S., et al. 2011, ApJ, 730, 119
- [Rin05] A. Ringwald, hep-ph/0505024 v1 (2005)
- [Rob88] “Direct Measurements of Neutrino Mass”, R. G. H. Robertson, D. A. Knapp, Annual Review of Nuclear and Particle Science, Vol. 38: 185-215 (1988)
- [Ron58] A. R. Ronzio, C. L. Cowan, and F. Reines, Rev. Sci. Instrum. 29, 146 (1958)
- [Rut08] E. Rutherford and H. Geiger, Proc. Roy. Soc. A81 (1908) 162
- [Rut14] E. Rutherford and E. N. da C. Andrade, Phil. Mag. 27 (1914) 854
- [Sal08] B. E. A. Saleh, M. C. Teich, Grundlagen der Photonik, Wiley-VCH, 2008
- [Sch11] T. Schäfer, Diplomarbeit, Institut für Kernphysik, Westfälische Wilhelms-Universität Münster, 2011
- [Sch97] N. Schmitz, Neutrinophysik, Teubner Verlag, 1997
- [Shi00] M.D. Shirk, P.A. Molian, Ultra-short pulsed laser ablation of highly oriented pyrolytic graphite, Carbon 39 (2001) 1183-1193, 2000
- [Smo08] J. Smollich, Diplomarbeit, Institut für Kernphysik, Westfälische Wilhelms-Universität Münster, 2008
- [SNO02] “Direct Evidence for Neutrino Flavor Transformation from Neutral-Current Interactions in the Sudbury Neutrino Observatory”, SNO Collaboration, Phys. Rev. Lett. 89, No. 1, 011301 (2002)

- [Spi11] D. Spitzer, diploma thesis, Institut für Kernphysik, Westfälische Wilhelms-Universität Münster, 2011
- [SK04] M. Ishitsuka for the Super-Kamiokande Collaboration, Proceedings for the XX-XIXth Rencontres de Moriond on Electroweak Interactions (2004)
- [Stu07] M. Sturm, diploma thesis, Institut für Kernphysik, Uni Karlsruhe, 2007
- [Stu96] B. C. Stuart et al., Optical ablation by high-power short-pulse lasers, Vol. 13, No. 2/February 1996/J. Opt. Soc. Am. B, 1996
- [Sve10] O. Svelto, Principles of Lasers, ISBN 978-1-4419-1301-2, 2010
- [Tho12] Thorlabs catalogue V21 <http://www.thorlabs.us/catalogpages/V21/903.PDF>, 2012
- [Thu07] T. Thümmeler, Dissertation, Institut für Kernphysik, Westfälische Wilhelms-Universität Münster, 2007
- [Tog96] H. Togashi et al., Formation of large carbon cluster ions at graphite (HOPG) surfaces by laser irradiation, Applied Surface Science 96-98 (1996) 267-271, 1996
- [Tra07] Transpector2 Operating Manual, IPN 074-276R, 2007
- [Ul02] H. Ulbricht et al., Physisorption of molecular oxygen on single-wall carbon nanotube bundles and graphite, Phys. Rev. B 66, 075404, 2002
- [Ul06] H. Ulbricht et al., Thermal desorption of gases and solvents from graphite and carbon nanotube surfaces, Carbon 44, 2931-2942, 2006
- [Val09] K. Valerius, phd thesis, Univ. of Münster (2009)
- [Vol89] U.G. Volkmann, K. Knorr: Ellipsometric study of krypton physisorbed on graphite, Surface Science 221, 379-393, 1989
- [Waq07] Z. Waqar, Hydrogen accumulation in graphite and etching of graphite on hydrogen desorption, J Mater Sci (2007) 42:1169-1176, 2007
- [Weg10] A. Wegmann, diploma thesis, Institut für Kernphysik, Westfälische Wilhelms-Universität Münster, 2010
- [Win97] R. Windholz and P. A. Molian, Journal of Materials Science 32 (1997) 4295 - 4301, 1997

Danksagung

Ich bedanke mich herzlich bei der gesamten Arbeitsgruppe von Prof. Weinheimer für die wunderbare Zeit und die Hilfsbereitschaft während der Diplomarbeit. Insbesondere gilt mein Dank Prof. Weinheimer, der mir die Ausbildung in einem äußerst spannenden Tätigkeitsfeld ermöglicht hat und mich in allen Fragen und Anliegen auf sehr motivierende und inspirierende Art und Weise unterstützt hat.

Ich danke Prof. Khoukaz, der sich als Gutachter für diese Diplomarbeit zur Verfügung gestellt hat.

Ich bedanke mich bei Stephan, für die sehr gute Betreuung während der Diplomarbeit und bei Miroslav für die zahlreichen Stunden, die er für das Korrekturlesen erübrigt hat. Außerdem danke ich Benjamin, der mir bei diversen Programmierungen geholfen hat.

Ich möchte mich bei Hans-Werner Ortjohann, Georg Bourichter und der gesamten Feinmechanischen Werkstatt für die Fertigung der vielen Teile bedanken.

Ich danke Roland Berendes und der gesamten Elektronischen Werkstatt für die Fertigung und Reparatur der zahlreichen Kabel und Geräte.

Ich danke Benjamin, Daniel, Michael und Oliver, für die Zusammenarbeit in einer Atmosphäre, die von Hilfsbereitschaft und Freundschaft bestimmt war.

Ich bedanke mich bei Christopher, Marcel, Felix und Christopher für die unendlichen Stunden des Zettelrechnens und den ganzen Spaß außerhalb der Uni.

Ich danke ganz besonders meinen Eltern, die mir dieses Studium ermöglicht haben und mich über die gesamte Zeit sowohl finanziell als auch moralisch unterstützt haben.

Mein größter Dank gilt Vanessa, die ich sehr liebe, dafür dass sie immer an mich geglaubt hat und mich in schweren Tagen ermuntert und mir zur Seite gestanden hat.

